Electrical and Electronic Engineering Department
Faculty of Engineering

Modelling of Electromagnetic Material Properties at Microwave Frequencies

by

Majid Hamid Nassar Alsadi

B.Sc. (Electronic Eng), M.Sc. (Electronic Eng)

Thesis submitted to the University of Nottingham for
the degree of Doctor of Philosophy

March 2012

To the one who taught me the

binary system before I learn

multiplication tables …

my father Dr Hamid N. Al-Sadi

Contents

Abstract

In recent years, electromagnetic interference (EMI) has raised serious issues in terms of the unintentional radiation that disrupts the near proximity equipment from working properly. One solution to reduce the effects of EMI is the use of electromagnetic shielding. Carbon fibre composite (CFC) material is a promising customised product that has entered numerous industrial areas due to its attractive properties like high strength, low weight, and the resistance to chemical substances and corrosion. CFC has started to be used as electromagnetic shields, for example modern computer cases. However, not much is known about its electromagnetic behaviour.

This research derives various models for CFC materials for the purpose of achieving better understanding to their interaction with electromagnetic waves at microwave frequencies.

Throughout this research, the electrical properties of different materials have been investigated in terms of their shielding effectiveness (SE). The modelling was performed using the transmission-line modelling (TLM) method. The digital filter (DF) technique was used for small structures that are embedded in the system under modelling. In this way, the space mesh can be turned into coarser mesh. While maintaining the same accuracy, this technique has substantially saved on computational

resources and has increased the speed of the modelling process. This in turn, has made it more feasible to model large scale practical systems. The formulae of DF cascading were derived to allow modelling systems of multiple embedded structures. Simulated models were validated by comparing them with the corresponding conventional fine mesh results. One-dimensional models were validated with the available analytic solution. Experimental measurements were conducted on panels made of this anisotropic material, which has manifested frequency-dependent characteristics that satisfy Drude model. These measurements have validated the corresponding numerical electromagnetic models.

The final product of this study is gaining better knowledge about the electromagnetic behaviour of different materials. This knowledge can help in predicting the shielding performance when these materials are used within large-scale systems.

Acknowledgements

I would like to thank my principal supervisor Professor Christos Christopoulos for introducing me to the world of EMC by suggesting this subject. His valuable comments served to clarify the topic to me. My thanks go also to my second supervisor Dr John D. Paul for introducing me to the laboratory equipment and how to use them. Throughout 151 meetings, I experienced the kindness of my supervisors who were always supporting me in tackling the numerous difficulties that have faced the project.

I am grateful to Dr Angela Nothofer for the useful and interesting discussions regarding practical aspects and for providing me with some industrial standards of microwave measurements.

My deep gratitude goes to Professor Richard E. Challis and through him to Airbus Company for providing me with a sample of carbon fibre composite material that was used in the experimental sessions.

Special thanks go to my colleagues Dr Ke Jia, Miss Bohan Liu, and Dr Abdul Rehman for supporting me in performing parallel computing in running the simulation codes.

I am indebted to Dr Ana Vukovic for inviting me to join the researchers in George Green Institute for Electromagnetics Research (GGIEMR) to complete my PhD degree.

List of Symbols and Acronyms

I. Symbols

The following symbols are used throughout this thesis.

Symbol	Description	First use
[C]	Connection matrix	§4.6 p.56
[S]	Scattering matrix	§4.6 p.56
β	Phase constant per unit metre of the medium	§2.3 p.16
Γ	Reflection coefficient	§5.3 p.74
Γ_F	Fresnel reflection coefficient for the half-plane of a thin panel	§5.3.1 Eq. 5.8 p.77
$\Gamma_{F\perp}$	Fresnel reflection coefficient when electric field is perpendicular to the plane of incidence	§5.3.1 Eq. 5.11 p.77
$\Gamma_{F\parallel}$	Fresnel reflection coefficient when electric field is parallel to the plane of incidence	§5.3.1 Eq. 5.12 p.77
δ	Skin depth or depth of penetration	§2.5 p.19
Δl	Side length of SCN or space discretisation	§4.7 p.56
Δt	Time step or time discretisation	§4.7.1 Eq. 4.14 p.58
Δx	Length of transmission-line section in x-direction	§2.3 p.15
Δx	Side length of SCN in the x-direction	§4.7.1 Eq. 4.13 p.58
Δy	Side length of SCN in the y-direction	§4.7.1 Eq. 4.13 p.58
Δz	Side length of SCN in the z-direction	§4.7.1 Eq. 4.13 p.58
ε	Permittivity of the medium/material	§2.3 Eq. 2.4 p.16
ε_o	Permittivity of free space (ε_o = 8.854x10^{-12} F/m)	§5.3.1 Eq. 5.10 p.77
ε_r	Relative permittivity of medium/material	§5.3.1 p.76

θ	Angle of incidence measured from the normal to the panel surface	§5.3.1 p.76
θ_t	Angle of transmission measured from the normal to the panel surface	§5.3.1 Fig. 5.5 p.78
λ	Operating wavelength	§7.3 p.180
λ_{min}	Minimum useful wavelength	§4.9 p.62
μ	Permeability of the medium/material	§2.3 Eq. 2.4 p.16
μ_o	Relative permeability of free space ($\mu_o = 4\pi \times 10^{-7}$H/m)	§7.6 p.192
μ_r	Relative permeability of medium/material	§2.5 p.19
σ	Conductivity of the medium/material	§2.3 Eq. 2.4 p.16
$\sigma(\omega)$	Frequency-dependent conductivity	§7.7 Eq.7.5 p.194
σ_{cm}	Electrical conductivity of a composite	§3.6.2 p.39
σ_f	Conductivity of the fibre	§3.6.2 Eq. 3.2 p.39
σ_r	Conductivity of the resin (matrix)	§3.6.2 Eq. 3.2 p.39
Σ	Summation	§5.1.2 Fig. 5.1 p.69
τ_o	Relaxation time for electron scattering in Drude model	§7.7 Eq.7.5 p.194
ω	Radian frequency	§2.3 p.16
a	Inner dimension of a cavity in x-direction	§5.5.3.2 Eq. 5.32 p.100
a_i	Digital filter real coefficient that determines feedback link	§5.1.2 Eq. 5.3 p.68
a_{ri}	Reflection digital filter real coefficient that determines feedback link	§5.3.1 Eq. 5.6 p.76
a_{ti}	Transmission digital filter real coefficient that determines feedback link	§5.3.1 Eq. 5.7 p.76
A	Absorption loss in dB	§3.6.2 Eq. 3.1 p.39
A_F	Area of the face window	§6.4.2 p.141
A_i	Real coefficient of the denominator of the transfer function in s-domain	§5.3.2 p.79
A_L	Area of the large window	§6.4.2 p.141
A_S	Area of the small window	§6.4.2 p.141
b	Inner dimension of a cavity in y-direction	§5.5.3.2 Eq. 5.32 p.100
b_i	Digital filter real coefficient that determines feed-forward link	§5.1.2 Eq. 5.3 p.68
b_{ri}	Reflection digital filter real	§5.3.1 Eq. 5.6 p.76

	coefficient that determines feed-forward link	
b_{ti}	Transmission digital filter real coefficient that determines feed-forward link	§5.3.1 Eq. 5.7 p.76
B	Correction factor that accounts for multiple reflections	§3.6.2 Eq. 3.1 p.39
B	Magnetic flux density	§3.7 p.40
B_i	Real coefficient of the numerator of the transfer function in s-domain	§5.3.2 p.79
$BW_{Gaussian}$	The 60dB-bandwidth of Gaussian pulse	§6.2.2.1.2 Eq. 6.6 p.132
c	Speed of light in free space ($c = 299792458$m/s)	§5.2.2 p.72
C	Capacitance per unit distance	§2.3 p.15
C_{DF}	Total number of TLM cells (nodes) for the DF setup	§5.7 Eq. 5.35 p.113
C_m	Total number of TLM cells (nodes) for the fine mesh setup	§5.7 Eq. 5.35 p.113
d	Inner dimension of a cavity in z-direction	§5.5.3.2 Eq. 5.32 p.100
dl	Space discretisation (also space step or space segment)	§5.2.2 p.71
dl_{DF}	Space step for the coarse mesh (with DF)	§5.7 Eq. 5.36 p.114
dl_m	Space step for the fine mesh	§5.7 Eq. 5.36 p.114
dt	Time discretisation (also time step)	§5.2.2 p.72
D	Power used to count for the object number of dimensions	§5.7 Eq. 5.36 p.114
D	Electric flux density	§3.7 p.40
E_i	Electric field intensity of the incident wave	§2.4 Fig. 2.2 p.17
E_r	Electric field intensity of the reflected wave	§2.4 Fig. 2.2 p.17
E_{rf}	First reflected electric field from a thin panel	§5.3 Fig. 5.3 p.74
E_{rm}	Total internal progressive reflections inside a thin panel	§5.3 p.73
E_t	Electric field intensity of the transmitted wave	§2.4 Fig. 2.2 p.17
E_{tf}	First transmitted electric field from a thin panel	§5.3 Fig. 5.3 p.74
E_{tm}	Total progressive transmissions through a thin panel	§5.3 p.73
E_x	x-component of E	§6.4.4.1.1 Fig. 6.18 p.147
E_{x_panel}	x-component of transmitted E with the presence of panel	§6.4.4.1 Eq. 6.9 p.146
E_{x_ref}	x-component of transmitted E	§6.4.4.1 Eq. 6.9 p.146

	without the presence of panel	
E_y	y-component of E	§6.4.4.1.1 Fig. 6.18 p.147
E_{y_panel}	y-component of transmitted E with the presence of panel	§6.4.4.1 Eq. 6.10 p.146
E_{y_ref}	y-component of transmitted E without the presence of panel	§6.4.4.1 Eq. 6.10 p.146
E_z	z-component of E	§6.4.4.1.1 Fig. 6.18 p.147
E_{z_panel}	z-component of transmitted E with the presence of panel	§6.4.4.1 Eq. 6.11 p.146
E_{z_ref}	z-component of transmitted E without the presence of panel	§6.4.4.1 Eq. 6.11 p.146
f_c	Cut off frequency	§7.3 Eq.7.1 p.180
f_{max}	Maximum useable frequency	§5.5.2.1.1 p.93
$f_{max\,DF}$	Maximum useful frequency for coarse mesh/digital filter setup	§5.7 Eq. 5.38 p.114
f_{min}	Minimum useful frequency	§6.2.2.1 p.127
f_{mnp}	Analytic value of the resonant frequency at mode mnp	§5.5.3.2 Eq. 5.32 p.100
f_o	Frequency at which conductivity equals $G_o/2$	§7.7 Eq.7.6 p.194
f_{sp}	Split frequency (splits the two behaviours apart)	§6.4.4 p.145
F	Correction factor accounts for time delay of running DF routine	§5.7 Eq. 5.35 p.113
G_o	Complex conductivity at DC in Drude model	§7.7 Eq.7.5 p.194
$h(n)$	Unit impulse response in discrete-time domain	§5.1.2 p.68
$H(\omega)$	Frequency response	§5.3.2 Fig. 5.6 p.80
$H(s)$	Transfer function in the s-domain	§5.3.2 Eq. 5.13 p.79
$H(z)$	z-transform of the unit impulse response	§5.1.2 p.68
H_i	Magnetic field intensity of the incident wave	§2.4 Eq. 2.8 p.18
H_r	Magnetic field intensity of the reflected wave	§5.3.1 Fig. 5.5 p.78
H_t	Magnetic field intensity of the transmitted wave	§2.4 Eq. 2.8 p.18
i	Input current to a transmission-line section	§2.3 p.15
I_R	Received current	§7.3 p.178
I_S	Source current	§7.3 p.178
j	$\sqrt{-1}$	§5.1.2 Eq. 5.2 p.68
J	Current density per unit area	§2.3 p.16
J_o	Amplitude of the sinusoidal current density	§2.3 p.16
k	Integer number	§4.6 p.55
$_kV^i$	Incident voltage at kth iteration	§4.6 p.55
$_kV^r$	Reflected voltage at kth iteration	§4.6 p.56

L	Inductance per unit distance	§2.3 p.15
L_1	Distance between sample and excitation in hollow metallic waveguide	§7.3 p.181
L_2	Distance between sample and receiver in hollow metallic waveguide	§7.3 p.181
L_d	Thickness of a thin panel	§4.9 p.63
L_{min}	Minimum dimension of object under modelling	§5.2.2 p.71
m	Number of half wavelengths in x-dimension	§5.5.3.2 Eq. 5.32 p.100
m_A	Area multiplier	§6.4.2 p.142
m_S	SE improvement in ratio form	§6.4.2 p.142
$\hat{n}$	Unit vector normal and outwardly directed from the cavity walls	§6.4.4.3 Eq. 6.12 p.154
n	Number of half wavelengths in y-dimension	§5.5.3.2 Eq. 5.32 p.100
n_1	Refraction index of medium 1	§5.3.1 Fig. 5.5 p.78
n_o	Refraction index of medium 0	§5.3.1 Fig. 5.5 p.78
N	Integer number	§5.7 p.113
NP	Number of poles	§5.1.2 p.69
NPr	Number of poles of reflection DF	§6.3 Table 6.1 p.136
NPt	Number of poles of transmission DF	§6.3 Table 6.1 p.136
N_s	Number of samples used in `invfreqs.m`	§5.3.2.1 p.80
NT	Total number of iterations	§4.6 p.56
NT_{min}	Minimum number of iterations for a complete pulse reflection	§6.2.1.2.2 Eq. 6.4 p.125
NX	Number of TLM nodes in the x-dimension of the object	§5.7 p.113
NY	Number of TLM nodes in the y-dimension of the object	§5.7 p.113
NZ	Number of zeros	§5.1.2 p.69
NZ	Number of TLM nodes in the z-dimension of the object	§5.7 p.113
p	Number of half wavelengths in z-dimension	§5.5.3.2 Eq. 5.32 p.100
R	Resistance per unit distance	§2.3 p.15
R	Reflection loss in dB	§3.6.2 Eq. 3.1 p.39
R_L	Load resistance	§5.4.1 Eq. 5.15 p.85
R_S	Source resistance	§5.3 Fig. 5.4 p.75
S	Simulation speedup	§5.7 p.113
S_{21}	Transmission S parameter	§1.3 p.6
S_{21}^{panel}	Transmission S parameter with the presence of the panel	§6.5 p.160
S_{21}^{ref}	Transmission S parameter	§6.5 p.160

	without the presence of the panel	
SE_x	x-component of SE	§6.4.4.1 Eq. 6.9 p.146
SE_y	y-component of SE	§6.4.4.1 Eq. 6.10 p.146
SE_z	z-component of SE	§6.4.4.1 Eq. 6.11 p.146
t	Time variable	§2.3 p.15
T	Time delay by one sample	§5.1.2 Eq. 5.2 p.68
T	Transmission coefficient	§5.3 p.74
T	The ABCD matrix	§5.4.1 Fig. 5.9 p.85
T1	Field point that receives at $\theta = 0^o$	§5.5.1 Fig. 5.10 p.88
T2	Field point that receives at $\theta = 25.5^o$	§5.5.1 Fig. 5.10 p.88
T_{eDF}	Elapsed run time of digital filter simulation	§5.7 Eq. 5.34 p.113
T_{em}	Elapsed run time of fine mesh simulation	§5.7 Eq. 5.34 p.113
T_S	Simulation time	§5.7 p.115
t_{T1}	Pulse propagation delay to reach point T1 from excitation	§5.5.3.5 p.103
t_{T2}	Pulse propagation delay to reach point T1 from excitation	§5.5.3.5 p.104
u	Speed of light in medium	§4.7.1 Eq. 4.14 p.58
v	Input voltage of a transmission-line section	§2.3 p.15
V_f	Volume fraction of fibre	§3.6.2 Eq. 3.2 p.39
V_i	Input voltage	§7.3 p.178
V_o	Output voltage	§7.3 p.178
V_{out}^{panel}	Voltage received at output point with the presence of the panel	§6.5 Eq. 6.13 p.160
V_{out}^{ref}	Voltage received at output point without the presence of the panel	§6.5 Eq. 6.14 p.160
V_r	Volume fraction of resin (matrix)	§3.6.2 Eq. 3.2 p.39
V_S	Source voltage	§5.3 Fig. 5.4 p.75
x	Distance variable	§2.3 p.15
Z_o	Characteristics impedance of free space	§4.7 p.56
Z_1	Characteristics impedance of a medium/material	§5.2.1 Fig. 5.2 p.71
Z_F	Output impedance of digital filter F	§5.4 Fig. 5.8 p.84
Z_G	Input impedance of digital filter G	§5.4 Fig. 5.8 p.84
Z^{-k}	Delay by k samples in the z-domain	§5.1.2 Eq. 5.3 p.68
Z_L	Load impedance	§5.3 Fig. 5.4 p.75
Z_S	Source impedance	§5.4 Fig. 5.8 p.84

II. Acronyms

The following acronyms are used throughout this thesis.

Symbol	Description	First use
ASTM	American society for testing and materials	§7.3 p.177
CAI	Compression after impact	§3.4.6 p.31
CFC	Carbon fibre composite	§1.1 p.3
DF	Digital filter	§5.1 p.67
DFT	Discrete Fourier transform	§4.9 p.61
DL	One-dimensional DF setup when the excitation source is at the left of the reader	§5.5.4.1 p.106
DR	One-dimensional DF setup when the excitation source is at the right of the reader	§5.5.4.1 p.106
EM	Electromagnetic	§2.4 Fig. 2.2 p.16
EMC	Electromagnetic compatibility	§1.1 p.2
EMI	Electromagnetic interference	§1.1 p.2
FDTD	Finite difference time domain	§4.1 p.50
FE	Finite element	§4.1 p.50
FFT	fast Fourier transform	§5.5.1.1 p.90
FIR	Finite impulse response	§5.1.1 p.67
GTEM	Gigahertz transverse electromagnetic	§8.2 p.210
IEEE	Institute of Electrical and Electronics Engineers	§5.5.2.1.4 p.96
IIR	Infinite impulse response	§5.1.1 p.67
KCL	Kirchhoff's current law	§2.3 p.15
KVL	Kirchhoff's voltage law	§2.3 p.15
M	Matched boundary	§5.5.1 Fig. 5.10 p.88
ML	One-dimensional fine mesh setup when the excitation source is at the left of the reader	§5.5.4.2 Fig. 5.30 p.108
MoM	Method of moment	§4.1 p.50
MR	One-dimensional fine mesh setup when the excitation source is at the right of the reader	§5.5.4.2 Fig. 5.30 p.108
PEC	Perfect electric conductor	§5.5.1 Fig. 5.10 p.88
PMC	Perfect magnetic conductor	§5.5.4.1 p.107
PML	Perfectly matched layer	§4.5 p.55
RAM	Radiation absorbing material	§2.2 p.14
RF	Radio frequency	§7.4 Table 7.1 p.183
SCN	Symmetrical condensed node	§4.7 p.56
SE	Shielding effectiveness	§2.4 p.17
SE_e	Electric shielding effectiveness	§2.4 p.17
SE_m	Magnetic shielding effectiveness	§2.4 p.17
TE	Transverse electric	§5.5.1.1 p.91
TEM	Transverse electromagnetic	§5.5.4.2 p.109

TLM	Transmission-line modelling	§1.1 p.2
TM	Transverse magnetic	§6.2.2.2 p.132

List of Figures

The captions of the figures used in the thesis are stated here.

List of Tables

The captions of the tables used in the thesis are stated here.

1

Research Plan

This chapter presents an overview of this study. It starts with a concise work plan supported with some representative references. More references will be cited in the relevant chapters. The project objectives are stated afterwards, followed by the thesis organisation structure.

1.1 Road Map of the Work Plan

The electromagnetic environment is an integral part of the world in which we live. The emergence of digital electronic systems has called for the necessity to reshape the electronic systems in a way to cope with resultant Electromagnetic Interference (EMI). Moreover, possible harmful effects due to EMI were increased with the developments of the wireless technologies. The goal of coping with EMI has triggered the need to understand the EMI generation and effects. This has lead to the emergence of the science of Electromagnetic Compatibility (EMC) [1.1-1.4] which investigates the means of minimising the harmful effects of EMI by various ways. One treatment is by using electromagnetic shields. These shields should be implemented from special material in a special structure to be suited for a particular application in a given environment. This has necessitated the need to understand the "behaviour" of shields. Understanding practical systems can be accomplished by modelling them. Here, electromagnetic numerical models [1.5] have to be developed. There is a number of candidate techniques that can serve this purpose. Each technique has its own strong aspects and weaknesses. This makes some technique superior to others for a specific case. Among these approaches, the Transmission-Line Modelling (TLM) method [1.6-

1.7] was found to be effective for the cases studied here. The last years have witnessed the introduction of newly designed customised materials to be used as shields. Reference [1.8] has used these materials as shields of EMI in aerospace structures. Reference [1.9] presented their numerical simulation when used for EMI shielding. Reference [1.10] has studied their shielding effectiveness. Reference [1.11] has suggested the use of activated carbon fibres to increase their shielding effectiveness. Reference [1.12] has studied the shielding effectiveness of their woven structure type. Reference [1.13] has studied their shielding properties in avionic systems. The major drive for this tendency is their attractive material properties that attempt to fulfil the modern industrial requirements of producing strong and light products. These customised materials are composites of more than one constituent material. A promising example of composites is the Carbon Fibre Composite (CFC) panels that are formed of a number of thin layers stacked together [1.14-1.22]. This has initiated a technical computational problem to model CFC panels. Therefore, there were researches trying to cope with thin structures whether they are thin panels within the system or thin layers within the CFC panels. A suggested treatment is the use of digital filters [1.23-1.25] that resemble the behaviour of these physical tiny structures rendering them into a mathematical entity within the model of the entire system. Digital filters were used with materials having frequency-dependent properties. Also, digital filters were used to characterise thin structures in EMC problems. The concept of digital filtering [1.26-1.29] provides the capability of cascading different structures and thereby

forming a combination of structures of various features. Having developed a theoretical model based on electromagnetic properties, the next step is to develop the confidence that this model is reliable in representing the shield system. Such confidence can be achieved by validating the developed models. There is no analytic solution ready for all practical objects apart from some limited cases when solving a simple structure. This leads us to adopt the experimental measurements [1.30] as an available choice. By conducting experimental sessions, the error between the model and the laboratory results should be examined. Until the error becomes acceptable [1.31], further modifications are required for the developed model. If the error is acceptable, the modelling approach can get a confidence and used within the presumed constraints. Conclusions now can be drawn regarding what have been achieved out of the main objectives that were set at the start of the work and carried out according to this road map of the research plan.

1.2 Project Objectives

The research work is focused on the modelling of the electromagnetic properties of materials, in particular at microwave frequencies. Typical materials are the composite materials. The objectives of this research project are:

- Develop and investigate numerical models of such materials to predict electromagnetic properties of large-scale behaviour,

- Tackle the case of cascades of different structures within the same system,

- Save computational efforts required in modelling thin embedded structures,

- Validate the simulated models experimentally using practical objects and materials,

The outcome will be a better understanding of how to use materials for electromagnetic design to meet particular specifications.

1.3 Thesis Outline

The purpose of this section is to present an overview of the following chapters.

Chapter 2 presents the subject of electromagnetic compatibility and the theory of electromagnetic shielding. The necessary transmission-line equations are derived to be used in distinguishing the wave behaviour from the diffusion behaviour. The main effects of frequency on the shielding effectiveness are explained.

Chapter 3 introduces the composite materials in general and the Carbon Fibre Composite (CFC) material in particular. The two main constituents of composite material are explained. Its strong points are demonstrated and its limitations are highlighted along with some possible treatments for improvements. A number of applications are stated including the electrical applications as shields. The CFC structure and features are given. The anisotropy feature is presented along with how it can affect their modelling. A brief word is stated regarding the future of CFC.

Chapter 4 reviews briefly the theory of the Transmission-Line Modelling (TLM). It classifies numerical modelling methods in terms of

the working domain and the mathematical operator. The advantages and weak points of the TLM method are stated. The scattering and the connection formulae are presented. The boundary representation is discussed for the cases of boundaries used in this project. At the end, some practical issues in implementing the TLM method are highlighted.

Chapter 5 describes how the digital filters can be applied to represent the tiny structures embedded within the object under modelling. It starts with introducing the concept of digital filtering. Thin panels are then presented as the structures that need some special treatment when modelled. Digital filter implementation and cascading is exemplified through a detailed example, through which comparisons were made between the derived digital filters and the corresponding conventional fine mesh. The stability issue is discussed. The chapter ends with deriving a formula that predicts the speedup rate in terms of the run time when using digital filters.

Chapter 6 is the main result part. It starts with choosing the simulation parameters and the post-processing settings. Verification with fine mesh is provided for a three-dimensional geometry. The main two aspects of simulations are the shielding effectiveness and the transmission S parameter (S_{21}). Results are stated concerning the change of conductivity, dimensions, mesh size, and the effect of monopoles. The character of shielding effectiveness variation with frequency is analysed.

Chapter 7 is concerned with the experimental measurements that were used to validate the developed models. It starts with an overview of other available measurement methods. Then a comparison is presented

between the method used in this study and the already known methods in the literature. A number of advantages over the reviewed methods are found in the method adopted in this study. The experimental configuration and the procedure are stated. The measurements are analysed and compared with the simulated results. It was found that the measured panels show frequency-dependent characteristics. Therefore, a Drude model was derived that supports the measurement results.

Chapter 8 starts with an overall discussion of the main results. Suggestions for future work are stated. The final conclusion of the research project is then given.

The main achievement of this work is the application of digital filtering techniques for studying the shielding effectiveness of thin panel consisting of several layers of composite material. The resulting reduction on computational costs has been evaluated. The efficiency of this approach has permitted the study by numerical simulation of the shielding effectiveness of complex practical structures and thus gave an insight on electromagnetic shielding. This has lead to acquiring better understanding of the electromagnetic behaviour of shields to EMI. Such understanding can lead to more efficient use of shields. Moreover, this is the first time cascaded materials have been put in TLM thin panel models, where throughout this work, the formulae of cascading digital filters were derived and used successfully.

On the practical side, measurements were conducted for an anisotropic material (CFC material) using a method that supports multiple modes over broader range of frequencies with less hardware equipment.

References

[1.1] K.L. Kaiser, *Electromagnetic Compatibility Handbook*. CRC Press, Boca Raton, 2005.

[1.2] C.R. Paul, *Introduction to Electromagnetic Compatibility*. John-Wiley and Sons, New York, second ed., 2006.

[1.3] C. Christopoulos, *Principles and Techniques of Electromagnetic Compatibility*. CRC Press, Boca Raton., second ed. 2007.

[1.4] H.W. Ott, *Electromagnetic Compatibility Engineering*. John Wiley & Sons Inc, New York, NY, 2009.

[1.5] D.G. Swanson and W.J.R. Hoefer, *Microwave Circuit Modeling Using Electromagnetic Field Simulation*. Artech House, Boston, 2003.

[1.6] W.J.R. Hoefer, *The Transmission-Line Matrix method – Theory and Applications*. IEEE Transactions on Microwave Theory and Techniques, Vol. MTT-33, No. 10. pp.882-893, Oct. 1985.

[1.7] C. Christopoulos, *The Transmission-Line Modeling Method TLM*. IEEE Press, N.Y., 1995.

[1.8] J.R. Gaier, *Intercalated Graphite Fiber Composites as EMI Shields in Aerospace Structures*. IEEE Transactions on Electromagnetic Compatibility, Vol. 34, No. 3, pp.351-356, Aug 1992.

[1.9] V. Trenkic, C. Christopoulos and T. Benson, *Numerical Simulation of Polymers and other Materials for Electronic Shielding Applications*. Polymat Conference, London. Sep 1994.

[1.10] D.D.L. Chung, *Electromagnetic Interference Shielding Effectiveness of Carbon Materials*. Carbon, Vol. 39, pp. 279-285, 2001.

[1.11] J. Wu and D.D.L. Chung, *Increasing the Electromagnetic Interference Shielding Effectiveness of Carbon Fiber Polymer – matrix composite by using activated carbon fibers*. Carbon, Vol. 40, pp. 445-467, 2002.

[1.12] S.P. Rea, D. Wylie, D. Linton, E. Orr, and J. McConnell, *EMI Shielding of Woven Carbon Fibre Composites*. High Frequency Postgraduate Student Colloq. 2004, pp. 205–210, 2004.

[1.13] S. Rea, D. Linton, E. Orr, and J. McConnell, *Electromagnetic Shielding Properties of Carbon Fibre Composites in Avionic Systems*. Microwave Review, pp. 29-32, Jun 2005.

[1.14] B.D. Agarwal and L.J. Broutman, *Analysis and Performance of Fiber Composites*. John-Wiley & Sons Inc, New York, 1990.

[1.15] H.O. Pierson, *Handbook of Carbon, Graphite, Diamond and Fullerenes: Properties, Processing and Applications*. Noyes Publications, New Jersey, 1993.

[1.16] D.C.L. Chung, *Carbon Fiber Composites*. Butterworth-Heinemann, Boston, 1994.

[1.17] S.T. Peters (ed.), *Handbook of Composites*, Chapman & Hall, London, second ed., 1998.

[1.18] G.W. Milton, *The Theory of Composites*. Cambridge University Press, 2002.

[1.19] P. Delhaès (ed.), *Fibers and Composites*. Taylor & Francis, London, 2003.

[1.20] A. Baker, S. Dutton, and D. Kelly, *Composite Materials for Aircraft Structures*. AIAA Education Series, Virginia, second ed., 2004.

[1.21] J. Cutler, *Understanding Aircraft Structures*. Blackwell Publishing, Oxford, fourth ed., 2005.

[1.22] F.C. Campbell, *Structural Composite Materials*. ASM International, Ohio, 2010.

[1.23] J.D. Paul, C. Christopoulos and D.W.P. Thomas, *Generalized material models in TLM – Part 1: Materials with frequency-dependent properties*. IEEE Transactions on Antennas and Propagation, Vol. 47, pp. 1528-1534, Oct 1999.

[1.24] J.D. Paul, V. Podlozny, D.W.P Thomas and C. Christopoulos, *Time-domain simulation of thin material boundaries and thin panels using digital filters in TLM*. Turkish J. Elect. Eng. Comp. Sci., Vol. 10, no.2, pp.185-198, 2002.

[1.25] J.D. Paul, V. Podlozny and C. Christopoulos, *The Use of Digital Filtering Techniques for the Simulation of Fine Features in EMC Problems Solved in the Time Domain*. IEEE Transactions on Electromagnetic Compatibility, Vol.45, No.2, May 2003.

[1.26] J.G. Proakis and D.G. Manolakis, *Digital Signal Processing*, Prentice-Hall, second edition, 1996.

[1.27] E.C. Ifeachor and B.W. Jervis, *Digital Signal Processing: A Practical Approach*. Prentice Hall, Harlow, England, second edition, 2002.

[1.28] K.V. Rangarao and R.K. Mallik, *Digital Signal Processing: A Practitioner's Approach*. John Wiley & Sons Inc, West Sussex, England, 2005.

[1.29] B.A. Shenoi, *Introduction to Digital Signal Processing and Filter Design.* John Wiley & Sons Inc, New Jersey, 2006.

[1.30] L.F. Chen, C.K. Ong, C.P. Neo, V.V. Varadan and V.K. Varadan, *Microwaves Electronics: Measurement and Material Characterisation*. John Wiley & Sons Inc, New York, NY, 2004.

[1.31] O. Balci, *Verification, Validation, and Certification of Modelling and Simulation Applications*. Proceedings of the 35th conference on Winter Simulation, 2003.

2

Electromagnetic Shielding

This chapter will give the background on the science of electromagnetic compatibility along with the reasons to its emergence. Special attention will be directed to the concept of shielding.

2.1 Introduction

In the last decade, issues of electromagnetic noise have started to be more serious and received more attention. The term "noise" in this study will be used to refer to any electrical signal present in a circuit other than the desired signal. Sources of noise can be classified under three main categories [2.1].

1) *Intrinsic noise*. This includes any random fluctuations within the same physical system.

2) *Man-made noise*. This can be a result from motors, switches, computers, digital electronics, radio transmitters, etc.

3) *Natural disturbances*. These are mainly dominated by lightning and sunspot activity.

The *electromagnetic interference* (EMI) is the undesirable effect of noise.

In the following sections, the science of the electromagnetic compatibility will be introduced. Shielding will be briefly discussed along with its measure, the *shielding effectiveness*.

2.2 Electromagnetic Compatibility

During the last few years, the operating frequency of electronic devices has increased by a significant amount. This reason, accompanied with

the decrease of digital devices threshold and the trend toward designing compact products [2.2] have led to the emergence of the electromagnetic compatibility science as a vital part of the overall process of equipment design.

Electromagnetic compatibility science is concerned with the ability of a system to operate in the presence of electromagnetic interference (EMI) from other electrical equipment and not to interfere with the operation of other equipment or other parts of itself [2.3]. However, if not in all cases, in the majority of cases, the EMI is not cancelled completely but partially.

The aim of EMC research is to increase the immunity to EMI in one or more of the following ways [2.2]. It can be achieved by minimizing EMI at its source, choosing proper layout, design hardware or/and software with inherent immunity to EMI, proper grounding, filtering, and shielding. This study is concerned with the use of shields (also called screens). This can also involve the use of radiation absorbing material (RAM) to protect some parts of the system from EMI. The importance of shields in EMC is due to the high degree of flexibility, where shielding remains under the full control of the designer [2.2]. However, the reduction of EMI is usually achieved with some side effects. Usually EMI can be reduced at the expense of affecting the normal operating characteristics; appearance (due to the special shape of the shielding structure), size and weight (by the amount of the size and the weight of the shield). According to [2.4], shielding is a fundamental step in establishing or improving the EMC of active and of passive devices.

2.3 Shielding Theory

An electromagnetic wave can go through a barrier in two basic forms or processes. The first process is the "leaking" of the electromagnetic energy through apertures. The second is the penetration of the wave energy through the barrier material by diffusion. These two processes usually take place simultaneously. Obviously, if there are no apertures then only diffusion takes place.

Consider the transmission line section that is composed of inductance per unit distance (L), capacitance per unit distance (C), and resistance per unit distance (R) as shown in Figure 2.1. The voltage (v) and current (i) on the line are functions of time (t) and distance (x). By applying Kirchhoff's voltage law (KVL) and Kirchhoff's current law (KCL) and assuming that the length of the transmission line section, Δx, tends to zero we get [2.5]

$$-\frac{\partial v}{\partial x}\Delta x = L\frac{\partial i}{\partial t} \tag{2.1}$$

$$-\frac{\partial i}{\partial x}\Delta x = C\frac{\partial v}{\partial t} + \frac{v}{R} \tag{2.2}$$
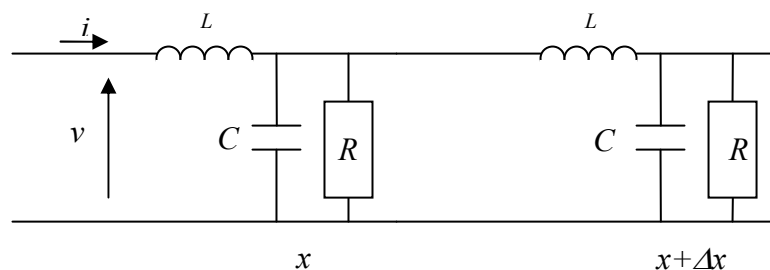
Figure 2.1 A lossy transmission line section used to derive equations 2.1 and 2.2.

By differentiating equation (2.1) and equation (2.2) with respect to t and x respectively, it will be possible to cancel out the voltage term and thereby obtaining

$$\frac{\partial^2 i}{\partial x^2} = \frac{LC}{(\Delta x)^2}\frac{\partial^2 i}{\partial t^2} + \frac{L}{(\Delta x)^2 R}\frac{\partial i}{\partial t} \qquad (2.3)$$

Current density (J) can be determined using

$$\frac{\partial^2 J}{\partial x^2} = \underbrace{\mu\varepsilon\frac{\partial^2 J}{\partial t^2}}_{wave-like\ behavior} + \underbrace{\mu\sigma\frac{\partial J}{\partial t}}_{diffusion-like\ behavior} \qquad (2.4)$$

where μ, ε, and σ are the medium magnetic permeability, electric permittivity, and electrical conductivity respectively. Assuming a sinusoidal signal, the current density will be $J(x,t)=J_o\cos(\omega t-\beta x)$ where ω is the radian frequency, β is the medium phase constant per unit metre, and J_o is the amplitude of the sinusoidal current density . Now, equation 2.4 will be

$$-\beta^2 J(x,t) = -\mu\varepsilon\omega^2 J(x,t) - \mu\sigma\omega\, J_o\sin(\omega t - \beta x) \qquad (2.5)$$

Thus,

$$\frac{|wave\ term|}{|diffusion\ term|} = \frac{\omega\varepsilon}{\sigma} \qquad (2.6)$$

This means that if $\omega\varepsilon \gg \sigma$ then wave behaviour dominates, while if $\omega\varepsilon \ll \sigma$ then diffusion behaviour will be the dominating factor, which is the case with good conductors [2.6]. In this study, the ratio described in equation (2.6) ranges between the order of 10^{-6} and 10^{-3}. This means that throughout this work, if we are considering ordinary lossy materials then for penetration through the barrier the diffusion mode dominates.

2.4 Shielding Effectiveness

A shield is a material, which is conductive or includes some conductive parts. This material is used to block or at least attenuate the electromagnetic radiation power in order to reduce the electromagnetic interference effects in a process called shielding [2.2]. Figure 2.2 illustrates the basic concept of shielding.
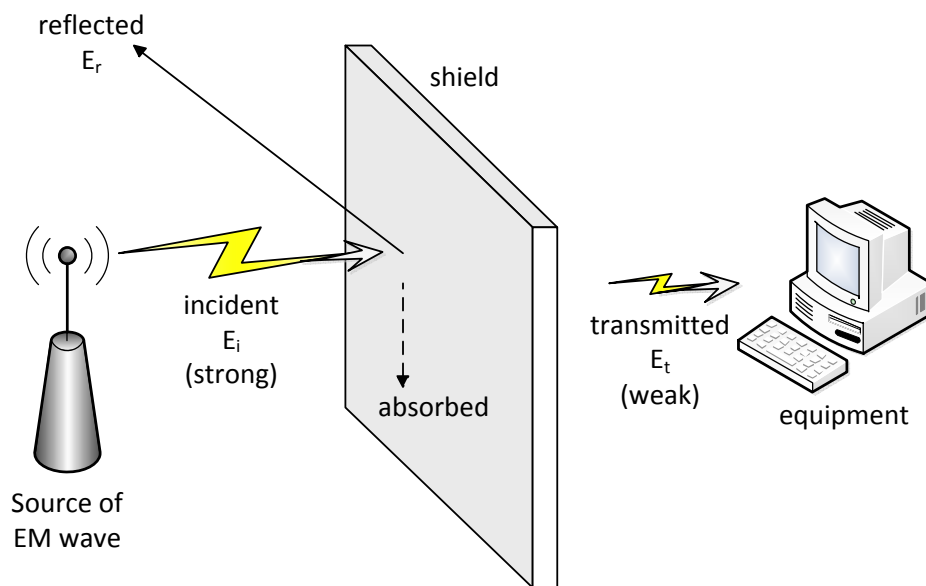
Figure 2.2. The concept of shielding in its general form. Notice that either the source or the equipment can be the device required to be shielded.

In general, the efficiency of shielding is characterized by its shielding effectiveness [2.7]. The shielding effectiveness (SE) basic definition is the ratio of the electromagnetic field without the presence of the shield (which is the field incident into the shield, $\mathbf{E_i}$) to the field in the presence of the shield (which is the field transmitted through the shield, $\mathbf{E_t}$). The two common definitions for shielding effectiveness are the electric shielding effectiveness (SE_e) and the magnetic shielding effectiveness (SE_m) given by [2.2]

$$SE_e = 20\log\left|\frac{\overline{E}_i}{\overline{E}_t}\right| \qquad\qquad (2.7)$$

$$SE_m = 20\log\left|\frac{\overline{H}_i}{\overline{H}_t}\right| \qquad\qquad (2.8)$$

However, Klinkenbusch [2.4] has pointed out to two other definitions of shielding effectiveness to be used with enclosures. They are combinations of SE_e and SE_m. They are called the electromagnetic shielding effectiveness and the transient shielding effectiveness.

Shielding effectiveness varies depending upon a number of parameters such as material conductivity, permittivity, permeability, thickness, geometry of the panel, the surroundings and the distance between the electromagnetic radiation source and the shield and the distance between the shield and the equipment. A typical acceptable value of shielding effectiveness in most of the practical problems is between 50dB and 60dB [2.2].

In addition to the experimental method to find the SE, various techniques have been developed to find the SE by analytical and numerical approaches. One of the numerical methods will be the subject of Chapter 4.

2.5 Frequency Effects

Since almost every practical shield contains apertures [2.4], the electromagnetic radiation will penetrate into the interior of the shield and then interfere with the device that supposed to be shielded. This is due to the small size of the operating wavelength which becomes comparable

with the unavoidable apertures that result from the fabrication of the shield e.g., in the joints of the lid to the rest of the shield. Other effects are the resonances within the shielded equipment. Since resonant frequencies tend to be more numerous at higher frequencies, more complex shielding behaviour is obtained at these high frequencies. On the other hand, at low frequencies (approaching the DC), where high values of conductivity and permeability are required to produce some shielding effectiveness [2.4], the electric and magnetic shielding effectiveness are generally not related. In this case, if the shield is thin (its thickness is much less than the skin depth) then it will not provide magnetic shielding if it is a non-magnetic material (relative permeability, μ_r is about one). The skin depth (δ) is the depth that a wave at a given frequency (ω in radian per second) will penetrate a specific material till the wave amplitude decays by 1/e (which is around 0.37). It is given by [2.2]

$$\delta = \sqrt{\frac{2}{\omega\mu\sigma}} \qquad (2.9)$$

A thick shield may provide a degree of magnetic shielding effectiveness if its relative permeability is much higher than one [2.8]. From what is mentioned, one can conclude, broadly speaking, that the permeability is the dominant factor that affects the magnetic shielding effectiveness at low frequency, while at high frequency; the material conductivity is the dominant factor that affects the electric shielding effectiveness [2.2].

2.6 Summary

This chapter has introduced the science of electromagnetic compatibility (EMC) and electromagnetic interference (EMI). Shielding from interference at low- and at high-frequencies was discussed. Accordingly, the key characteristics were identified for specifying the right shield for a given frequency and shield material. The shielding effectiveness was introduced as a measure that describes the effectiveness of a shield in reducing the penetration of EMI.

References

[2.1] H.W. Ott, *Electromagnetic Compatibility Engineering*. John Wiley & Sons Inc, New York, NY, 2009.

[2.2] C. Christopoulos, *Principles and Techniques of Electromagnetic Compatibility*. CRC Press, Boca Raton., 2nd ed. 2007.

[2.3] N. Storey, *Electronics: A system approach*. Pearson, Harlow, 4th ed. 2009.

[2.4] L. Klinkenbusch, *On the Shielding Effectiveness of Enclosures.* IEEE transactions on electromagnetic compatibility, Vol.47, No.3 Aug 2005, pp. 589-601.

[2.5] C. Christopoulos, *The Transmission-Line Modeling Method: TLM*. IEEE Press, N.Y., 1995.

[2.6] D.K. Cheng, *Fundamentals of Engineering Electromagnetics*. Addison-Wesley, Reading, 1993.

[2.7] C. Feng and Z. Shen "A Hybrid FD-MoM Technique for Predicting Shielding Effectiveness of Metallic Enclosures With Apertures", IEEE

transactions on electromagnetic compatibility, Vol.47, No.3 Aug 2005, pp. 456-462.

[2.8] M. Robinson, T. Benson, C. Christopoulos, J. Dawson, M. Ganley, A.C. Marvin, S. Porter, and D. Thomas, *Analytical Formulation for the Shielding Effectiveness of Enclosures with Apertures*. IEEE transactions on electromagnetic compatibility, Vol.40, No.3 Aug 1998, pp. 240-248.

3

Composite Materials

This chapter will describe the composite material that was used in the experimental part of this study. Its main features along with its applications will be briefly introduced. Some aspects of modelling will also be introduced.

3.1 Introduction

Advanced composites represent a growing industry due to their distinct advantages over competing metallic materials, including lighter weight, higher strength performance, and corrosion resistance. Composites have been studied extensively over the past decades for a number of reasons. The first is obviously their usefulness, which is characterised in their mechanical characteristics and led to the wide spectrum of applications.

A second reason is that some researchers [3.1] believe that what can be learnt from the field of composites could have far-reaching implications in many fields of science.

A third reason is that as more understanding scientists can have on composites, the more opportunities can arise in solving challenging outstanding questions. This will open new frontiers, e.g., new mathematical tools [3.1].

The next section will give a definition for composite materials along with their constituents and types. Advantages and weak points will be described in §3.3 and §3.4 respectively, which will be followed by the main applications. Section 3.6 is dedicated to the *carbon fibre composite* (CFC) materials. Their modelling difficulties will be presented in §3.7. Lastly, the future of such materials will be briefly described.

3.2 Composite Materials

A composite material can be defined as [3.2] a combination of two or more materials that results in better properties than those of the individual components used alone. In contrast to metallic alloys, each material retains its separate chemical, physical, and mechanical properties. The two constituents (also called phases) usually are: a reinforcement and a matrix. Table 3.1 states the main features of each phase of a general composite material.

Feature	Matrix	Reinforcement
Function	Transfers load into and out of the fibres; maintains the fibres in the proper orientation and spacing to prevent failure of adjacent fibres when one fails; also protects them from abrasion and the environment	Provides the strength and stiffness
Strength	Usually it is weaker	Usually it is harder, stronger and stiffer
Material	Mainly it can be polymer, metal, or ceramic	Glass, polymer, ceramic, carbon, and sometimes metallic

Table 3.1. The main features of the matrix and the reinforcement phases [3.2, 3.3, 3.4, 3.5].

3.2.1 The Basic Idea of Composites

As pointed out in more than one source [3.3, 3.6], composites like CFC can be looked at in two ways. Both view points present an attempt to use the fibres as well as the matrix in practical devices.

The first view point is that it is an attempt towards improving the carbon fibres by introducing the matrix. The carbon fibres enjoy a number of attractive properties. However, being tiny and breakable, carbon fibres

24

are delicate to handle. Thus, a solution is to embed them in a matrix which will distribute the mechanical stress.

The second view point is that it is an attempt towards improving the matrix by introducing the carbon fibres. Polymeric materials have good mechanical properties. However, they are insulators and poor thermal conductors. Thus, a solution is to "fill" them with conductive fibres.

On either way, the solution was connecting the microworld (i.e., the carbon fibres) to the macroworld (i.e., the composites).

3.2.2 Matrix Types

The matrix phase (also called the continuous phase) is made mostly[1] of one of the following three material types [3.2, 3.4, 3.5]

- Polymers: They have low strength and stiffness

- Metals: They have intermediate strength and stiffness but high ductility

- Ceramics: They have high strength and stiffness but are brittle

In the case of polymer and metal matrix composites that form a strong bond between the fibre and the matrix, the matrix transmits loads from the matrix to the fibres through shear loading at the interface. In ceramic matrix composites, the objective is often to increase the toughness rather than the strength and stiffness; therefore, a low interfacial strength bond is desirable. However, the type and quantity of the reinforcement determine the final properties. In general, because metal and ceramic matrix composites require very high temperatures and sometimes high

---

[1] Sometimes, a fourth type matrix can be made from carbon. The carbon-type matrix is also brittle, just like the ceramic-type matrix.

pressures for processing [3.2], they are normally much more expensive than polymer matrix composites. However, they have much better thermal stability, an important requirement in applications where the composite is exposed to high temperatures.

3.2.3 Reinforcement Types

In terms of the geometrical shape, reinforcement phase can be one of two types: particulate and fibre type. Table 3.2 states the main differences between the two types.

Feature	Particulate Reinforcement	Fibre Reinforcement
Dimensions	Dimensions are approximately equal in all directions	Length is much greater than its diameter
Geometry	Geometry can be spherical, platelets or any other regular or irregular geometry	The ratio of length to diameter is greater than ten in practical
Strength	Much weaker and less stiff than continuous fibre composites	Stronger and stiffer in general
Cost	Much less expensive	Much more expensive
Reinforcement volume percentage	Up to 40-50%	60-70%
Factor that limits the reinforcement volume percentage	Their composites contain less reinforcement due to processing difficulties and brittleness	At higher percentages than 70% there is too little matrix to support the fibres effectively
Material	Typically ceramic with metal matrix	Typically glass, aramid (a polymer), ceramic, carbon, and sometimes metallic

Table 3.2. The main differences between the particulate and the fibre reinforcement [3.2, 3.3, 3.4, 3.7].

Fibre reinforcement can in turn be classified into two types according to their *aspect ratio*, which is the length-to-diameter ratio. These two types of fibres are called continuous and discontinuous fibres. Table 3.3 states

the main differences between the two types of fibre reinforcement. As shown in this table each type has found its own applications according to its structure.

Feature	Continuous Fibres	Discontinuous Fibres
Aspect ratio	Long	Short
Orientation	Normally have a preferred orientation	Have random orientations
Examples	Unidirectional, woven, and helical winding	Examples are chopped fibres and random mat
Strength	Often made into laminates to obtain the desired strength and stiffness	The random alignment reduces its strength and modulus
Cost	Much more expensive	Much less expensive
Uses	Used where higher strength and stiffness are required	Used where the cost is the main driver and strength and stiffness are less important

Table 3.3. The main differences between the continuous and the discontinuous fibre [3.2, 3.4].

From the above overview of types of composites, one can expect many types of composite final products by combining a matrix type with a suitable reinforcement type. For instance, the composite example in this study is the carbon fibre composite. It has a polymer-type matrix and a continuous-fibre-type reinforcement as indicated in Figure 3.1.
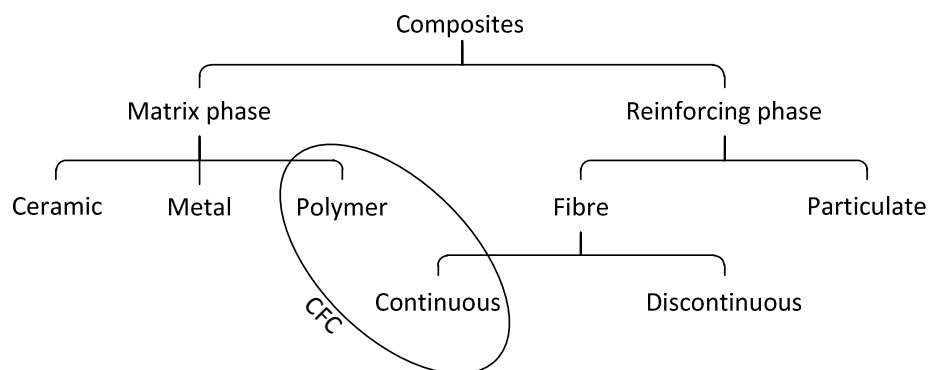
Figure 3.1. The Carbon Fibre Composite (CFC) example is most commonly made of continuous fibres within a polymer matrix.

3.3 Advantages of Composite materials

There are many advantages of composites such as light weight, the ability to tailor the lay-up[2] for optimum strength and stiffness, improved fatigue life, corrosion resistance, and, with good design practice, reduced assembly costs can be achieved due to fewer detailed parts and fasteners.

3.3.1 Strength

The specific strength (strength per density) and specific modulus (modulus per density) of high strength fibres (especially carbon) are higher than those of other comparable aerospace metallic alloys [3.2]. The reason composites are often considered for aircraft design is because of their *strength to weight ratio* [3.8]. A high strength to weight ratio will result in a lighter aircraft structure. This translates into greater weight savings resulting in improved performance, greater payloads, longer range, and fuel savings.

3.3.2 Corrosion Resistance

Corrosion of aluminium alloys is a major cost and a constant maintenance problem for both commercial and military aircraft [3.2]. The high corrosion resistance of composites can result in major savings in supportability costs.

---

[2] A lay-up is the stack of a number of composite layers. Each layer is one sheet of a matrix with embedded reinforcement material. Further explanation will be stated in §3.6.1 for the CFC case.

3.3.3 CFC Fatigue

As long as reasonable strain levels [3.2] are used during design, fatigue of carbon fibre composites should not be a problem.

3.4 Limitations and Drawbacks

The disadvantages of composites include high raw material costs and usually high fabrication and assembly costs; adverse effects of both temperature and moisture; poor strength in the out-of plane direction where the matrix carries the primary load; susceptibility to impact damage and delaminations (ply separations); and greater difficulty in repairing them compared to metallic structures. However, the proper selection [3.2] of materials (fibre and matrix), product forms, and processes can have a major impact on lowering the cost of the finished part.

In this section some important drawbacks of composites are discussed briefly. The anisotropy effect is addressed in §3.7.

3.4.1 Fabrication and Assembly Cost

The major cost driver in fabrication for a composite part using conventional hand lay-up is the cost of laying up the plies (layers). This cost is generally 40 to 60 percent [3.2] of the fabrication cost, depending on part complexity. Assembly cost is another major cost driver. However, one of the potential advantages of composites is the ability to cure or bond a number of detail parts together to reduce assembly costs and the number of required fasteners.

3.4.2 Temperature

Temperature has an effect on composite mechanical properties. Typically, matrix-dominated mechanical properties decrease [3.2, 3.9] with increasing temperature. Fibre-dominated properties are somewhat affected by cold temperatures, but the effects are not as severe as those of elevated temperature on the matrix-dominated properties.

3.4.3 Humidity

The amount of absorbed moisture depends on the matrix material and the relative humidity. Elevated temperatures increase the rate of moisture absorption. Absorbed moisture reduces the matrix-dominated mechanical properties and causes the matrix to swell [3.2, 3.9], which relieves locked-in thermal strains from elevated-temperature curing.

3.4.4 Delaminations

Composites are susceptible to delaminations (ply separations) during fabrication, during assembly, and in service [3.2, 3.3, 3.9]. During fabrication, foreign materials can be inadvertently left in the lay-up. During assembly, improper part handling or incorrectly installed fasteners can cause delaminations. In service, low-velocity impact damage from dropped tools or forklifts running into aircraft can cause damage.

3.4.5 Environmental degradation

Exposure of composites to various environmental conditions may or may not cause degradation, depending on the specific material system and the specific environment. However, when environmental degradation does occur, it is usually, but not always, the matrix that is affected [3.2].

In addition to humidity and temperature (discussed above) other environmental effects can change the properties of the composites. These include [3.3] wind conditions, rainfall, ultraviolet and infrared radiation levels. Aircraft components are also subjected to a wide range of chemicals, including fuel and paint.

3.4.6 Strain Limit

Carbon fibre composite has low strain limit in compression [3.10]. This is because its CAI (Compression After Impact) is weaker than metal [3.11]. This has limited its use as a primary structure in aircraft manufacturing. However, a number of methods have been suggested to improve the matrix toughness [3.9].

3.4.7 Electrical Conductivity

The conductivity of CFC in general is nearly 1000 times lower than that of most metals [3.12]. Therefore, it might explode [3.8] when struck by lightning, which its current can reach up to 200 kA [3.13] for a direct attachment. This is because of the generated heat inside the composite due to the dissipation of such a high current in the relatively high resistance of the composite material. Aeroplanes and yacht masts made

of carbon fibre must be fitted with lightning conductors unless the cross-sections of the components are so big that they can absorb a lightning strike without overheating. For aircraft this usually means building copper conductors into the wing around carbon spars or adding a conductive layer, such as aluminium mesh, over the outside of the whole aircraft [3.8].

Electromagnetic wave absorbing fillers (made from the Radiation Absorption Material, RAM) can be used [3.14] in producing composites with enhanced electromagnetic shielding performance as it is the case of carbon fibre composites.

3.5 Applications

Due to the decreasing price of carbon fibres, the applications of carbon fibre composites are rapidly widening to include the aerospace, automobile, marine, construction, biomedical, and other industries. In general, high-performance but more costly CFC materials are used where high strength and stiffness along with light weight are required, and much lower-cost fibreglass composites are used in less demanding applications where weight is not as critical.

3.5.1 Aerospace

In military aircraft, low weight is a key factor for performance and payload reasons, and composites often approach 20 to 40 percent [3.2] of the airframe weight. In recent years helicopter airframes have been built largely from carbon-fibre composites. Both small and large commercial

aircraft rely on composites [3.2, 3.3, 3.8] to decrease weight and increase fuel performance, the most striking example being the 50 percent composite airframe for the new Boeing 787 (The Dreamliner) where its first test flight took place in December 2009. All future Airbus and Boeing aircraft are expected to use large amounts of high-performance composites. Composites are also used extensively in both weight-critical reusable and expendable launch vehicles and satellite structures. Weight savings due to the use of composite materials in aerospace applications generally range from 15 to 25 percent.

3.5.2 Land transportations

The major automakers are increasingly turning to composites to help them meet performance and weight requirements, thus improving fuel efficiency. Cost is a major driver for commercial transportation, and composites offer lower weight and lower [3.2] maintenance costs.

3.5.3 Marine Transportations

Corrosion is a major expense for the marine industry. Composites help minimize these problems, primarily because they do not corrode like metals or rot like wood [3.2]. Hulls of boats ranging from small fishing boats to large racing yachts are routinely made of glass fibres and polyester or vinyl ester resins. Masts are frequently fabricated from carbon fibre composites.

3.5.4 Construction and Infrastructure

Using composites to improve the infrastructure of roads and bridges [3.2] is a relatively new. Many of the world's roads and bridges are badly corroded and in need of continual maintenance or replacement. Composites offer much longer life with less maintenance due to their corrosion resistance. The blades for large wind turbines are normally made of composites to improve electrical energy generation efficiency.

3.5.5 Recreation

Tennis racquets have been made of glass fibre composites for years, and many golf club shafts are made of carbon fibre composites.

3.5.6 Electrical Applications

Carbon fibre composites are being considered for electromagnetic interference (EMI) shields. This study takes this application in particular and investigates the behaviour of CFC shields by means of deriving high-frequency models that describe their electrical properties. This work can have an impact on reaching better fabrication of the CFC panels designed for a specific purpose to work in given circumstances. Chapter 5 deals with implementing digital filters that represent small embedded structures in the system under modelling. The fibres of the carbon in the CFC materials can be these small embedded structures inside the matrix system. The succession of fibres can be regarded as a cascade system that was the subject in §5.4. In the macroscale, the entire CFC panels can be regarded as the embedded structure (after being

homogenised[3]) within the system under modelling. The stack of a number of CFC layers can be dealt with as a cascade system. Two CFC panels were used in the laboratory measurements (Chapter 7) in order to validate the derived models in this study.

The fibres are sometimes coated with nickel [3.5] by electroplating to increase the electrical conductivity, and moulded in the form of sheets with a specific polymer. Nickel is more commonly used than copper for the coating because of the superior oxidation resistance of nickel [3.9]. Another approach to making composites more highly electrically conducting is to use intercalated graphite fibres. Intercalation is the process of introducing "guest" atoms or molecules between the graphene[4] layers of graphite [3.15].

3.6 Carbon Fibre Composites

A carbon fibre composite (also called graphite fibre composite) material consists of a carbon filamentary phase embedded in a continuous matrix phase [3.3, 3.9]. Epoxy [3.16] is the dominant matrix used for carbon fibre polymer-matrix structural composites. This is mainly due to its high-strength matrix [3.5].

The composites with the highest strength and modulus are the continuous-fibre composites [3.2]. Fibres produce high-strength composites because of their small diameter. As a general rule, the smaller the diameter of the fibre, the higher its strength, but often the

---

[3] Homogenisation will be explained in §3.7.1.
[4] Graphene is a special form of carbon whose structure is one-atom-thick planar sheets of carbon atoms that are densely packed in a honeycomb crystal lattice [3.17]. Thus graphite consists of many graphene sheets stacked together.

cost increases as the diameter becomes smaller. In addition, smaller-diameter high-strength fibres have greater flexibility and are more amenable to fabrication processes such as weaving or forming over radii. There are two main varieties of carbon fibre composites [3.8]. They are called 'high-modulus' and 'high-strength', which are caused by variation of the manufacturing technique.

The matrix of carbon fibre composites can be a polymer, a ceramic, a metal, or carbon itself [3.5] (which produces carbon-carbon composite). The most common matrix materials of carbon-fibre composites are the polymers, also called resins or plastics. Carbon-reinforced polymers are low-density, high-strength, and high-modulus composites with extensive applications, especially in aerospace as mentioned in §3.5.1. Their cost is still relatively high but is gradually decreasing as the fabrication techniques are becoming less labour-intensive.

3.6.1 The CFC Structure

When there is a single ply or a lay-up in which all of the layers or plies are stacked in the same orientation (Figure 3.2.a), the lay-up is called a *lamina*. When the plies are stacked at various angles (Figure 3.2.b), the lay-up is called a *laminate* [3.2]. Continuous-fibre composites are normally laminated materials in which the individual layers, plies, or laminae are oriented in directions that will enhance the strength in the primary load direction. Unidirectional (0°) laminae are extremely strong and stiff in the 0° direction. However, they are very weak in the 90°

direction because the load must be carried by the much weaker polymeric matrix.

0°	0°
0°	90°
0°	+45°
0°	-45°
0°	-45°
0°	+45°
0°	90°
0°	0°
(a) Lamina	(b) Laminate
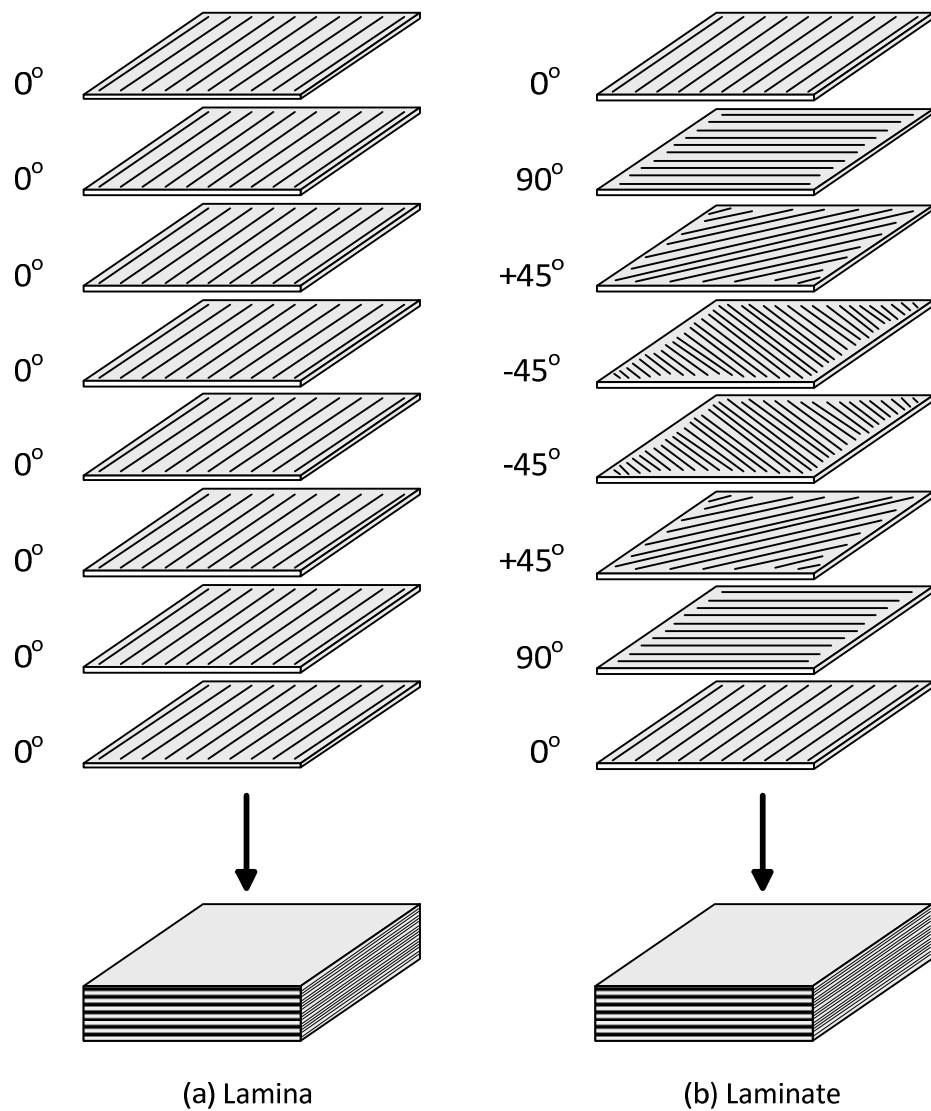
Figure 3.2. Lamina and laminate lay-up structures [3.2]. The stated angle per a given layer represents the orientation of fibres in that layer.

3.6.2 Electrical Properties of Carbon Fibre Composites

When assessing a given material in terms of its electrical properties, there are three parameters that can describe its electrical status. Being a product of composition, CFC properties can vary considerably according to the design. However, typical values of the three properties of the CFC materials are stated as follows.

- Electrical conductivity (σ) of 1.8kS/m [3.18], 10kS/m [3.19], 20kS/m [3.20, 3.21, 3.22], or 28kS/m [3.23] up to around 55kS/m [3.24].

- Electric permittivity (ε) of 1.1 to 5 [3.14, 3.18, 3.23] times the free space permittivity that equals 8.854×10^{-12} F/m

- Magnetic permeability (μ) of that of the free space that equals $4\pi \times 10^{-7}$ H/m. This is because it is not a magnetic material.

The length of the fibre is important in deciding [3.25] the shielding effectiveness (SE). For effective use of the entire cross-section [3.26] of a fibre for shielding, the fibre size should be comparable to or less than the skin depth. Another factor that affects the SE is the fibre content, where at a given frequency, SE is increased with increasing the fibre content [3.25].

Polymer-matrix composites containing fillers are attractive for shielding due to their mouldability, which helps to reduce [3.26] or eliminate the seams in the housing, which forms the shield. This is an advantage over metal shields as they tend to allow leakage of the radiation and diminish the effectiveness of the shield.

CFC materials have lower density [3.23] (1.6 – 2 g/cm^3) than comparable metals (2.5 – 3 g/cm^3). This has allowed for significant weight savings on aircraft. However, unlike metals, CFC materials do not provide high conductivity. Moreover, the conductivity of carbon fibre polymer-matrix composites decreases with increasing frequency [3.9] as will be demonstrated in Figure 7.18. To take an idea about the conductivity of a typical CFC sample, let us consider for example the

sample that was used in [3.23] and [3.27], which is made up of three individual plies of woven CFC. The carbon in each ply is bundled into tows of 6000 filaments. The fibre is continuous and has a diameter of 7 μm. The weight percentage of carbon is approximately 58%. The remainder 42% is a resin that is made of epoxy, which has a dielectric constant of around 4. The density (also called specific gravity) of the carbon and resin are 1.76 g/cm^3 and 1.3 g/cm^3 respectively. The conductivity of the carbon is 55555 S/m and the thickness of the composite panel is 1.14mm. Applying plane wave shielding theory, the total shielding effectiveness of a solid material with no apertures is defined as [3.28]

$$SE_{dB} = A + R + B \qquad (3.1)$$

where A is the absorption loss in dB, R is the reflection loss in dB, and B is a correction factor that accounts for internal multiple reflections within thin shields that were discussed in §5.2.1. This correction factor (measured in dB) may be either positive or negative and is negligible when A is greater than 15dB [3.29].

To calculate the conductivity, the *rule of mixtures* has been suggested and used by a number of references [3.2, 3.23, 3.30]. It states that for a unidirectional continuous-fibre lamina or laminate, the longitudinal (i.e., in the direction parallel to the fibres) property of a composite (in this case electrical conductivity, σ_{cm}) is equal to the conductivity of its component parts weighted by the volume fraction of each part as given by

$$\sigma_{cm} = V_f \sigma_f + V_r \sigma_r \qquad (3.2)$$

where σ_f and σ_r are the conductivity of the fibre and the resin respectively, and V_f and V_r are the volume fraction of fibre and resin respectively.

Assuming a non-conducting resin, σ_r can be set to zero. The volume fraction of the carbon is 0.505. According to equation (3.2) the composite conductivity is found to be 0.505 x 55555 = 28055 S/m. The calculated shielding effectiveness of this panel has given a value of 76dB at 10MHz and it increases to reach 150dB at 1GHz [3.23] and 370dB at 10GHz [3.27].

Another SE example can be obtained from [3.26] where shielding effectiveness of 19dB was obtained over frequencies from 1-2GHz with CFC of 20-percent-volume (V_f=0.2) carbon fibres of 10μm diameter and 400μm length.

CFC panels have found extensive use in the manufacturing of spacecraft structures and their shielding effectiveness was tested [3.31].

3.7 Anisotropy

Anisotropic media exhibit directionally dependent electromagnetic properties [3.32] (in terms of one or more of conductivity, permittivity and permeability). This means, the electric flux density (D) becomes not aligned with the electric field intensity (E) or the magnetic field intensity (H) becomes not aligned with the magnetic flux density (B). In this case, tensors [3.1, 3.33] (instead of scalars) will be needed to relate D with E and H with B.

Anisotropy is not an attribute of all composite materials. For instance, the particulate-reinforced composites are not directional; therefore, properties of particulate composites are essentially isotropic [3.3]. This is due to the random orientation of the particulate reinforcement.

Typically, fibre composite materials exhibit anisotropy. Thus, some properties vary depending upon which geometric axis or plane they are measured along. For a composite to be isotropic in a specific property, such as the conductivity, all reinforcing elements (whether fibres or particles) have to be randomly oriented [3.7]. This is not easily achieved for discontinuous fibres, since most processing methods tend to impart a certain orientation to the fibres. Continuous fibres in the form of sheets are usually used to deliberately make the composite anisotropic in a particular direction that is known to be the principally loaded axis or plane.

3.7.1 Homogenisation

Usually, in modelling CFC, researchers seek to define an equivalent material of single permittivity and single conductivity. The conversion from the actual case to the simplified (homogeneous) structure is referred to as a homogenisation process. The resultant (homogenised) panel will be in the same size and with a single permittivity (and a single conductivity) that is a function of the permittivity (and the conductivity) of both the fibres and the matrix and also a function of the fibre/matrix volume ratio.

According to [3.32], a mixture of two or more different mediums may be viewed as being effectively homogeneous, provided that wavelengths are much longer than the length–scales of the mixture's nonhomogeneities. Homogenisation is important in the interpretation of experimental measurements and in material design [3.32]. A number of procedures of homogenising composites have been proposed [3.33].

3.7.2 Modelling of CFC

Being a complicated substance, the CFC electrical properties (and hence its SE) can not be determined in a straight forward [3.12]. Therefore, full numerical approaches [3.19] should be used to analyse the electromagnetic interaction of a fibre composite. In this study, the Transmission-Line Modelling (TLM) method was adopted due to its attractive attributes (such as its absolute stability) as explained in §4.4. Numerical methods, in general, have good accuracy yet they can impose a heavy burden on the computational effort in terms of time and memory. The reason for that is that the numerical approaches require thin multilayered panels and fibres of composite material to be spatially resolved by very small discretisation steps. These discretisation steps will result in prohibitive computational time and storing memory. More discussion of this subject can be found in §5.2.2. One way to reduce this computational effort is by using digital filters as exemplified in Chapter 5.

To model layers, homogenisation can be applied where an "average" property for the combination of resin and fibres has to be defined [3.3].

This averaging can be applied on a particular layer within the composite panel or on the whole panel [3.19].

3.8 Tailored Composites and the Future

As Milton forecasted ten years ago [3.1], it is getting increasingly possible to produce "designer composites", where the microstructure has been tailored to produce desirable properties. Obviously, a better understanding of the link between the microstructure and the macrostructure properties will be essential in this endeavour. In addition to the microscopic level, tailoring can also be applied at the macroscopic level [3.6], where composites allow tailoring the properties of a given material.

In November 2011, an assessment of the CFC future [3.34] was made by stating that the CFC global demand was roughly £7 billion in 2010, and it was estimated that it will achieve £9 billion by 2012, and is expected to reach £12 billion by 2015 experiencing an average annual growth rate of 8%. The strongest demand is expected in aerospace, wind energy, and automotive manufacturing. The good availability at a reasonable price level of £5-6/kilogram (in November 2011) can trigger a large-scale use of carbon fibre based composites.

3.9 Summary

This chapter has introduced composite materials in general and the carbon fibre composites in particular, which is the material that was used in this study. It was shown that these materials have some attractive

properties that make it competitive with the comparable material in the market. It was also shown that they have some drawbacks that limit commercial use. However, some of these weak points can be overcome. The main applications were reviewed highlighting the properties to be optimised for specific application. The material anisotropy was introduced and it was shown how anisotropy can affect the composite material modelling. One solution to modelling problems is the use of homogenised properties. The chapter concluded with a look at the future of these promising materials.

References

[3.1] G.W. Milton, *The Theory of Composites*. Cambridge University Press, 2002.

[3.2] F.C. Campbell, *Structural Composite Materials*. ASM International, Ohio, 2010.

[3.3] A. Baker, S. Dutton, and D. Kelly, *Composite Materials for Aircraft Structures*. AIAA Education Series, Virginia, second ed., 2004.

[3.4] S.T. Peters (ed.), *Handbook of Composites*, Chapman & Hall, London, second ed., 1998.

[3.5] H.O. Pierson, *Handbook of Carbon, Graphite, Diamond and Fullerenes: Properties, Processing and Applications*. Noyes Publications, New Jersey, 1993.

[3.6] P. Delhaès (ed.), *Fibers and Composites*. Taylor & Francis, London, 2003.

[3.7] Nondestructive Testing (NDT) Resource Center. http://www.ndt-ed.org/EducationResources/CommunityCollege/Materials/Structure/composite_class.htm accessed on 22 Dec 2011.

[3.8] J. Cutler, *Understanding Aircraft Structures*. Blackwell Publishing, Oxford, fourth ed., 2005.

[3.9] D.C.L. Chung, *Carbon Fiber Composites*. Butterworth-Heinemann, Boston, 1994.

[3.10] P. Veers, *Research Directions in Wind Turbine Blades: Materials and Fatigue*. A presentation for GCEP-Stanford University, 2004.

[3.11] P.P.M. So and W.J.R. Hoefer *A General Planar Circuit Simulator Based on Two-Dimensional TLM Method*. Laboratory for Electromagnetics and Microwaves, Department of Electrical Engineering University of Ottawa, 1989, IEEE MTT-S Digest, pp. 343-346.

[3.12] C.L. Holloway, D.A. Hill, J. Ladbury, G. Koepke, and R. Garzia, *Shielding Effectiveness Measurements of Materials Using Nested Reverberation Chambers*. IEEE Transactions on Electromagnetic Compatibility, Vol. 45, No. 2, pp.350-356, May 2003.

[3.13] V. Cooray (ed), *Lightning Protection*. The Institution of Engineering and Technology, London, 2010.

[3.14] C.P. Neo and V.K. Varadan, *Optimization of Carbon Fiber Composite for Microwave Absorber*. IEEE Transaction on Electromagnetic Compatibility, Vol. 46, No. 1, pp.102-106, Feb 2004.

[3.15] J.R. Gaier, *Intercalated Graphite Fiber Composites as EMI Shields in Aerospace Structures*. IEEE Transactions on Electromagnetic Compatibility, Vol. 34, No. 3, pp.351-356, Aug 1992.

[3.16] J. Wu and D.D.L. Chung, *Increasing the Electromagnetic Interference Shielding Effectiveness of Carbon Fiber Polymer – matrix composite by using activated carbon fibers*. Carbon, Vol. 40, pp. 445-467, 2002.

[3.17] Wikipedia, *Graphene*. http://en.wikipedia.org/wiki/Graphene accessed on 7 January 2012.

[3.18] K.H. Wong, *Use of Recycled Carbon Fibre for Electromagnetic Interference Shielding*. PhD thesis, The University of Nottingham, 2006.

[3.19] C.L. Holloway, M.S. Sarto and M. Johansson, *Analyzing Carbon-Fiber Composite Materials With Equivalent-Layer Models*. IEEE Transactions on Electromagnetic Compatibility, Vol. 47, No. 4, pp.833-844, Nov 2005.

[3.20] J. Johns, J. Wlodarcyzk, and A. Mallik, *New TLM Models for Thin Structures*. International Conference on Computation in Electromagnetics, 25-27 Nov 1991, IEE, London. Conference Publication No. 350.

[3.21] A. Mallik and C.P. Loller, *The Modelling of EM Leakage into Advanced Composite Enclosures using the TLM Technique*. International Journal of Numerical Modelling: Electronic Networks, Devices and Fields, Vol. 2, 1989, pp. 241-248.

[3.22] V. Trenkic, C. Christopoulos and T. Benson, *Numerical Simulation of Polymers and other Materials for Electronic Shielding Applications*. Polymat Conference, London. Sep 1994.

[3.23] S.P. Rea, D. Wylie, D. Linton, E. Orr, and J. McConnell, *EMI Shielding of Woven Carbon Fibre Composites*. High Frequency Postgraduate Student Colloq. 2004, pp. 205–210, 2004.

[3.24] CEVP Ltd. Accessed by the following link in 20 Jul 2007 www.cevp.co.uk/cfc_spec_sheet.htm

[3.25] C. Huang and C. Wu, *The EMI Shielding Effectiveness of PC/ABS/Nickel-Coated-Carbon-Fibre Composites*. European Polymer Journal, Vol. 36, pp. 2729-2737, 2000.

[3.26] D.D.L. Chung, *Electromagnetic Interference Shielding Effectiveness of Carbon Materials*. Carbon, Vol. 39, pp. 279-285, 2001.

[3.27] S. Rea, D. Linton, E. Orr, and J. McConnell, *Electromagnetic Shielding Properties of Carbon Fibre Composites in Avionic Systems*. Microwave Review, pp. 29-32, Jun 2005.

[3.28] H.W. Ott, *Electromagnetic Compatibility Engineering*. John Wiley & Sons Inc, New York, NY, 2009.

[3.29] N.C. Das, D. Khastgir, T.K. Chaki, A. Chakraborty, *Electromagnetic Interference Shielding Effectiveness of Carbon Black and Carbon Fibre Filled EVA and NR Based Composites*. Composites – Part A: Applied Science and Manufacturing, Vol. 31, pp. 1069-1081, 2000.

[3.30] B.D. Agarwal and L.J. Broutman, *Analysis and Performance of Fiber Composites*. John-Wiley & Sons Inc, New York, 1990.

[3.31] A.L. Bogorad, M.P. Deeter, K.A. August, G. Doorley, J.J. Likar, and R. Herschitz, *Shielding Effectiveness and Closeout Methods for*

Composite Spacecraft Structural Panels. IEEE Transaction on Electromagnetic Compatibility, Vol. 50, No. 3, pp.547-555, Aug 2008.

[3.32] T.G. Mackay and A. Lakhtakia, *Electromagnetic Anisotropy and Bianisotropy: A Field Guide*. World Scientific, New Jersey, 2010.

[3.33] R. Piat, I. Tsukrov, N. Mladenov, V. Verijenko, M. Guellali, E. Schnack, and M.J. Hoffmann, *Material modelling of the CVI-infiltrated carbon felt I: Basic formulae, theory and numerical experiments*. Composites Science and Technology Vol. 66, pp. 2997-3003, 2006.

[3.34] Omnexus by SpecialChem, *Future Growth of Carbon Fibers Reinforced Plastics*. http://www.omnexus.com/community-pulse/community-insight.aspx?id=29042 accessed on 25 Dec 2011.

4

The Implementation of the Transmission-Line Modelling Method

This chapter briefly introduces the Transmission-Line Modelling (TLM) method as the numerical modelling technique that is adopted in this study. The method is compared to other numerical modelling methods and its strong features are stated with its weak points. Some practical implementation issues will be explained.

4.1 Introduction

Models help us predict the behaviour of components, circuits, and systems. Modelling of a particular object (or system) is the process of generating a conceptual object used in the creation of a predictive formula. This is achieved by presenting a pattern or representation designed to show the object structure [4.1].

Generally, configurations under test may be treated using analytical formulations or approximate techniques (i.e., numerical simulation) [4.2]. However, a numerical simulation is recommended for complex structures, although it requires much computing time and memory. Moreover, it is difficult for designers to investigate the effect of design parameters on the shielding effectiveness [4.3]. Examples of numerical simulation methods are the finite difference time domain (FDTD), method of moment (MoM), finite-element (FE), and the transmission-line modelling (TLM) methods.

4.2 Classifications of Numerical Methods

Numerical modelling methods can be classified according to the working domain into time domain methods and frequency domain methods. The

solution of a numerical method may be in a form of numbers, so if the input is sinusoidal (single frequency), then the transfer function relates to this specific frequency and the problem solution method is denoted as frequency-domain type. Alternatively, if the input signal is in a form of an impulse function (contains all the frequencies) then the impulse response of the system is obtained and the problem solution method is denoted as time-domain type [4.2]. Table 4.1 illustrates the essential differences between the methods of the two domains.

Item	Time-domain method	Frequency-domain method
Result at a single frequency	Less suitable	More suitable
Results at many frequencies or for transient problems	More suitable	Less suitable
Frequency-dependent parameters	Less suitable	More suitable
Non-linearity or time-variation problems	More suitable	Less suitable
Example of a method	FDTD and TLM	FE and MoM

Table 4.1. Comparison between time- and frequency-domain numerical techniques [4.2, 4.4].

For a time-domain method, the excitation waveform is usually a time-domain pulse which contains a broad range of frequencies, which makes it more suitable if results are required at a frequency range. On the other hand, the frequency-domain method excites a single-frequency waveform which makes it more suitable if the results are required at a single frequency. Since the frequency-domain method excites a single frequency waveform, any frequency-dependency feature can be easily identified; therefore, frequency-domain method is more suitable in this

51

regard. In the same way, any time-dependency feature can be easily identified using time-domain method.

Numerical modelling techniques can also be classified according to the operator nature into integral-form and differential-form. A brief comparison between the two forms is shown in Table 4.2.

Item	Integral method	Differential method
Discretisation region	Only structure boundaries (coarse)	Entire volume (fine)
Discretisation resolution	Lower	Higher
Represented details	Thin structures	Thin slots, wires, or films
Resulting equations	Complex	Simpler
Open boundary problem	Quite rigorous (easily obtained)	Approximate techniques (difficult to be obtained)
Inhomogeneous, nonlinear with complex boundaries and apertures	Less suitable	More suitable
Example of a method	MoM	FE, FDTD and TLM

Table 4.2. Comparison between Integral and differential numerical modelling techniques [4.2, 4.4, 4.5].

The discretisation region can cover only the structure boundaries or a specific thin structure within the system with the use of integral methods, where the mesh can be set to be coarse mesh. A higher discretisation resolution is needed with differential methods where the entire volume should be covered by the mesh. Therefore, differential methods are more suitable in modelling thin slots, wires, and films. The mathematical resultant equations of the integral method are harder to be solved, which make it not suitable for any nonlinearity or complex structure but produce a rigorous solution with open boundary problem. On the other hand, simpler equations are obtained with the differential method, which

52

make it more suitable for modelling complex structures but the open boundary problem can only be solved with approximate techniques.

From the above discussion, one can see that each method has its own uses; therefore, for a given application a hybrid method, combining the advantages of each method, may perform better than either one of them. An example is the hybrid method derived from the time-domain TLM and the frequency-domain mode-matching technique. The method adopted in this study is the transmission-line modelling (TLM) method.

4.3 TLM Definition

The transmission-line modelling method (also called transmission-line matrix method [4.5, 4.6, 4.7]) is a time-domain differential-type numerical modelling technique that models the electromagnetic fields by analogy to Huygens's principle (in a discrete form) in both space and time. Thus, it uses an interconnection of transmission-lines. These transmission lines form an equivalent network for the propagation of waves in space. When voltage pulses (pulses are used since it is a time-domain method) travel down the lines, they scatter at the interconnections, which are called nodes [4.5]. The aim of performing the TLM is to determine the voltages at all the transmission line nodes by finding the transient response at these nodes including boundary nodes, where the loads or terminations are located. This also applies to the currents that pass through all the transmission line sections.

4.4 Main Features of the TLM method

The TLM method has a number of features that make it well suited to electromagnetic compatibility (EMC) problems [4.4, 4.8, 4.9].

- *Accurate*. TLM is a discrete model which can be solved exactly; whereas the approximations are only introduced at the discritisation stage. This is a major difference from the tradition approach in which an idealised continuous model is first obtained and then this model is solved approximately [4.10],

- *Simple*. The method is expressed in terms of the already-familiar circuit concepts. Thus, the user has a good knowledge of the properties and behaviour of the model; the nature and significance of errors and the manner in which material properties can be introduced,

- *Stable*. The stability problems do not arise due to the absence of any active components, since the model is a distributed collection of capacitors, inductors and resistors,

- *Flexible*. Increased resolution can be applied only in areas where it is required, which can be done by applying variable mesh size,

- *Efficient*. A single calculation will give information over a wide range of frequencies. Also, the internal as well as external environment can be modelled simultaneously,

- *Wide Applications*. The range of applications includes complex shapes, inhomogeneous materials, and source regions with non-linearities.

4.5 Weak Points of the TLM Method

Normally, every devised method has its own strong features as well as some weak points. This makes it more suited to specific areas of applications at the expense of other areas. However, these points are subjects of researches and a number of treatments were developed to tackle them. Below is a list of a number of weak points [4.8, 4.11].

- The most basic mesh uses uniform cubic cells. This means stair case approximations should be used for curved surfaces,

- Resolving small feature dictates a very fine grid. This leads to heavy computational efforts (memory and time). One treatment is the use of digital filters, which is the subject of Chapter 5,

- Not easy to solve closely spaced resonances. This is because interference between the *sinc* terms associated with the two adjacent resonance peaks can cause an error in the value of the resonance frequency. Therefore it is not recommended with filters,

- Not easy to implement Perfectly Matched Layers (PML) that resemble open boundaries.

4.6 Implementation of TLM

The modelling of electromagnetic fields with the TLM method can be regarded as the application of a discrete version of Huygen's continuous wave model. At each time step, k, voltage pulses, $[_k V^i]$, are incident upon the node from each of the link lines (transmission line sections forming the TLM interconnection of network). These pulses are then

scattered to produce a set of scattered voltages, $[_kV^r]$, which become incident on adjacent nodes at the next time step. The processes of scatter and connect can be written as $[_kV^r] = [S][_kV^i]$ and $[_{k+1}V^i] = [C][_kV^r]$ respectively, where $[S]$ is the scattering matrix and $[C]$ is the connection matrix. The time iterations are repeated for NT times. The constraints that govern the total number of iterations (NT) are discussed in §6.2.1.2.2.

4.7 The Three-Dimensional TLM Node

In its basic form, the symmetrical condensed node (SCN) is the intersection of twelve transmission lines, each of characteristic impedance Z_o. The SCN cube has a side length of Δl *as shown in Figure 4.1. The two polarisations in any direction of propagation are carried on two pairs of transmission lines, which do not couple with each other. The scattering matrix can be derived from Maxwell's equations using the concepts of charge and energy conservation.

As illustrated in Figure 4.1, the labels of the twelve ports were chosen according to reference [4.12]. In this scheme, each port is assigned a three-character name: the first character gives the direction parallel to the link line, the second character can be either "p" or "n" to indicate whether the port is on the positive or negative side of the node, and the third indicates the polarisation. In this way, V_{xpy} refers to the voltage pulse on the link line parallel to the x-axis, on the positive side of the node, polarised in the y-direction.

---

* The dimension of the TLM node (Δl) will be called dl when the TLM is put into implementation in the subsequent chapters.
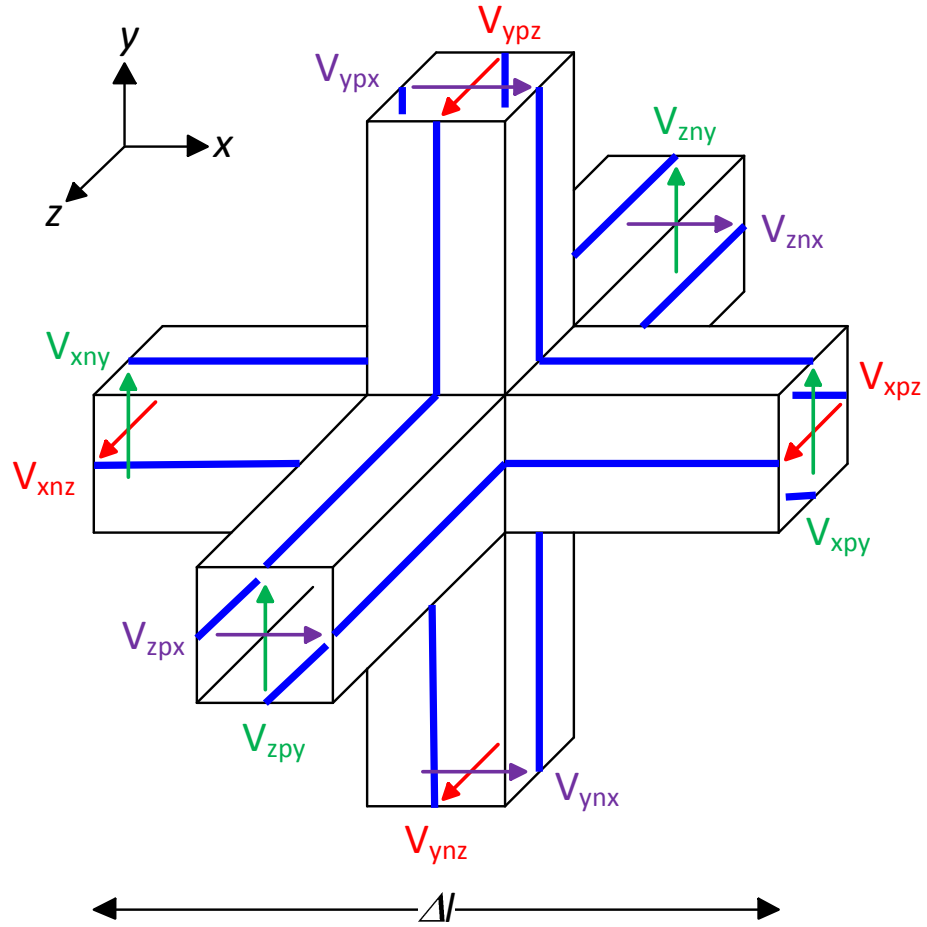
Figure 4.1. The 12-port symmetric condensed node, which is the basic building brick in the three-dimensional models used with the TLM method. The x-, y-, and z-polarised voltages are shown in purple, green, and red respectively.

4.7.1 The Scattering Formulae

The twelve-port node can be used to model regions of space with a uniform mesh. The intrinsic impedance of the medium is determined by the characteristic impedance of the link lines. The scattered pulses are given as:

$$V_{ynx}^{r} = \frac{1}{2}\left(V_{znx}^{i} + V_{zpx}^{i} + V_{xny}^{i} - V_{xpy}^{i}\right) \tag{4.1}$$

$$V_{ypx}^{r} = \frac{1}{2}\left(V_{znx}^{i} + V_{zpx}^{i} + V_{xpy}^{i} - V_{xny}^{i}\right) \tag{4.2}$$

57

$$V^r_{znx} = \frac{1}{2}\left(V^i_{ynx} + V^i_{ypx} + V^i_{xnz} - V^i_{xpz}\right) \tag{4.3}$$

$$V^r_{zpx} = \frac{1}{2}\left(V^i_{ynx} + V^i_{ypx} + V^i_{xpz} - V^i_{xnz}\right) \tag{4.4}$$

$$V^r_{zny} = \frac{1}{2}\left(V^i_{xny} + V^i_{xpy} + V^i_{ynz} - V^i_{ypz}\right) \tag{4.5}$$

$$V^r_{zpy} = \frac{1}{2}\left(V^i_{xny} + V^i_{xpy} + V^i_{ypz} - V^i_{ynz}\right) \tag{4.6}$$

$$V^r_{xny} = \frac{1}{2}\left(V^i_{zny} + V^i_{zpy} + V^i_{ynx} - V^i_{ypx}\right) \tag{4.7}$$

$$V^r_{xpy} = \frac{1}{2}\left(V^i_{zny} + V^i_{zpy} + V^i_{ypx} - V^i_{ynx}\right) \tag{4.8}$$

$$V^r_{xnz} = \frac{1}{2}\left(V^i_{ynz} + V^i_{ypz} + V^i_{znx} - V^i_{zpx}\right) \tag{4.9}$$

$$V^r_{xpz} = \frac{1}{2}\left(V^i_{ynz} + V^i_{ypz} + V^i_{zpx} - V^i_{znx}\right) \tag{4.10}$$

$$V^r_{ynz} = \frac{1}{2}\left(V^i_{xnz} + V^i_{xpz} + V^i_{zny} - V^i_{zpy}\right) \tag{4.11}$$

$$V^r_{ypz} = \frac{1}{2}\left(V^i_{xnz} + V^i_{xpz} + V^i_{zpy} - V^i_{zny}\right) \tag{4.12}$$

For a uniform mesh

$$\Delta l = \Delta x = \Delta y = \Delta z \tag{4.13}$$

and thus the time step can be written as

$$\Delta t = \frac{\Delta l}{2u} \tag{4.14}$$

where u is the speed of light in the medium defined by permeability (μ) and permittivity (ε) as

$$u = \frac{1}{\sqrt{\mu\varepsilon}} \tag{4.15}$$

4.7.2 The Connection Formulae

As noticed from the above discussion, the scattering process finds the reflected (and hence the name scattered) components from the incident components for the same node and at the same time iteration. The connection process, on the other hand, finds the incident components from the reflected components for the adjacent node found at the previous time iteration. Assuming the terminology used in Figure 4.1, the connection formulae will "connect" the scattered voltages to their nearby node. In this way, these same voltages will be the incident voltages at the next time iteration. For a TLM node located at coordinate (x, y, z), the connection formulae concerning its twelve ports are given by

$$_{k+1}V_{xpy}^{i}(x,y,z) = {}_{k}V_{xny}^{r}(x+1,y,z) \qquad (4.16)$$

$$_{k+1}V_{zny}^{i}(x,y,z) = {}_{k}V_{zpy}^{r}(x,y,z-1) \qquad (4.17)$$

$$_{k+1}V_{xny}^{i}(x,y,z) = {}_{k}V_{xpy}^{r}(x-1,y,z) \qquad (4.18)$$

$$_{k+1}V_{zpy}^{i}(x,y,z) = {}_{k}V_{zny}^{r}(x,y,z+1) \qquad (4.19)$$

$$_{k+1}V_{xpz}^{i}(x,y,z) = {}_{k}V_{xnz}^{r}(x+1,y,z) \qquad (4.20)$$

$$_{k+1}V_{ypz}^{i}(x,y,z) = {}_{k}V_{ynz}^{r}(x,y+1,z) \qquad (4.21)$$

$$_{k+1}V_{xnz}^{i}(x,y,z) = {}_{k}V_{xpz}^{r}(x-1,y,z) \qquad (4.22)$$

$$_{k+1}V_{ynz}^{i}(x,y,z) = {}_{k}V_{ypz}^{r}(x,y-1,z) \qquad (4.23)$$

$$_{k+1}V_{znx}^{i}(x,y,z) = {}_{k}V_{zpx}^{r}(x,y,z-1) \qquad (4.24)$$

$$_{k+1}V_{ypx}^{i}(x,y,z) = {}_{k}V_{ynx}^{r}(x,y+1,z) \qquad (4.25)$$

$$_{k+1}V_{zpx}^{i}(x,y,z) = {}_{k}V_{znx}^{r}(x,y,z+1) \qquad (4.26)$$

$$_{k+1}V_{ynx}^{i}(x,y,z) = {_k}V_{ypx}^{r}(x,y-1,z) \qquad (4.27)$$

4.8 Boundary Representation

The boundary conditions [4.4, 4.8, 4.9, 4.12] can be imposed on link lines to model an internal or an external wall. Also, boundary conditions can be imposed at the nodes to model a material with certain properties. Boundary conditions at the node are implemented in the Scattering matrix, while on the link lines; they are implemented in the Connection matrix. An open circuit boundary describes a plane of symmetry that acts like a mirror. In general, the material or a wall can be implemented whether they are lossless ($\sigma = 0$), lossy ($0 > \sigma > \infty$) or perfect conductor ($\sigma \to \infty$). Open boundary is modelled by a load that terminates the mesh node at the boundary side. This load is matched to the medium that bounds the panel under modelling.

4.9 Practical Implementation Issues

A complete process of the application of the TLM method is shown in Figure 4.2. The problem is defined according to the initial requirements. The model is then developed by setting the space discritisation (Δl), initial conditions and the boundary conditions along with the type of excitation. If needed, the preprocessing stage will reshape the input data to the TLM solver so that the input data is within the limits of the solver. The TLM solver apply the scatter-connect operations in an iterative form. The values of the TLM network stored in the output nodes are eventually processed in the postprocessing stage to make it a useful data

that can make sense for the next stage, which interprets them for analysing the outcome. The postprocessing usually applies the discrete Fourier transform (DFT) to transfer the time-domain data into frequency-domain. Sometimes, low-pass filtering and windowing are also applied. The final step is to draw conclusions from the analysed data.
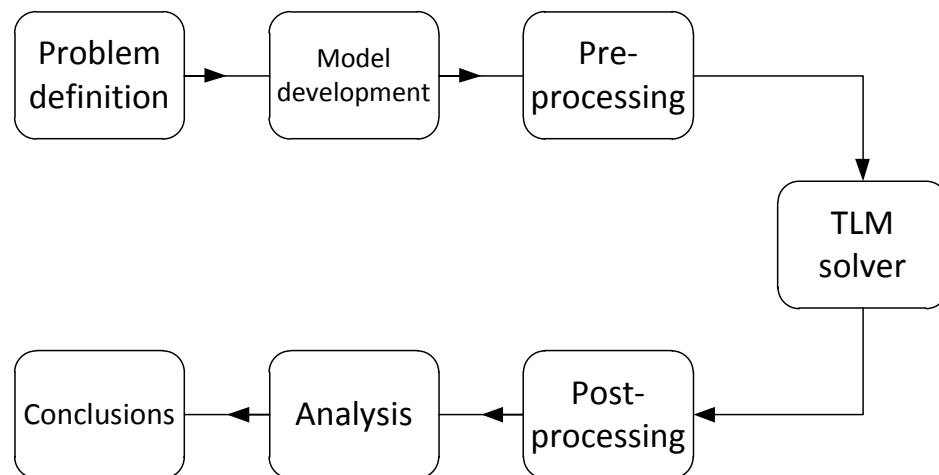
Figure 4.2. General block diagram that is streamlining a practical implementation of a TLM application.

In this study all models were developed using three-dimensional TLM nodes, even the one- and two-dimensional objects. In this case, the time step (Δt) can be obtained from the space step (Δl) by equation (4.14). As mentioned earlier, the space step (Δl) is chosen by the user when setting the model parameters in the second stage (called model development) of Figure 4.2. However, there are some constraints that the user should be aware of. These constraints define the valid range of Δl. These constraints should be determined to avoid excessive error in the results. In the case of the conventional use of TLM (no digital filters are used), two factors should be taken into consideration:

- *Dimensions of the object under modelling.* In order to fully resolve an object there should be typically 5 TLM nodes (Figure 4.3) describing its minimum dimension. In this way, the wave amplitudes are described with enough resolution. Moreover, the lossier the material is, the more TLM nodes will be required to represent the associated dimension. This is because the lossier material produces more dispersive wave. The exception to this is the case of good conductor or perfect conductor, in which case only one TLM node is adequate. A "layer" of free space can also be represented by one TLM node,

$$5 \, \Delta l$$
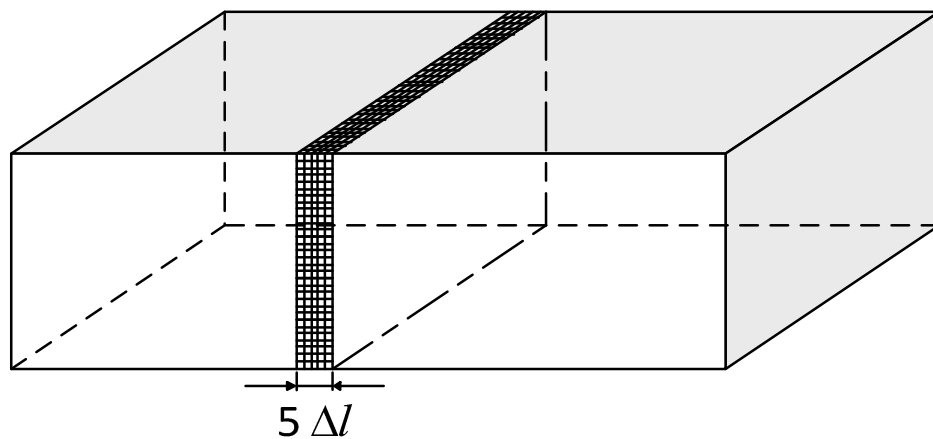
Figure 4.3. The minimum dimension in the object (under conventional modelling) needs to be represented by at least 5 space steps to be resolved.

- *Frequency range of excitation.* In order to resolve a frequency component, it is recommended to represent its wavelength by at least 10 TLM nodes. This defines the minimum useable wavelength (λ_{min}) as illustrated in Figure 4.4,
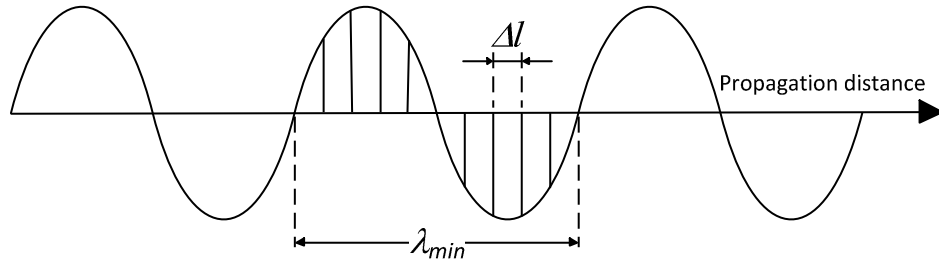
Figure 4.4. The minimum useful wavelength needs to be represented by at least 10 space steps to be resolved.

In the case of the use of digital filters, a third factor needs to be added. It is the *thickness of the thin panel* (L_d) that the digital filter is representing. The digital filter represents the panel as an internal boundary to be placed in between of two adjacent TLM nodes; therefore, Δl should be chosen such that it keeps the panel thickness to be regarded as a "zero-thickness" boundary between nodes and does not introduce a greater separation between the adjacent nodes as illustrated in Figure 4.5. Further explanation will be given in §5.2.2 and §6.2.1.2.1.
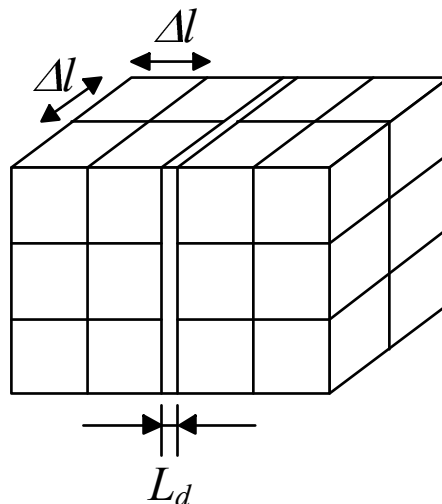
Figure 4.5. The thickness of the panel (under TLM modelling represented by a digital filter) needs to be at most one-fifth of the space step.

4.10 Summary

This chapter has briefly introduced the Transmission-Line Modelling (TLM) method. This is the method that was adopted in this study for modelling the panels. Its attractive features were presented to show that it supports certain cases better than the other candidate methods. Some treatments have been devised in coping with some of its drawbacks. One solution is the use of digital filters to reduce the computational burden, which will be investigated in Chapter 5. A brief review of modelling simple boundaries was presented. Finally, some implementation issues were clarified.

References

[4.1] Wikipedia: the free encyclopaedia. Accessed via the following link in 16th, Aug 2007 http://en.wikipedia.org/wiki/Model.

[4.2] C. Christopoulos, *Principles and Techniques of Electromagnetic Compatibility*. CRC Press, Boca Raton., 2nd ed. 2007.

[4.3] M. Robinson, T. Benson, C. Christopoulos, J. Dawson, M. Ganley, A.C. Marvin, S. Porter, and D. Thomas, *Analytical Formulation for the Shielding Effectiveness of Enclosures with Apertures*. IEEE transactions on electromagnetic compatibility, Vol.40, No.3 Aug 1998, pp. 240-248.

[4.4] J.L. Herring, *Developments in the Transmission-Line Modelling Method for Electromagnetic Compatibility Studies*. PhD Thesis, University of Nottingham, May 1993.

[4.5] J. Johns, J. Wlodarcyzk and A. Mallik, *New TLM Models for Thin Structures*. International Conference on Computation in

Electromagnetics, 25-27 Nov 1991, IEE, London. Conference Publication No. 350.

[4.6] J.A. Cole, J.F. Dawson and S.J. Porter, *Efficient Modelling of Thin Conducting Sheets within the TLM Method*. International Conference on Computation in Electromagnetics, 10-12 Apr 1996, IEE, London. Conference Publication No. 420.

[4.7] S. Maguer, A. Peden, D. Bourreau, and M. Ney, *Split-Step TLM (SS TLM): A New Scheme for Accelerating Electromagnetic-Field Simulation*. IEEE Transactions on Microwave Theory and Techniques, Vol.52, No.4, pp. 1182-1190, Apr 2004.

[4.8] C. Christopoulos, *The Transmission-Line Modeling Method TLM*. IEEE Press, N.Y., 1995.

[4.9] W.J.R. Hoefer, *The Transmission-Line Matrix method – Theory and Applications*. IEEE Transactions on Microwave Theory and Techniques, Vol. MTT-33, No. 10. pp.882-893, Oct. 1985.

[4.10] P.B. Johns, *The Art of Modelling*. Electronics and Power, pp. 565-569, Aug 1979.

[4.11] D.G. Swanson and W.J.R. Hoefer, *Microwave Circuit Modeling Using Electromagnetic Field Simulation*. Artech House, Boston, 2003.

[4.12] K. Chang (ed), *Encyclopedia of RF and Microwave Engineering*. John-Wiley & Sons, New Jersey, 2005.

5

Digital Filter Implementation

This chapter starts with a general introduction to digital filters. In this study digital filters are used for the purpose of representing thin layers in electromagnetic simulations. After introducing thin panels, the relevant digital filter structure is derived and illustrated with an example. Cascading of digital filters is discussed for the case of two different layers attached together. Then, the filter stability issue is studied for the digital filters used in this project. The chapter concludes with discussing how digital filter application can save modelling time.

5.1 Introduction

Generally, a filter is a network that selectively changes the wave shape, amplitude-frequency and/or phase-frequency characteristics of a signal in a desired manner. For a digital input data, a digital filter (DF) is used, which is a mathematical algorithm implemented in hardware and/or software that produces a digital output data for the purpose of achieving a filtering objective [5.1].

5.1.1 Filter Types

Digital filters can be divided into two classes, namely the infinite impulse response (IIR) and the finite impulse response (FIR). The IIR digital filter can be implemented with fewer coefficients than the corresponding FIR filter. This leads to a more economical filter in both computational and storage requirements than the FIR filter. It is shown [5.1] that for the same amplitude response specifications, the number of FIR filter-coefficients is typically six times the order of the IIR transfer

function. For example, a digital filter of type IIR that has two poles and two zeros will have a filter order of two. This IIR filter can represent the same amplitude response of an FIR filter that has twelve coefficients. It is important here to produce efficient filters in implementing physical systems. Moreover, the IIR filters are more efficient than FIR filters in terms of their computational effort. Accordingly, the digital filters developed in this project are all of IIR type. Unlike FIR filters, the stability of IIR filters can not always be guaranteed. This point is discussed in §5.6.

5.1.2 IIR Filter Realisation

Being a system that processes discrete-time input signal, the digital filter is best modelled using the z-transform. The z-transform of the filter unit impulse response, *h(n)*, is given as *H(z)* as

$$H(z) = \sum_{n=-\infty}^{\infty} h(n) z^{-n} \qquad (5.1)$$

where *H(z)* is the filter transfer function, with the complex variable *z* given by

$$z = e^{j\omega T} \qquad (5.2)$$

where ω is the radian frequency and *T* is a constant that represents time-delay by one sample.

A typical digital filter used in this project can be expressed by the Padé form given by

$$H(z) = \frac{b_{NZ} z^{-NZ} + \cdots + b_2 z^{-2} + b_1 z^{-1} + b_0}{a_{NP} z^{-NP} + \cdots + a_2 z^{-2} + a_1 z^{-1} + 1} \qquad (5.3)$$

The filter coefficients b_i, i=0..NZ and a_i, i=1..NP are real constants, with NZ and NP representing the number of zeros and the number of poles respectively. The filter order equals the number of poles, which are the roots of the denominator of equation (5.3).

The implementation of a digital filter requires three different types of functional elements: one-sample-time delay elements, multipliers by constants, and adders. The general structure of a digital filter that is given by equation (5.3) is shown in Figure 5.1.
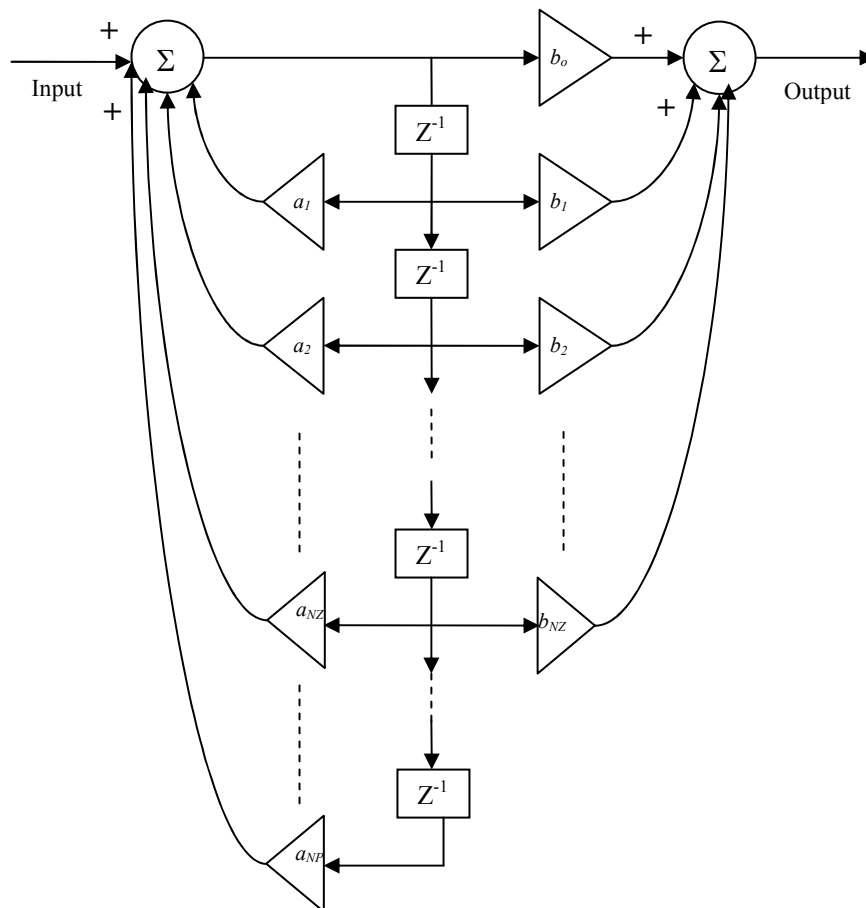
Figure 5.1. General realisation diagram of an IIR digital filter with NP poles and NZ zeros. Its coefficients are given in equation (5.3).

5.2 Thin Panels

A conductive panel with thickness much less than the skin depth is defined as a *thin* panel. The skin depth (δ) was introduced in §2.5 and its expression is restated in equation (5.4).

$$\delta = \sqrt{\frac{2}{\omega\mu\sigma}} \qquad (5.4)$$

where ω is the radian frequency, μ and σ are the permeability and conductivity of the panel material respectively.

Thin panels can be found when examining any structure that includes fine conductive elements or features that satisfy the definition of thin panels. Examples can include thin panels with or without perforation or fine conductive tracks [5.2].

5.2.1 Multiple Reflections

Thin panels require special treatment when they are modelled in terms of their electromagnetic properties. This is because of the multiple reflections that are encountered within the thin conductive panels as shown in Figure 5.2. These internal multiple reflections can often be neglected in the case of a thick conductive panel due to the high absorption loss [5.3]. The shielding effectiveness of a thin shield is normally dominated by reflection not absorption [5.4].

Thin Panel   Thick Panel
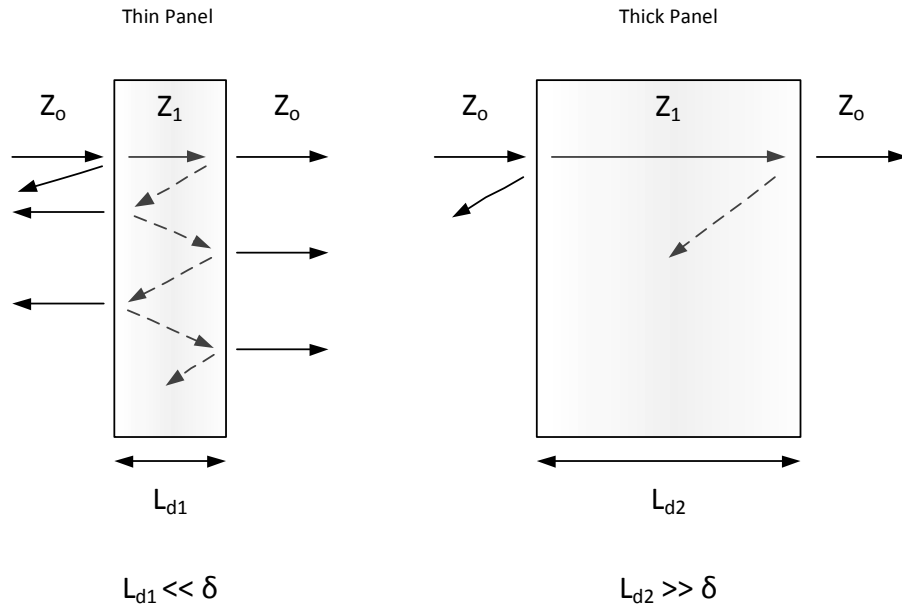
Figure 5.2. Multiple reflections occur in thin panels, whereas they are negligible in thick panels, where Z_o and Z_1 are the characteristic impedances of free space and the panel material respectively.

5.2.2 Modelling Difficulties

As shown in Chapter 4, modelling requires representing the object under modelling with TLM virtual cubes (TLM cells or nodes). Unlike thick panels, applying a regular mesh on a thin panel would produce an impractical computational burden in terms of memory storage and simulation time. This is because of the high density of TLM cells that would be required. As a guideline, there should be at least five TLM space segments (dl) representing the thickness of the panel. Furthermore, the higher the conductivity of the material is, the more TLM nodes are required to characterise the panel thickness. In terms of the excitation frequency, the minimum used wavelength should be represented by at least ten TLM space segments. Basically, the maximum size of the TLM space step (dl) is dictated by the minimum dimension in the setup (L_{min}) and by the minimum relevant wavelength size (λ_{min}). For completeness,

the constraint for the minimum *dl* will be stated in the case of using digital filters that represent embedded thin panels. The digital filter approach is applied by assuming that the digital filter plane (representing the panel) has an infinitesimal thickness. This means that the TLM space step should be significantly larger than the panel thickness (L_d) and hence the choice of *dl* to be at least five times the panel thickness. The complete constraint can be formulised as

$$5L_d \leq dl \leq Min\left[\frac{L_{min}}{5}, \frac{\lambda_{min}}{10}\right] \tag{5.5}$$

In the case of the conventional fine mesh, there is no minimum limit for *dl*; therefore, a thin panel will force *dl* and hence the time step ($dt = dl/2c$) to a very small value and hence requires very long computation times. Note that *c* is the speed of light in free space, which equals 2.99792458×10^8 m/s.

5.2.3 Multi-Scale Modelling

Basically, there are two main approaches to cope with systems that have embedded fine features [5.2]. The first approach is by introducing local mesh modification. This is done by having refined or distorted mesh. This modification increases the spatial resolution in the near proximity to the relevant fine features. However, this approach introduces an interface error between the fine and coarse mesh regions. This approach has been applied to diffusion problem [5.5 to 5.7] and to thermal problems [5.8]. The second approach is to introduce a local solution for the field components near the relevant fine features. The main challenge in this

approach is to find this local solution and to devise the corresponding interface. Relevant solutions were found for different materials with different properties like frequency-dependent properties, anisotropic properties, nonlinear properties, thin ferrite layers, and perforated walls [5.9 to 5.14].

In this project, a version of the second approach is adopted because it minimises errors that are produced when connecting the fine grid to the coarse grid. Moreover, this local solution is implemented by digital filters to characterise fine features like thin panels. Digital filters are represented as 'functional' boundaries, which means the simulation does not need to take the relevant panel into account explicitly as a physical body embedded within the system under modelling. It is thus not necessary to set the space step (dl) according to the thickness of the panel. In this way, it is possible to choose a larger value for dl. The resultant coarser mesh lowers significantly the computational effort required for simulation.

5.3 Filter Structure

A layer of material of thickness L_d located in free space can be modelled as shown in Figure 5.3. This model takes the net reflection (E_r) and transmission (E_t) through the layer. Thus, all the internal progressive reflections (E_{rm}) and transmissions (E_{tm}) are accounted for in the final system.
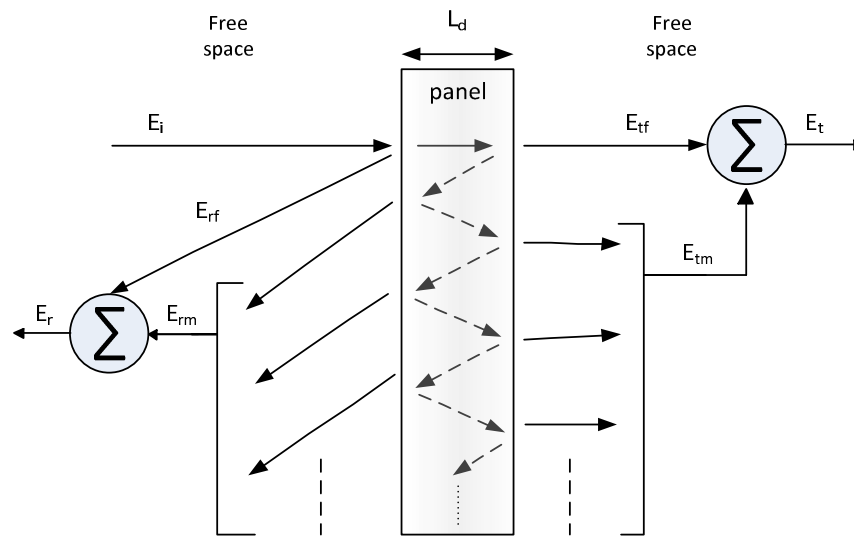
Figure 5.3. Modelling of a thin layer located in free space with incident field (E_i) from left. The final transmitted field (E_t) is the sum of the first transmitted field (E_{tf}) and the transmitted fields due to multiple reflections (E_{tm}). Similarly, $E_r = E_{rm} + E_{rf}$.

The coefficients of the reflection and transmission processes can be represented as digital filters since these processes 'reshape' their input waves. Having two ports, this means four digital filters are required to implement the model shown in Figure 5.3. The net reflected (E_r) and transmitted (E_t) fields are used in Figure 5.4 to show the complete model for the general case when the load is not matched to free space. The transmission coefficient (T) and reflection coefficient (Γ) triangular blocks can be realised using the general structure of a digital filter that is presented in Figure 5.1.
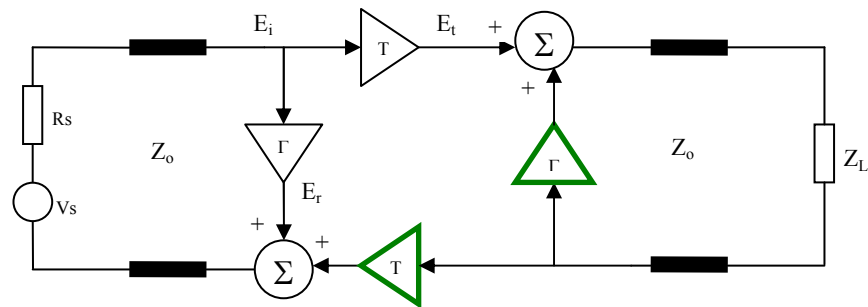
Figure 5.4. Material layer in free space is replaced with its corresponding four digital filters. The material is inserted between two transmission line sections representing free space. The green digital filters process the reflection from the load.

Generally, this model requires four distinct filters. However, if the panel material is isotropic then there will be one filter type to represent the transmission coefficient. This is because the incident wave will suffer the same attenuation from both sides of the panel. This is not the case with the anisotropic materials. The two reflection coefficient filters are also identical if the medium surrounding the material is the same on both sides.

The typical number of poles for digital filters used in this project ranged from three poles to nine poles. The choice of the number of poles depends on the complexity of the response of the filter as a function of frequency. As a rule of thumb, the more features (e.g., peaks and nulls) there are in the filter coefficient (reflection or transmission), the more poles are required to describe the response.

5.3.1 Filter Realisation

Assuming three poles and three zeros, the reflection coefficient (Γ) and the transmission coefficient (T) functions in the discrete z-domain will be given by equations (5.6) and (5.7) respectively.

$$\Gamma(z) = \frac{b_{r3}\,z^{-3} + b_{r2}\,z^{-2} + b_{r1}\,z^{-1} + b_{r0}}{a_{r3}\,z^{-3} + a_{r2}z^{-2} + a_{r1}\,z^{-1} + 1} \tag{5.6}$$

$$T(z) = \frac{b_{t3}\,z^{-3} + b_{t2}\,z^{-2} + b_{t1}\,z^{-1} + b_{t0}}{a_{t3}\,z^{-3} + a_{t2}z^{-2} + a_{t1}\,z^{-1} + 1} \tag{5.7}$$

where the real coefficients are scaled by a_{r0} and a_{t0} for $\Gamma(z)$ and $T(z)$ respectively.

These coefficients can be determined uniquely for given material properties, digital filter properties, and the angle of incidence (θ) measured from the line normal to the panel edge. Material properties consist of the material conductivity (σ), relative permittivity (ε_r), relative permeability (μ_r), and the material thickness (L_d). This study treats non-magnetic materials; therefore, one can always assume that $\mu_r = 1$. Digital filter properties include the number of poles (*NP*) and the number of zeros (*NZ*). If not otherwise stated, they will be taken to be equal throughout this project. This is because if the number of poles is greater than the number of zeros then the magnitude of the frequency response will tend to zero as the frequency becomes large. On the other hand, if the number of zeros is greater than the number of poles then the gain will increase without bound when the frequency increases. This case can not happen in passive systems because it implies a power gain through the

system [5.15]. For normal incidence the angle of incidence is zero. The overall reflection and transmission coefficients can be found as follows [5.16, 5.17].

$$\Gamma = \Gamma_F \frac{1 - e^{-j2\delta}}{1 - \Gamma_F^2 \, e^{-j2\delta}} \tag{5.8}$$

$$T = \frac{\left(1 - \Gamma_F^2\right) e^{-j\left(\delta - \frac{\omega L_d}{c}\right)}}{1 - \Gamma_F^2 \, e^{-j2\delta}} \tag{5.9}$$

where

$$\delta = \frac{\omega L_d}{c} \sqrt{\varepsilon_r - j \frac{\sigma}{\varepsilon_o \omega} - \sin^2 \theta} \tag{5.10}$$

Γ_F is the Fresnel reflection coefficient for the half-plane, which is given by equation (5.11) when the electric field is perpendicular to the plane of incidence as illustrated in Figure 5.5.a.

$$\Gamma_{F\perp} = \frac{\cos\theta - \sqrt{\varepsilon_r - j \frac{\sigma}{\varepsilon_o \omega} - \sin^2 \theta}}{\cos\theta + \sqrt{\varepsilon_r - j \frac{\sigma}{\varepsilon_o \omega} - \sin^2 \theta}} \tag{5.11}$$

Alternatively, when the electric field is parallel to the plane of incidence (Figure 5.5.b), Γ_F is given by

$$\Gamma_{F\parallel} = \frac{\left(\varepsilon_r - j \frac{\sigma}{\varepsilon_o \omega}\right)\cos\theta - \sqrt{\varepsilon_r - j \frac{\sigma}{\varepsilon_o \omega} - \sin^2 \theta}}{\left(\varepsilon_r - j \frac{\sigma}{\varepsilon_o \omega}\right)\cos\theta + \sqrt{\varepsilon_r - j \frac{\sigma}{\varepsilon_o \omega} - \sin^2 \theta}} \tag{5.12}$$

The angular frequency is $\omega = 2\pi f$. Speed of light in free space is c, which equals 2.99792458×10^8 m/s. Throughout this project, the excitation electric field is perpendicular to the incident plane. This makes parameter Γ_F be defined by equation (5.11), supported by Figure 5.5.a.
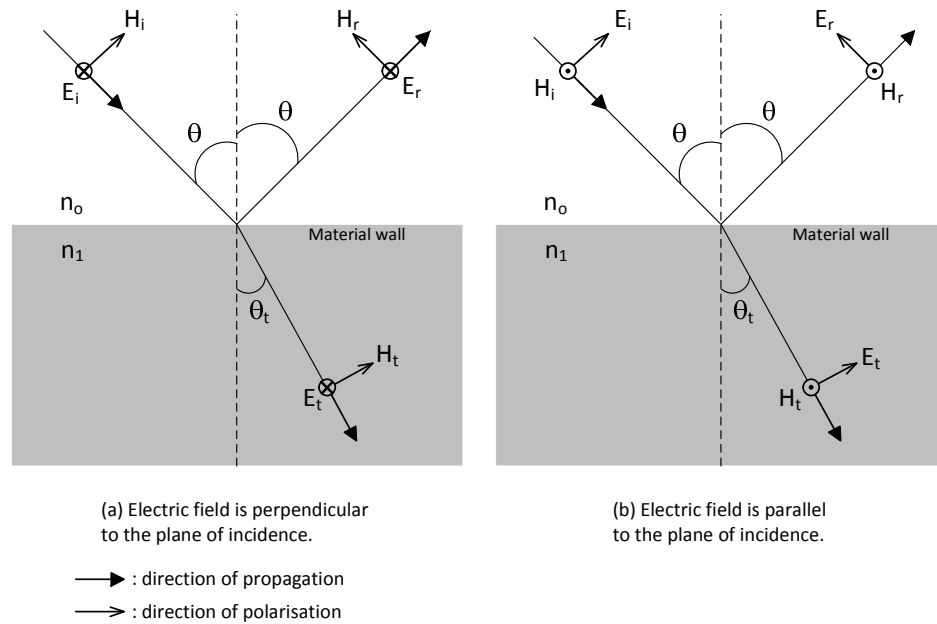
Figure 5.5. Reflection and transmission of a plane wave at a plane dielectric boundary with two cases of the relationship between the electric field and the plane of incidence [5.18].

However, the other polarisation (illustrated in Figure 5.5.b) has been tested and the method has proved to produce an agreement between fine mesh and coarse mesh/digital filter configurations.

By applying equations (5.8 to 5.12), the complex data of reflection and transmission coefficients will be defined over the relevant frequency points stored as the discrete-frequency values in vector ω. Complex vector fitting can now be applied to $\Gamma(\omega)$ and $T(\omega)$ to generate the a_i and b_i coefficients of the Padé form that is given by equations (5.6) and (5.7). This fitting process can be performed using the Matlab function `invfreqs` twice: one for the reflection coefficient and one for the transmission coefficient. The use of `invfreqs` is discussed in the next section.

5.3.2 The Matlab function `invfreqs`

The Matlab function `invfreqs,` defined by the Matlab file `invfreqs.m,` provides complex-data fitting in a form of rational polynomials using least-squares fitting [5.19, 5.20]. The application of `invfreqs` will result the set of real coefficients (A_i and B_i) defined in the s-domain as

$$H(s) = \frac{B_{NZ}\, s^{NZ} + \cdots + B_2\, s^2 + B_1\, s + B_0}{s^{NP} + \cdots + A_2 s^2 + A_1\, s + A_o} \qquad (5.13)$$

where s is the frequency-domain complex variable. These coefficients are used by the electromagnetic solver regSolve. The solver applies the bilinear transformation to derive the corresponding digital filter defined in the z-domain [5.21]. Equation (5.3) can be obtained from equation (5.13) by applying the bilinear z-transform as illustrated in

$$H(z) = Z\{H(s)\} \qquad (5.14)$$

where the bilinear z-transform is performed by substituting s variable in equation (5.13) as

$$s \rightarrow \frac{2}{\Delta t}\left(\frac{1 - z^{-1}}{1 + z^{-1}}\right)$$

where Δt is the simulation time step, which will be explained (as dt) in §5.5.1.1. An overview of the process is illustrated in Figure 5.6.

79
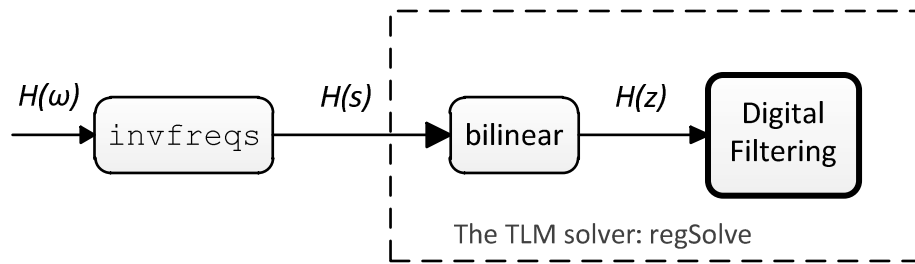
Figure 5.6. Pictorial summary of how `invfreqs` function prepares the frequency data for the TLM solver.

5.3.2.1 Basic Use

The basic application of `invfreqs` is illustrated in Figure 5.7.
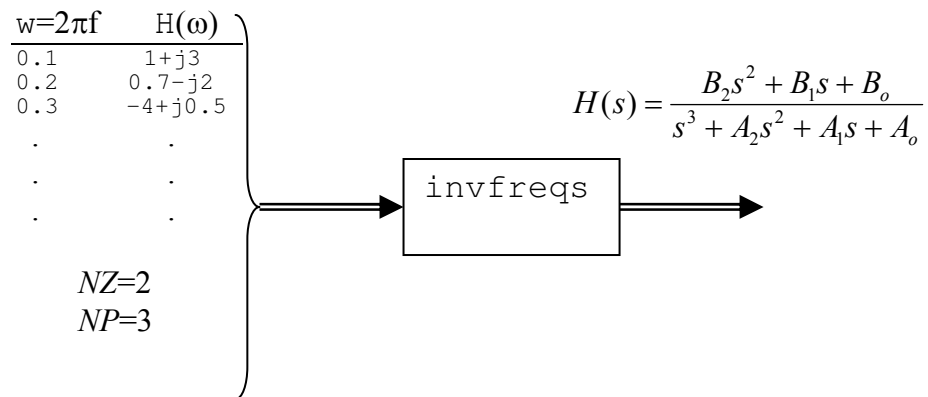
Figure 5.7. Complex vector fitting by `invfreqs` Matlab function. The letter `w` stands for the angular frequency.

The following format calls the function `invfreqs` after defining the four quantities in the right-hand side parentheses. Notice that the letter 'w' is used to denote the radian frequency, ω. The function returns the two vectors in the left-hand side brackets.

$$[B,A]=\texttt{invfreqs}(H,w,NZ,NP);$$

where the input parameters are defined as:

H: $N_s \times 1$ vector where its elements are generally complex,

w: $N_s \times 1$ vector where its elements (real values) represent the frequency

points at which the corresponding elements of vector H are specified,

NZ: the number of zeros that represents the order of the numerator

polynomial in equation (5.13),

NP: the number of poles that represents the order of the denominator

polynomial in equation (5.13),

N_s: the number of samples used for this complex fitting.

The output parameters are defined as:

A: $(NP+1) \times 1$ vector where its elements are the real coefficients of the

denominator polynomial in equation (5.13),

B: $(NZ+1) \times 1$ vector where its elements are the real coefficients of the

numerator polynomial in equation (5.13).

5.3.2.2 `invfreqs` Example

It is required to find a mathematical Padé expression for the following

complex function specified on the stated frequency points as shown in

Table 5.1

Point number	w values (x 10^{10})	H(w)
1	0.0000	-0.9947 - 0.0000j
2	0.0287	-0.9947 - 0.0006j
3	0.0575	-0.9947 - 0.0013j
4	0.0862	-0.9946 - 0.0019j
5	0.1150	-0.9945 - 0.0025j
6	0.1437	-0.9943 - 0.0031j
7	0.1725	-0.9942 - 0.0037j
8	0.2012	-0.9940 - 0.0043j
9	0.2299	-0.9938 - 0.0048j
10	0.2587	-0.9936 - 0.0054j
11	0.2874	-0.9933 - 0.0059j
12	0.3162	-0.9931 - 0.0064j
13	0.3449	-0.9928 - 0.0069j
14	0.3737	-0.9925 - 0.0073j

15	0.4024	-0.9923 - 0.0077j
16	0.4311	-0.9920 - 0.0082j
17	0.4599	-0.9917 - 0.0085j

Table 5.1. The complex data that should be fitted to a padé expression using invfreqs Matlab function.

H(w) given in Table 5.1 could be the reflection coefficient or the transmission coefficient derived by equations (5.8) and (5.9) respectively.

Here the number of samples is N_s=17

Let us find the rational expression of a general example in which the numerator polynomial order (*NZ*) will be set to a different value from the denominator polynomial order (*NP*). In this case, let *NZ* be equal to 2 and *NP* be equal to 3.

The execution of the following statement will produce the required s-domain coefficients.

```
[B,A]=invfreqs(H,w,2,3);
```

The length of vectors B and A will be *NZ*+1=3 and *NP*+1=4 respectively. These vectors contain the required mathematical expression, which will be given as

B=[-2.9721e+12   -1.4171e+23   -9.3041e+32] and

A=[1   3.1322e+12   1.4455e+23   9.3535e+32]

This is equivalent to the following mathematical expression that represents the s-domain transfer function.

$$H(s) = \frac{-2.9721 \times 10^{12} \ s^2 - 1.4171 \times 10^{23} \ s - 9.3041 \times 10^{32}}{s^3 + 3.1322 \times 10^{12} \ s^2 + 1.4455 \times 10^{23} \ s + 9.3535 \times 10^{32}}$$

This example is concerned only with the use of `invfreqs` function. Issues of selecting the design parameters are presented in §5.5 when a digital filter design is exemplified in detail.

5.4 Filter Cascading

It is required to investigate the possibility of developing a method through which one can derive the overall system performance of a sandwich of layers in terms of its reflection and transmission parameters. This is to be done without building a filter (from first principles) for the entire sandwich that represents the relevant system. In this way, the system characteristics can be derived from the characteristics of each individual layer in the sandwich. This can simplify the system simulation. Moreover, using digital filters reduces the memory usage and simulation time. This is because each individual digital filter can represent a certain feature in the system. This feature may appear more than once in the system under modelling. Thus, one can have ready simple (i.e., low order) digital filters which can be used as part of the main system modelling whenever its relevant feature is part of the system. The overall system characteristics can be obtained by cascading the relevant simple digital filters in the right sequence.

The question now is: Given the reflection and transmission coefficients of the individual digital filters, as shown in Figure 5.8, how can we relate them to the relevant coefficients for the overall cascade?
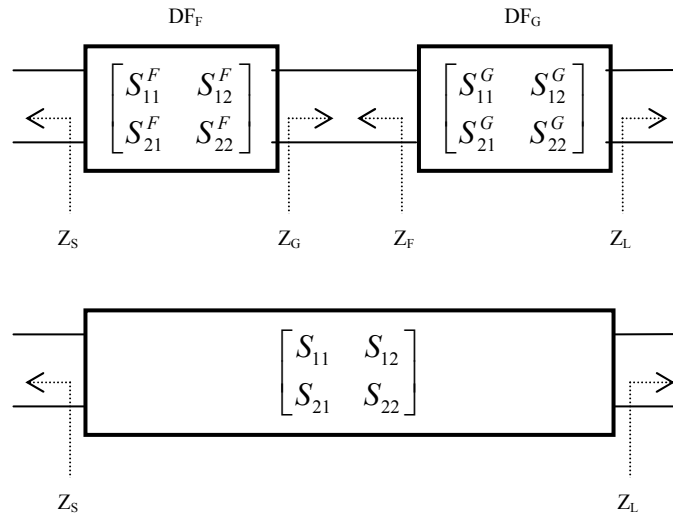
Figure 5.8. Cascading digital filters F and G.

Assuming a system that characterizes a reciprocal medium, the S matrix is symmetric[*]. The system source impedance is referred to as Z_S while Z_L is the system load impedance. Z_F is the source impedance for digital filter G, which is the output impedance for digital filter F. In the same logic Z_G is the load impedance for digital filter F, which is the input impedance for digital filter G. The letters 'F' and 'G' have been chosen to name the two filters in order to remove any confusion that might happen with using the ABCD parameters.

Unlike the ABCD matrix, S matrix can not be used to derive cascaded filters by simply multiplying the individual S matrices of the cascaded stages. Some intermediate transformation need to be applied first. Frickey [5.22] has presented a transformation between S parameters and the ABCD parameters. This transformation was used to relate the S parameters of two individual filters with the overall filter of their cascade.

---

[*] This is not the case with the anisotropic material (see §3.7) in which a change of polarisation may occur upon propagating through the material.

5.4.1 The Cascade S-parameters

In this section, a cascade of two systems will be considered. Both systems are two-port networks that can represent digital filters in this study. The aim here is to derive a relationship between the overall cascade S parameters and the S parameters of each individual filter.

The approach that will be followed is by making use of Frickey's transformation as shown in Figure 5.9.

$$S_F = \begin{bmatrix} S_{11}^F & S_{12}^F \\ S_{21}^F & S_{22}^F \end{bmatrix} \xrightarrow{\text{Frickey}} T_F = \begin{bmatrix} A_F & B_F \\ C_F & D_F \end{bmatrix}$$

$$S_G = \begin{bmatrix} S_{11}^G & S_{12}^G \\ S_{21}^G & S_{22}^G \end{bmatrix} \xrightarrow{\text{Frickey}} T_G = \begin{bmatrix} A_G & B_G \\ C_G & D_G \end{bmatrix}$$

$$S = \begin{bmatrix} S_{11} & S_{12} \\ S_{21} & S_{22} \end{bmatrix} \xleftarrow{\text{Frickey}} T = \begin{bmatrix} A & B \\ C & D \end{bmatrix} \xleftarrow{T=T_F.T_G}$$
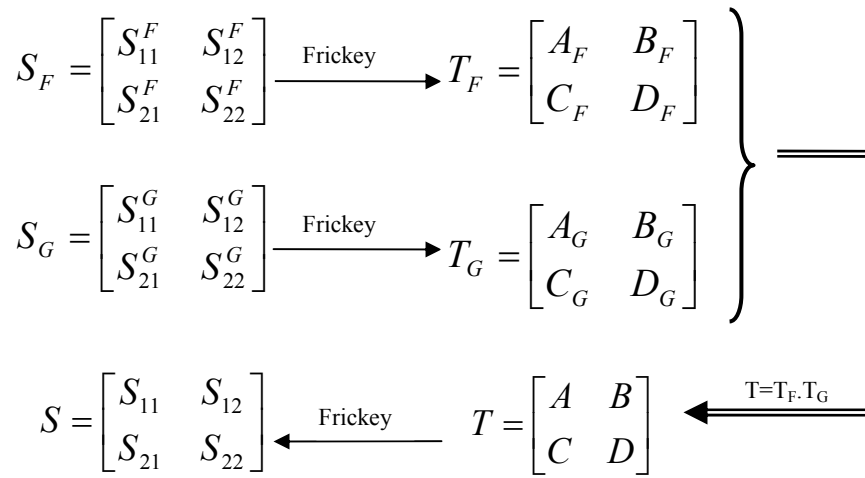
Figure 5.9. The summary of deriving the cascade S parameters from the individual filter S parameters.

To derive the ABCD parameters from the S parameters of the relevant system, the following formulae can be applied [5.22].

$$A = \frac{\left(Z_S^* + S_{11}Z_S\right)\left(1 - S_{22}\right) + S_{12}S_{21}Z_S}{2S_{21}\sqrt{R_S R_L}} \qquad (5.15)$$

$$B = \frac{\left(Z_S^* + S_{11}Z_S\right)\left(Z_L^* + S_{22}Z_L\right) - S_{12}S_{21}Z_S Z_L}{2S_{21}\sqrt{R_S R_L}} \qquad (5.16)$$

$$C = \frac{\left(1 - S_{11}\right)\left(1 - S_{22}\right) - S_{12}S_{21}}{2S_{21}\sqrt{R_S R_L}} \qquad (5.17)$$

$$D = \frac{(1 - S_{11})(Z_L^* + S_{22}Z_L) + S_{12}S_{21}Z_L}{2S_{21}\sqrt{R_S R_L}} \qquad (5.18)$$

where R_S and R_L are the real part of the complex impedance Z_S and Z_L respectively. The asterisk symbol in Z^* means a complex conjugate. By applying equations (5.15 to 5.18) on filter F and filter G, eight quantities will be generated, which are given by the matrices T_F and T_G as shown in Figure 5.9. Now, being expressed as a T matrix, the cascade T matrix can be obtained by direct matrix multiplication as

$$T = \begin{bmatrix} A & B \\ C & D \end{bmatrix} = \begin{bmatrix} A_F & B_F \\ C_F & D_F \end{bmatrix} \cdot \begin{bmatrix} A_G & B_G \\ C_G & D_G \end{bmatrix} \qquad (5.19)$$

Matrix multiplication gives

$$T = \begin{bmatrix} A & B \\ C & D \end{bmatrix} = \begin{bmatrix} A_F A_G + B_F C_G & A_F B_G + B_F D_G \\ C_F A_G + D_F C_G & C_F B_G + D_F D_G \end{bmatrix} \qquad (5.20)$$

where the ABCD parameters for filter F and filter G are defined according to equations (5.15 to 5.18).

To transform the ABCD parameters to the S parameters, the following formulae can be applied [5.22].

$$S_{11} = \frac{AZ_L + B - CZ_S^* Z_L - DZ_S^*}{AZ_L + B + CZ_S Z_L + DZ_S} \qquad (5.21)$$

$$S_{12} = \frac{2(AD - BC)\sqrt{R_S R_L}}{AZ_L + B + CZ_S Z_L + DZ_S} \qquad (5.22)$$

$$S_{21} = \frac{2\sqrt{R_S R_L}}{AZ_L + B + CZ_S Z_L + DZ_S} \qquad (5.23)$$

$$S_{22} = \frac{-AZ_L^* + B - CZ_S Z_L^* + DZ_S}{AZ_L + B + CZ_S Z_L + DZ_S} \qquad (5.24)$$

After some manipulation and simplification, the following results can be obtained.

$$S_{11} = \frac{\left(S_{12}^{F}S_{21}^{F} - S_{11}^{F}S_{22}^{F}\right)\left[S_{11}^{G}(Z_{F}+Z_{G}) + \left(Z_{F}^{*}-Z_{G}\right)\right] + S_{11}^{F}\left[S_{11}^{G}\left(Z_{F}-Z_{G}^{*}\right) + \left(Z_{F}^{*}+Z_{G}^{*}\right)\right]}{\left(Z_{F}^{*}+Z_{G}^{*}\right) - S_{11}^{G}S_{22}^{F}(Z_{F}+Z_{G}) + S_{11}^{G}\left(Z_{F}-Z_{G}^{*}\right) - S_{22}^{F}\left(Z_{F}^{*}-Z_{G}\right)} \quad (5.25)$$

$$S_{21} = \frac{2\sqrt{R_{F}R_{G}}\, S_{21}^{F}S_{21}^{G}}{\left(Z_{F}^{*}+Z_{G}^{*}\right) - S_{11}^{G}S_{22}^{F}(Z_{F}+Z_{G}) + S_{11}^{G}\left(Z_{F}-Z_{G}^{*}\right) - S_{22}^{F}\left(Z_{F}^{*}-Z_{G}\right)} \quad (5.26)$$

$$S_{22} = \frac{\left(S_{12}^{G}S_{21}^{G} - S_{11}^{G}S_{22}^{G}\right)\left[S_{22}^{F}(Z_{F}+Z_{G}) + \left(Z_{G}^{*}-Z_{F}\right)\right] + S_{22}^{G}\left[S_{22}^{F}\left(Z_{G}-Z_{F}^{*}\right) + \left(Z_{F}^{*}+Z_{G}^{*}\right)\right]}{\left(Z_{F}^{*}+Z_{G}^{*}\right) - S_{11}^{G}S_{22}^{F}(Z_{F}+Z_{G}) + S_{11}^{G}\left(Z_{F}-Z_{G}^{*}\right) - S_{22}^{F}\left(Z_{F}^{*}-Z_{G}\right)} \quad (5.27)$$

Only one of the parameters S_{12} and S_{21} need to be used here since in this project reciprocal media are treated. This means that S matrix is symmetric, meaning S_{12} equals S_{21}.

When Z_F and Z_G are equal and are both real, equations (5.25 to 5.27) can be reduced to equations (5.28 to 5.30) respectively.

$$S_{11} = S_{11}^{F} + \frac{S_{11}^{G}S_{12}^{F}S_{21}^{F}}{1 - S_{11}^{G}S_{22}^{F}} \quad (5.28)$$

$$S_{21} = \frac{S_{21}^{F}S_{21}^{G}}{1 - S_{11}^{G}S_{22}^{F}} \quad (5.29)$$

$$S_{22} = S_{22}^{G} + \frac{S_{22}^{F}S_{12}^{G}S_{21}^{G}}{1 - S_{11}^{G}S_{22}^{F}} \quad (5.30)$$

5.5 Digital Filter Example

This example is intended to simulate a two-dimensional setup with the purpose of modelling a cascade of two materials using a fine mesh then

to find the equivalent coarse mesh/digital filter model. The two materials

properties are shown in Table 5.2.

Material	A	B	Units
Conductivity (σ)	500	1000	S/m
Relative permittivity (ε_r)	5	5	–
Material width (L_d)	1	1	mm

Table 5.2. Properties of materials A and B.

5.5.1 Fine mesh setup

Figure 5.10 shows the xy-plane view of the setups that will be used to

simulate the fine-mesh structure.
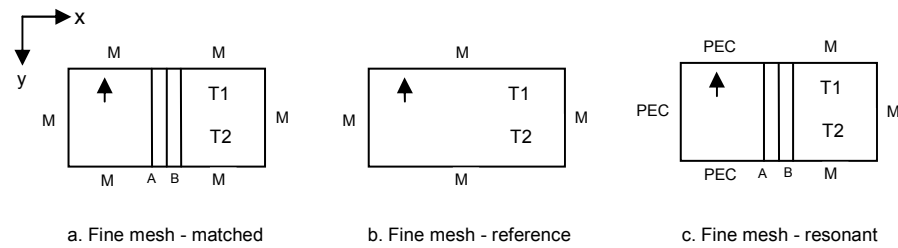
Figure 5.10. The xy-plane view of the two-dimensional setups used for fine-mesh simulation.

Boundary condition M stands for Matched or absorbing boundary. PEC

stands for Perfect Electric Conductor that has a reflection coefficient of

minus one to provide total reflection for electromagnetic waves.

Figure 5.11 shows the general template of the fine mesh setups. The

coordinates shown on the setup geometry represent the number of TLM

cells. This means that the distance between point (881,0,0) and point

(0,440,0) is 881dl in the x-direction and 440dl in y-direction. Thus, by

knowing that dl=0.1mm for the fine mesh, one can find that distance in

metres. Two cases are used for boundary conditions; each case is used for different setup:

1. All sidewalls (geometrically expressed as planes: x=0, x=881, y=0, and y=440) are set in a matched condition as shown in Figure 5.10.a.

2. Only the excitation part (i.e., the half of the cavity with the excitation source) is set to have a perfect electric conductor (PEC) side walls. The excitation part sidewalls are geometrically expressed as planes x=0, y=0: x<430, and y=440: x<430. The remaining side walls are set to have a matched condition as shown in Figure 5.10.c.
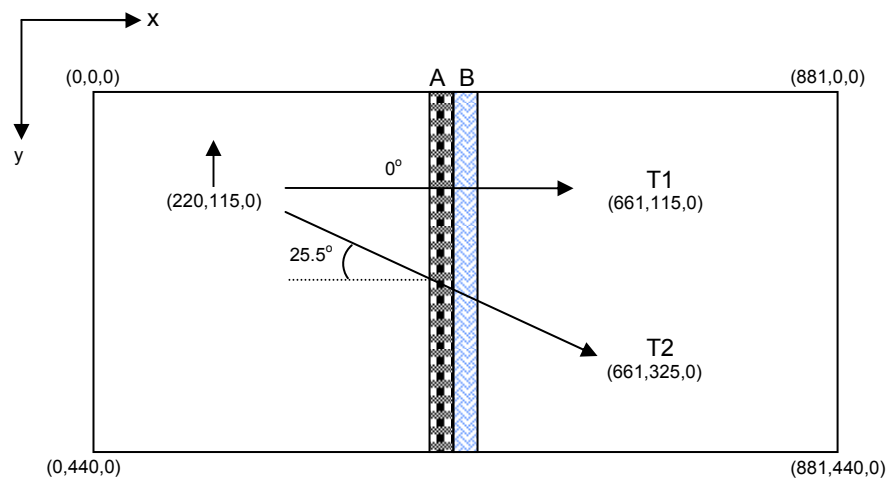
Figure 5.11. Geometry that is used with the fine mesh setups. The angle of incidence θ equals 0º and 25.5º for the path of the wave received by T1 and T2 respectively.

The reference setup is used to provide the corresponding results when no thin panel is used. As shown in Figure 5.10.b, the reference setup is exactly like the matched setup after removing the two materials. Two points have been chosen to receive the transmitted pulse. Point T1 receives the normal-incident field (i.e., $\theta = 0º$) while point T2 receives

89

the off-normal field at $\theta = 25.5°$. This assumption is valid provided that matched boundary condition is applied on all side-walls.

5.5.1.1 Design Parameters

In order to resolve the thin panel and obtain accurate responses, the space step (*dl*) should be set to be less than one-fifth of the panel thickness (L_d) according to §4.9 where it was stated that the lossier the material is, the more TLM cells are required to represent the panel thickness. Therefore, *dl* will be set to be as fine as one-tenth of the panel thickness (L_d). This criterion ensures high resolution in modelling the any object within the main space under modelling. Since L_d is equal to 1mm, *dl* can be set to 0.1mm.

The physical dimensions (in mm) are set to 88.2 x 44.1 x 0.1 so that it can be scaled by 21 *dl* to compare with the coarse mesh/digital filter version.

The number of time iterations (*NT*) is set to $2^{17} = 131072$ in order to obtain the steady state condition and resolve low frequencies. It was chosen in a form of the number two raised to a power of integer for compatibility with the Fast Fourier Transform (FFT).

The excitation is set as a Gaussian pulse to avoid the abrupt change of the rectangular pulse at the rising and falling edges. This arrangement is important to minimise Gibbs phenomenon that produces some extra high-frequency error in the frequency domain. The excitation pulse duration is set to 132ps. The excitation duration should be greater than 20 to 40 times the time step (*dt*), where $40dt = 40\ dl/2c = 20\text{x}10^{-4}/3\text{x}10^{8}$

= 6.7ps. This is because the Gaussian Pulse will then be well represented by these 20 to 40 samples. Moreover, the lower the excitation duration is, the higher the frequencies it can resolve. Furthermore, the maximum useful frequency should be taken into consideration such that the minimum useful wavelength should be resolved by 10 segments (*dl*) for a good representation of one cycle of a sine wave. Polarisation of the excited pulse is set in z-direction since z=0 and z=1 planes are set to be PEC. This arrangement has made the cavity capable of supporting TE wave.

5.5.2 Digital filter setup

This section will discuss the coarse mesh/digital filter (or simply the digital filter) setup for the same cases as in §5.5.1. By scaling down the fine mesh space step (*dl*) and dimensions by 21 a new setup is obtained. Table 5.3 shows the scaling effect on the setup mesh.

Design parameter	Fine mesh	Coarse mesh/digital filter	unit
X dimension	882	882 / 21 = 42	*dl*
Y dimension	441	441 / 21 = 21	*dl*
dl	0.1	0.1 x 21 = 2.1	mm

Table 5.3. Scaling by 21 for the fine mesh to obtain its coarse mesh version.

As with the fine mesh configurations, three setups are prepared for the digital filter simulations as shown in Figure 5.12.

a. Digital filter - matched   b. Digital filter - reference   c. Digital filter - resonant
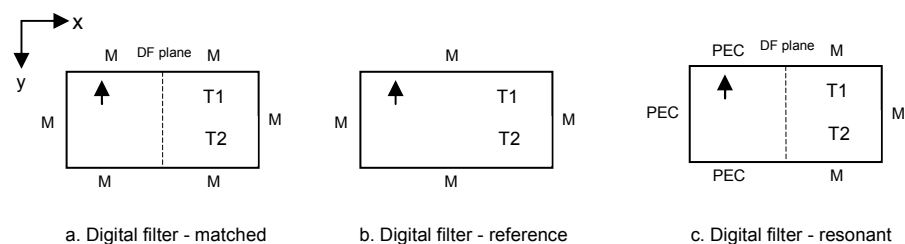
Figure 5.12. The two-dimensional setups used for the digital filter simulation.

The general template of the digital filter setups is shown in Figure 5.13.
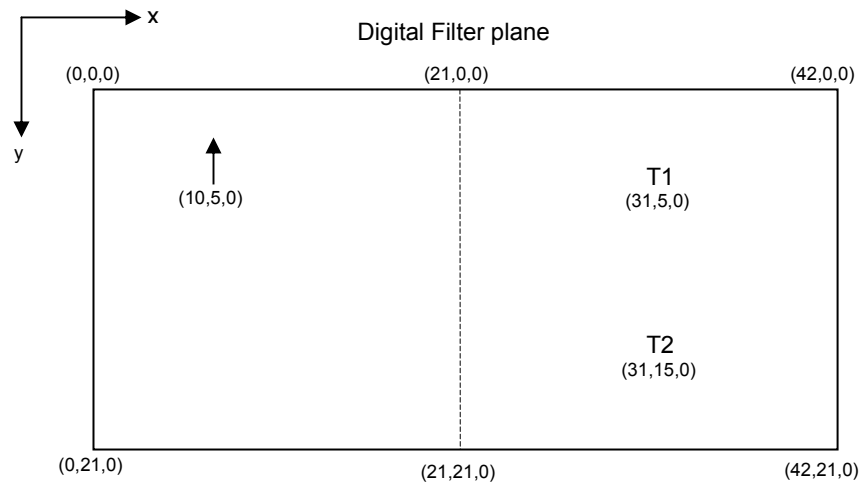
Figure 5.13. Geometry that is used with the digital filter setups.

5.5.2.1 Digital Filter Implementation

The frequency range and the number of poles need to be specified along with the properties of the two materials before setting the digital filter coefficients that are used in the regSolve code.

5.5.2.1.1 Frequency Range

A frequency range has to be determined at which the filter coefficients should be calculated. The frequency step decides the resolution of the frequency response. The number of frequency samples in the frequency vector should be chosen such that it does not over burden the simulation memory and at the same time, the frequency range can describe the frequency response with sufficient resolution that allows us to extract the required information within an acceptable accuracy.

Before determining the frequency resolution, the maximum frequency needs to be specified. The maximum usable frequency is determined

assuming that its corresponding wavelength (λ_{min}) should be represented by 10 TLM cells. Hence $f_{max} = c/\lambda_{min} = c/10dl = 3\times10^8/2.1\times10^{-2} =$ 14.3GHz. Thus f_{max} was chosen to be 15GHz.

5.5.2.1.2 Filter Design

The frequency vector has been determined to be up to 15GHz with a frequency step of 45.745MHz to get 328 frequency samples in the frequency vector. The transmission coefficient (T) and reflection coefficient (Γ) can be computed for materials A and B by applying equations (5.8 to 5.12) for each material. Figure 5.14 illustrates the reflection coefficient and transmission coefficient for material A. Similarly, Figure 5.15 shows the two coefficients for material B.
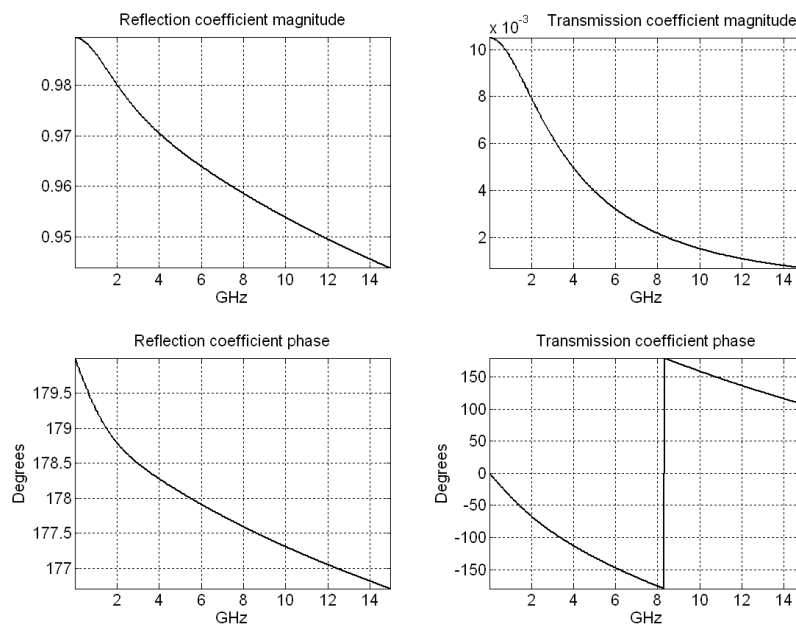
Figure 5.14. The computed reflection and transmission coefficients of material A over the defined frequency range.

93
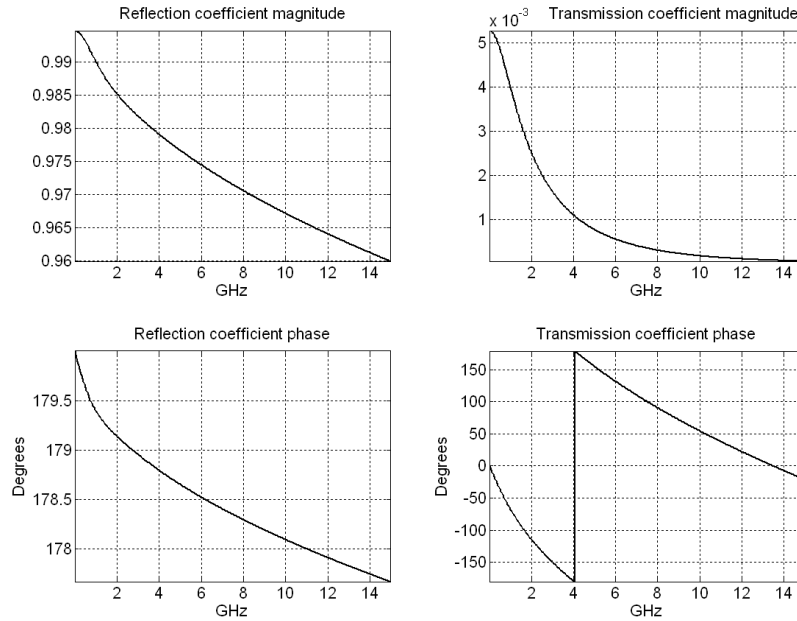
Figure 5.15. The computed reflection and transmission coefficients of material B over the defined frequency range.

5.5.2.1.3 Filter Cascading

Up to this point, four analytic complex vectors have been computed. These are the reflection coefficient and transmission coefficient for material A and material B. Next step is to apply the cascading formulae of equations (5.25 to 5.27) and setting their reference impedances (Z_A and Z_B) to equal real values, say 50 Ohms each.

Since each of the two materials is an isotropic material when considered alone, the following simplification can be made:

$\Gamma_A = S_{11A} = S_{22A}$

$T_A = S_{21A} = S_{12A}$

$\Gamma_B = S_{11B} = S_{22B}$

$T_B = S_{21B} = S_{12B}$

The S matrix of the resultant cascade is symmetric with the following parameters. The S_{11} is the analytic value of reflection coefficient from

94

material-A side. As it was verified, the transmission coefficient of the cascade is the same from either side of the cascade. Therefore, S_{12} has the same value of S_{21}. The S_{22} is the analytic value of reflection coefficient from material-B side. The analytic values of the reflection coefficients and the transmission coefficient are plotted in Figure 5.16.
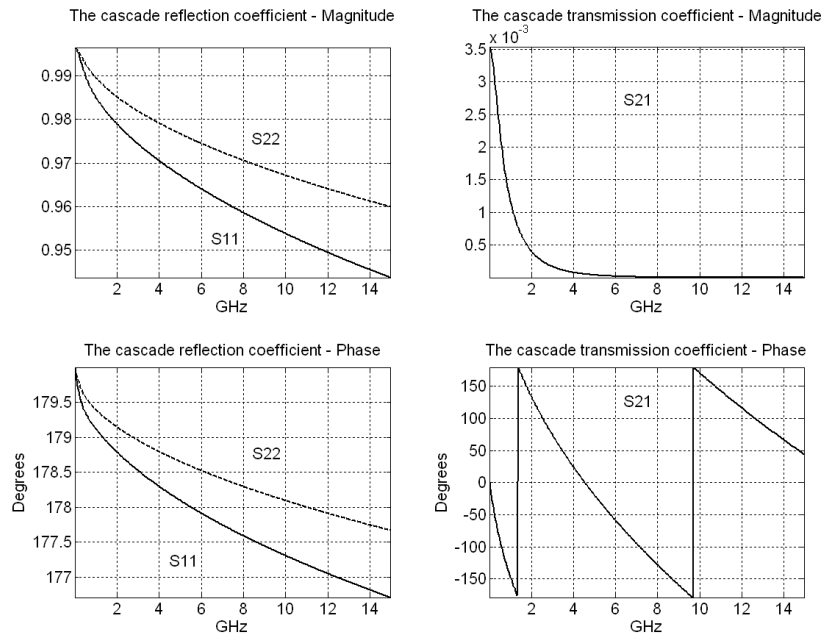
Figure 5.16. The reflection and transmission analytical coefficients from the two sides of the cascade of material A and material B.

5.5.2.1.4 Complex Fitting

Complex fitting should be applied to each of the three coefficients (S_{11}, S_{21}, and S_{22}) to generate the corresponding Padé form. In this study, the number of poles is taken to be equal to the number of zeros unless otherwise stated. The number of poles (*NP*) is chosen such that it is the minimum number that can provide an *acceptable* fit to the analytic curve that gives a stable response. The term "acceptable" here is based on a subjective judgement of the fitting results as will be clarified in Figure 5.17 and Figure 5.18. However, in case a subjective judgement is hard to

be made, an objective judgement based on the IEEE standard 1597.1 can be made [5.23]. This fitting process for each of the three coefficients can be performed using the Matlab function `invfreqs.m` which produces two sets of real constants, namely A_i and B_i as illustrated in Figure 5.7, where H(ω) can be S_{11}, S_{21}, or S_{22}.

Figure 5.17 shows the complex fitting of S_{11} and S_{22} to three-pole filters; and the complex fitting of S_{21} to a four-pole filter. It is clear that a four-pole fitting for S_{21} demonstrates a poor verification. To less extent, three-pole fitting for S_{11} and S_{22} also suffers from poor verification with the analytic curve at frequencies below 1GHz.
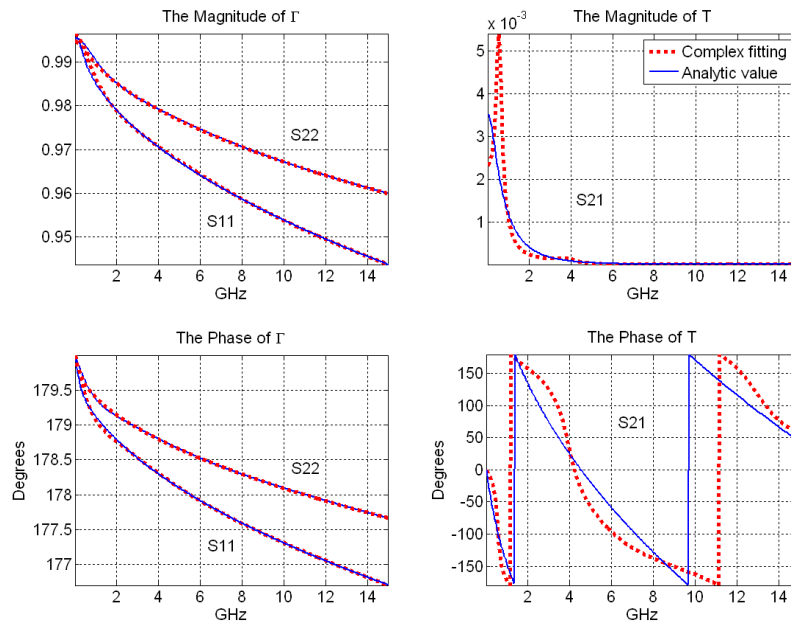
Figure 5.17. Complex fitting of the reflection coefficients (S_{11} and S_{22}) to three-pole filters while the transmission coefficient (S_{21}) is fit to four-pole filter. The fit curve is dotted while the analytic curve is solid.

By adding another pole for each coefficient an acceptable fit is achieved. Thus, the number of poles that was chosen for reflection coefficient and transmission coefficients is four and five poles respectively. Table 5.4 shows the Padé constants of S_{11}, S_{21}, and S_{22}. These coefficients

represent the digital filter that is a resultant of cascading the two

materials A and B.

	S_{11}	S_{21}	S_{22}
NP	4	5	4
b_o	-0.7183	-1.3163×10^{-6}	-0.7856
b_1	-6.4134×10^{11}	1.4598×10^{5}	-7.1169×10^{11}
b_2	-6.8321×10^{22}	-2.2604×10^{16}	-7.8328×10^{22}
b_3	-1.5472×10^{33}	1.4550×10^{27}	-1.8562×10^{33}
b_4	-5.5706×10^{42}	-7.6496×10^{37}	-7.4708×10^{42}
b_5		1.6481×10^{48}	
a_1	7.1179×10^{11}	5.7541×10^{10}	7.6729×10^{11}
a_2	7.1694×10^{22}	2.5259×10^{21}	8.1107×10^{22}
a_3	1.5803×10^{33}	3.6614×10^{31}	1.8852×10^{33}
a_4	5.5933×10^{42}	2.7752×10^{41}	7.5001×10^{42}
a_5		4.5456×10^{50}	

Table 5.4. The three coefficients of the digital filter given in terms of their real constants.

Figure 5.18 shows the fitting using these values of the number of poles

and compares with analytic results.
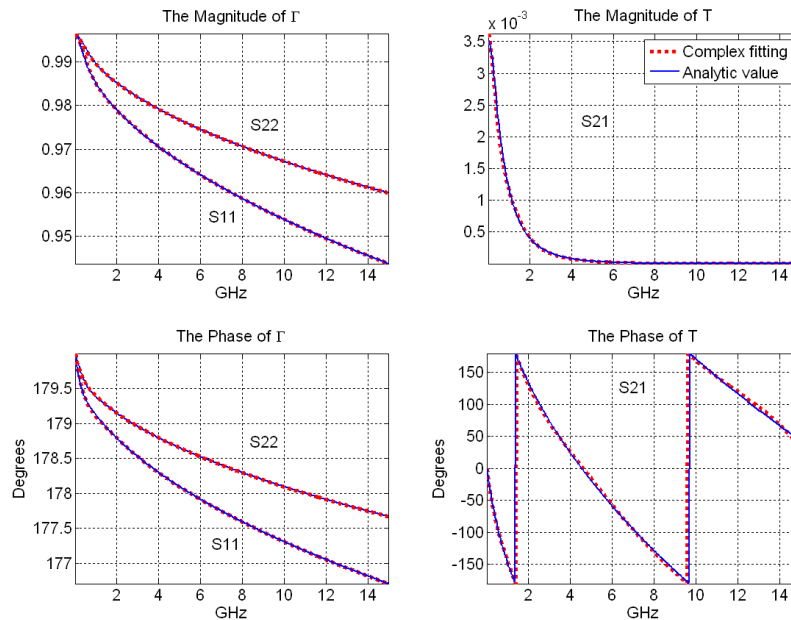
Figure 5.18. Complex fitting of the reflection coefficients (S_{11} and S_{22}) to four-pole filters while the transmission coefficient (S_{21}) is fit to five-pole filter. The fit curve is dotted while the analytic curve is solid.

The values of poles and zeros are stated in Table 5.5.

S_{11}		S_{21}		S_{22}	
Poles	Zeros	Poles	Zeros	Poles	Zeros
X 10^{11}	X 10^{11}	X 10^{10}	X 10^{10}	X 10^{11}	X 10^{11}
-5.9590	-7.7350	-1.9680 +3.5514j	1.0356 +9.6594j	-6.4627	-7.8234
-0.8675	-0.8975	-1.9680 -3.5514j	1.0356 -9.6594j	-0.9035	-0.9257
-0.2477	-0.2521	-0.8005 +0.7933j	2.8384 +5.6245j	-0.2566	-0.2599
-0.0437	-0.0443	-0.8005 -0.7933j	2.8384 -5.6245j	-0.0501	-0.0505
		-0.2171	3.3426		

Table 5.5. The complex values of poles and zeros of the cascaded digital filter.

5.5.3 Results

With the application of the six generated regSolve cases (demonstrated in Figures 5.10 and 5.12), a set of results were obtained. The shielding effectiveness (*SE*) is found for the developed setups in the frequency domain as

$$SE(f) = \frac{E(f)_{at\,T\_Reference}}{E(f)_{at\,T\_with\,object}} \qquad (5.31)$$

This applies on point T1 and T2. The "*Reference*" subscript refers to the case when there is no object (material or the corresponding digital filter) as illustrated in Figure 5.10(b) and 5.12(b). The "*with object*" subscript can be the matched case shown in Figures 5.10(a) and 5.12(a) or it can be the resonant case shown in Figures 5.10(c) and 5.12(c).

5.5.3.1 Fine mesh – Matched case

Shielding effectiveness at points T1 and T2 is shown in Figure 5.19.
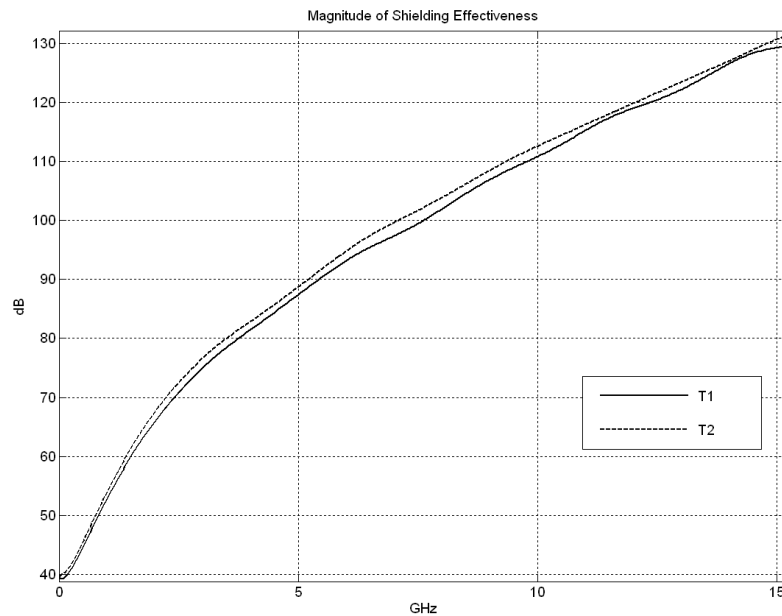
Figure 5.19. Shielding effectiveness for two different angles of incidence.

By comparing the SE curve at T1 with that at T2 one can observe that the magnitude of shielding effectiveness is almost the same in these two points.

The time-domain signal observed at T1 and T2 is shown in Figure 5.20 for the two cases: with and without the panel. It is obvious that the Gaussian pulse has experienced attenuation, delay, and dispersion due to the lossy material panel. The time delay the pulse has experienced when it penetrated the material panel will be called the *penetration time*. Further explanation will be given in §6.2.2.3. Penetration time can be defined for the radiation path at a given point as the time difference between the peaks of two pulses: the transmitted pulse through the material and the free space propagated pulse (without the material). Penetration time through the meshed cascade is found to be 479.4 ps and 501.0 ps for paths linking the source to T1 and T2 respectively.
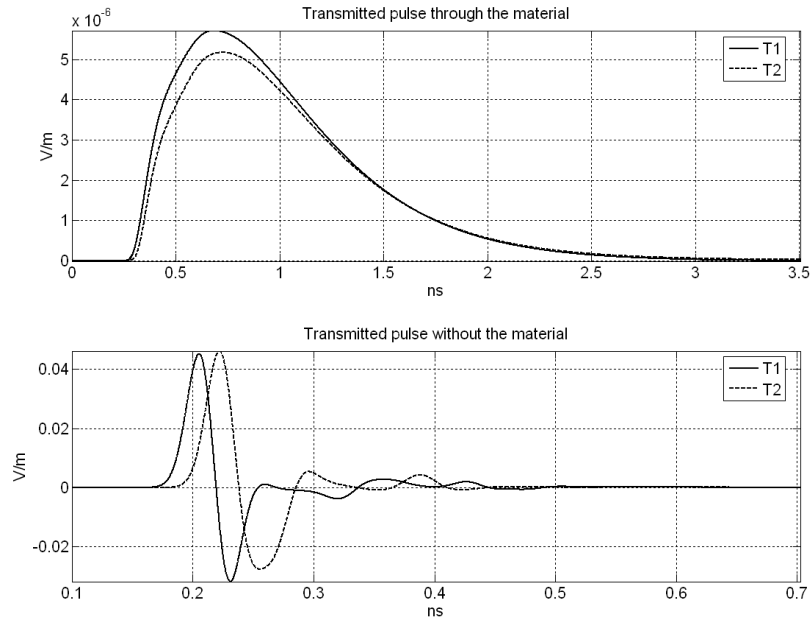
Figure 5.20. Fine-mesh excited pulse with and without the object for the two points.

5.5.3.2 Fine mesh – Resonant case

Shielding effectiveness for points T1 and T2 are shown in Figure 5.21.

The analytic values of the resonant frequencies are defined for a given

conducting rectangular cavity as

$$f_{mnp} = \frac{u}{2}\sqrt{\left(\frac{m}{a}\right)^2 + \left(\frac{n}{b}\right)^2 + \left(\frac{p}{d}\right)^2} \qquad (5.32)$$

where u is the speed of light in the medium that fills the cavity, a, b, and

d represent the x, y, and z-dimensions of the cavity, respectively. The

integers m, n, and p represent the number of half wavelengths in the x-,

y-, and z-dimensions respectively. Further clarification will be given in

§6.2.2.2.

The analytic values of resonant frequencies show a good agreement with

the simulated model. Due to non-matched conditions, the two points

receive the field transmitted pulse reflected from all directions. The

100

difference between the two points is more obvious for frequencies above

6GHz.
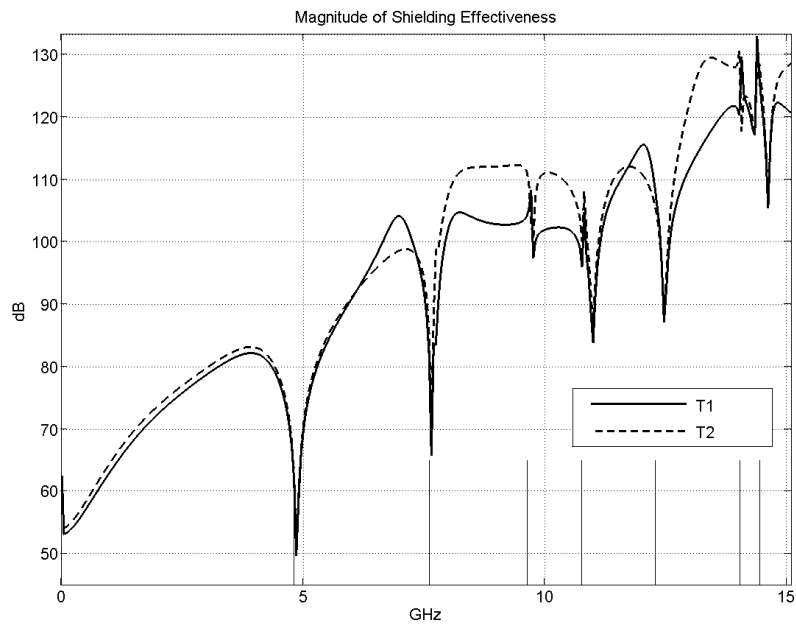
Figure 5.21. Shielding effectiveness for the resonant case.

5.5.3.3 Coarse mesh/digital filter – Matched case

The shielding effectiveness at points T1 and T2 are shown in Figure

5.22.
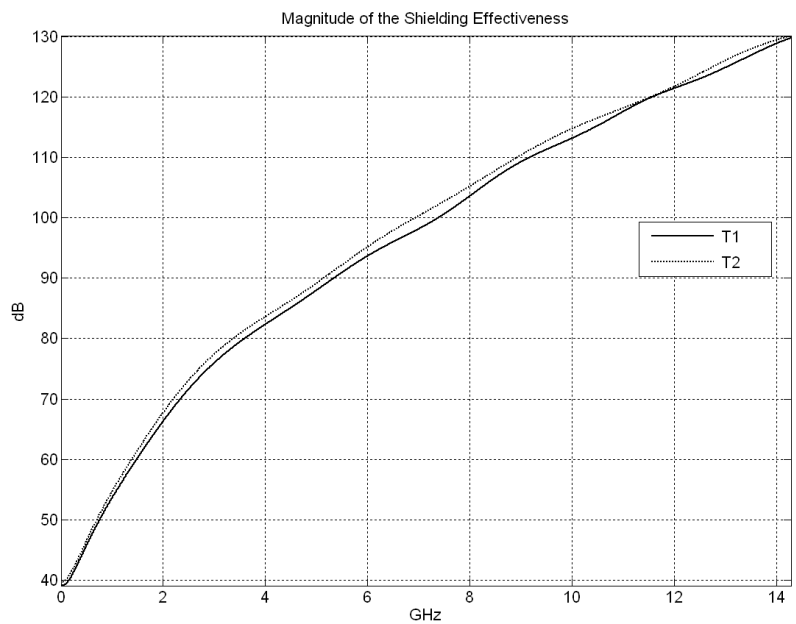
Figure 5.22. Shielding effectiveness for two different angles of incidence.

As with the case of fine mesh, the shielding effectiveness curves are smooth as expected with no features representing resonant frequencies. Again, like for the fine mesh case, there is a negligible effect of the angle of incidence on the shielding effectiveness response.

Time-domain signal at T1 and T2 are shown in Figure 5.23 with and without the object. Penetration time through the digital filter plane is found to be 472.9 ps and 493.8 ps for paths linking the source to T1 and T2 respectively.
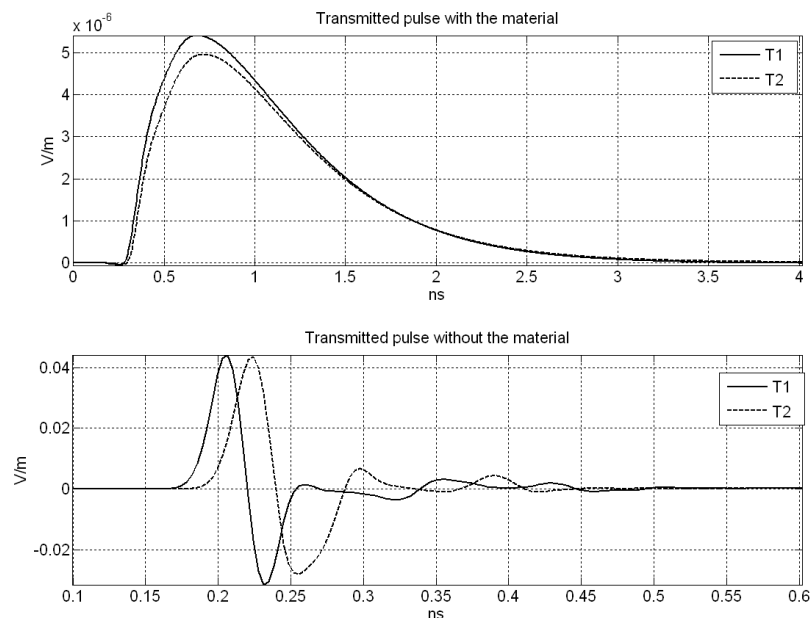
Figure 5.23. Coarse-mesh excited pulse with and without the object for the two points.

5.5.3.4 Coarse mesh/digital filter – Resonant case

The shielding effectiveness at points T1 and T2 are shown in Figure 5.24. The effect of the angle of incidence is noticeable for frequencies over 7.5GHz, which is an expected case with non-matched cavity walls. The resonant frequencies are calculated which agree with the shielding effectiveness response.
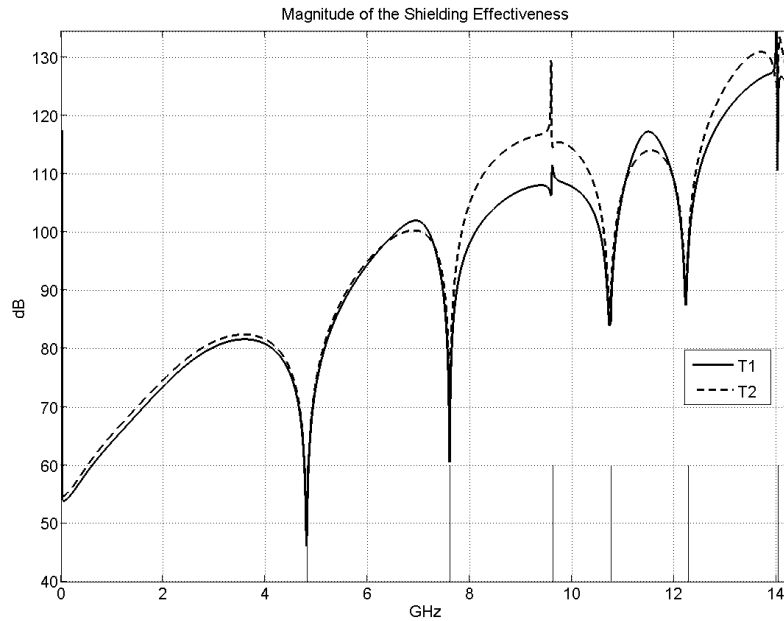
Figure 5.24. Shielding effectiveness for the resonant case. The vertical lines indicate the theoretical resonance frequencies.

5.5.3.5 Fine Mesh versus Coarse Mesh

Figures 5.25, 5.26, and 5.27 compare the fine mesh with the coarse mesh/digital filter results. From these figures, one can deduce that this method is applicable with incident angle other than the normal angle. The normal angle case is represented by the transmitted pulse received by T1. An off-normal incident wave by an angle of 25.5° with the normal line to the edge of the panel is received by T2.

In Figure 5.25, there is a noticeable time delay between the pulses received by T1 and T2 by 17.6ps without the presence of the material. This difference is expected due to the difference in the path length for the two pulses to propagate. Taking the fine mesh case, the coordinates of the excitation, T1, and T2 points are specified in Figure 5.11. The time required for the wave to reach T1 from the excitation is

$$t_{T1} = \frac{|\overrightarrow{ET1}|}{c} = \frac{(661-220)\,dl}{2.99792458 \times 10^8} = \frac{441 \times 0.1 \times 10^{-3}}{2.99792458 \times 10^8} = 147.1ps$$

103

Similarly, the time for the wave to reach T2 from the excitation is

$$t_{T2} = \frac{|\overrightarrow{ET2}|}{c} = \frac{\sqrt{(661-220)^2 + (325-115)^2}\ dl}{2.99792458 \times 10^8}$$

$$= \frac{488.45 \times 0.1 \times 10^{-3}}{2.99792458 \times 10^8} = 162.9\,ps$$

Thus the time difference is $162.9 - 147.1 = 15.8$ps, which is close to 17.6ps that is found from Figure 5.25.
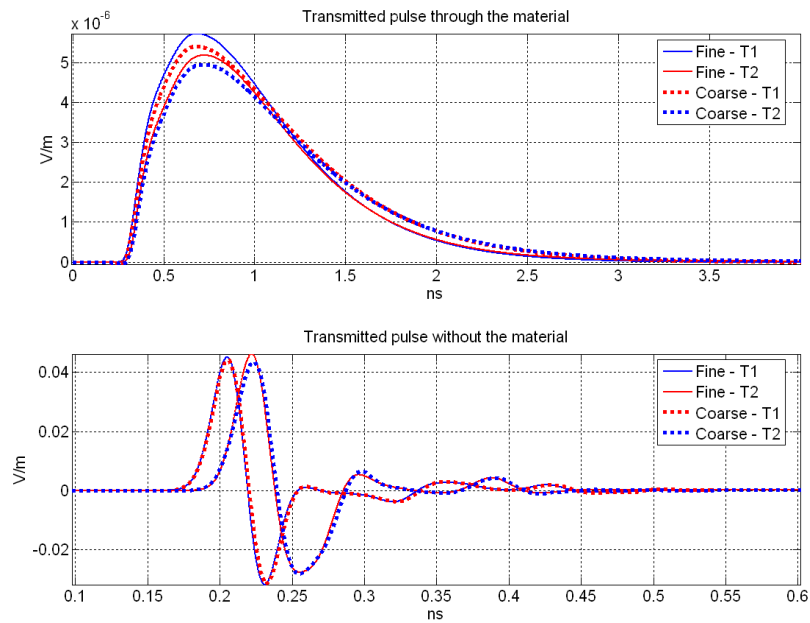
Figure 5.25. The transmitted pulse received by points T1 and T2 for the two cases of with and without the material.
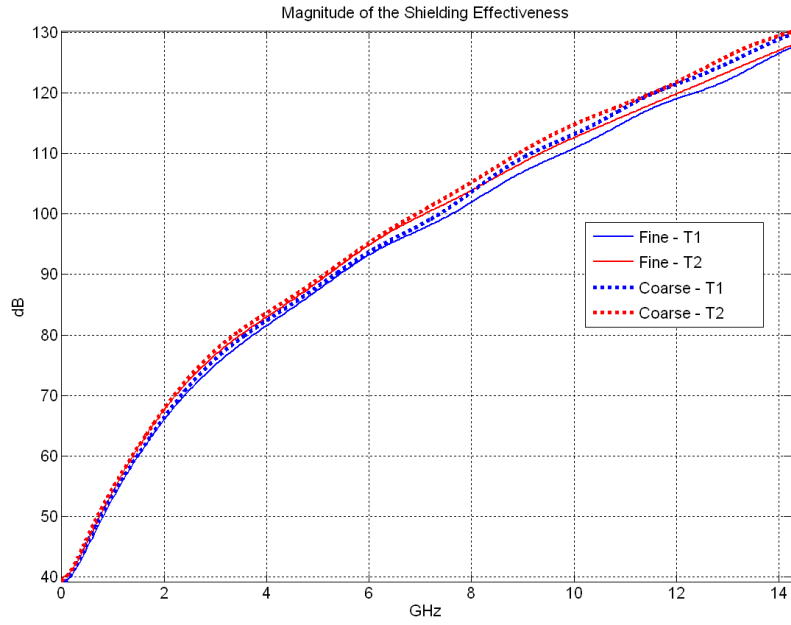
Figure 5.26. The matched case magnitude of shielding effectiveness for the two points T1 and T2 for the two cases of with and without the material.
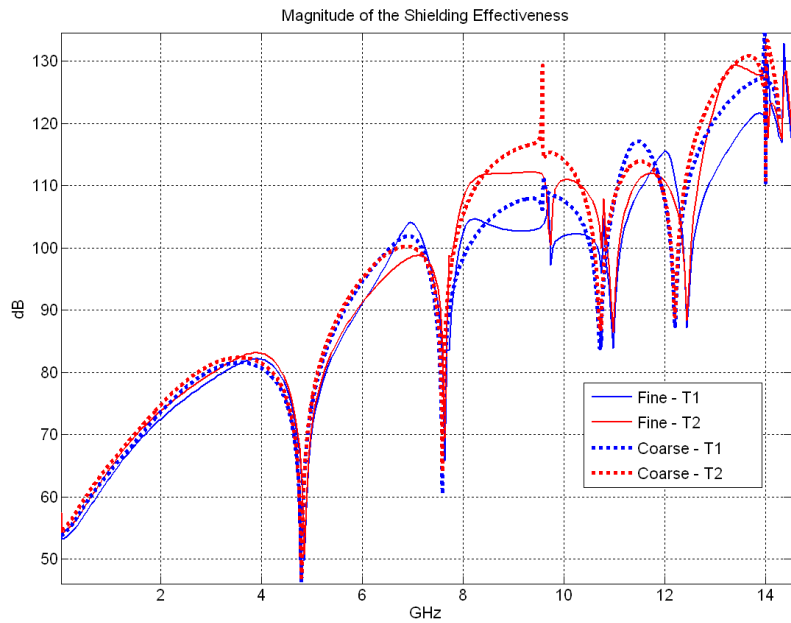
Figure 5.27. The resonant case magnitude of shielding effectiveness for the two points T1 and T2 for the two cases of with and without the material.

105

5.5.4 Test of Symmetry

The principle of reciprocity [5.24, 5.25] is the basis from which S_{21} can be found to be equal to S_{12}; however, S_{11} does not equal S_{22} in general. In this section, we check by numerical experimentation that reciprocity holds for the two materials used in the current example. This statement was verified by simulation for the cascade of three materials as well.

5.5.4.1 Symmetry with Digital Filter setup

Setup DL in Figure 5.28 represents a one-dimensional setup that has the same digital filter that is used in the two-dimensional setups explained in the previous sections. A new setup can be derived from the first one by swapping the excitation and receiving points around the digital filter plane. This is Setup DR in Figure 5.28.
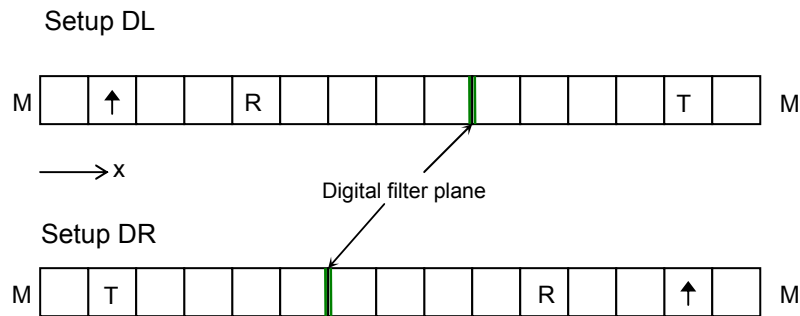
Figure 5.28. Two one-dimensional digital filter setups. The excitation source is to the left of the reader in Setup DL. The excitation source is to the right of the reader in Setup DR. The reference setups are not shown.

Simulation parameters are set as follows: The space step (*dl*) is 2mm. The number of time iterations is $2^{17} = 131072$, which makes a total

simulation time[*] of 0.437μs. The setup size is 15 x 1 x 1 measured in dl. The excitation is a Gaussian pulse with duration of 132ps. The boundary conditions are set to characterise a TEM transmission line, where the setup ends (planes x = 0 and x = 14) are set to the matched condition. The y-direction walls (planes y = 0 and y = 1) are set as perfect magnetic conductor (PMC). The z-direction walls (planes z = 0 and z = 1) are set as perfect electric conductor (PEC). The excitation is polarised in z-direction. It is expressed as a vertical arrow in Figure 5.28. Points R and T represent the field points that receive the reflected and transmitted pulse respectively.

Figure 5.29 shows the reflection coefficients and transmission coefficients when comparing setup DL with setup DR. It is clear that the transmission coefficients for the two setups are identical while there is a difference between the reflection coefficients. This agrees with the fact that the higher the conductivity is, the closer the reflection coefficient magnitude will be to one. Since material A has a lower conductivity (500 S/m) than material B (1k S/m), more energy penetrates A-material's side so less energy is reflected from this side. Therefore, the relevant reflection coefficient to B-material is closer to one.

---

[*] The name simulation time will be used to denote the transient time that is simulated, which is given by (time step) x (total number of time iterations). It will be further clarified in §5.7 and §6.2.1.2.
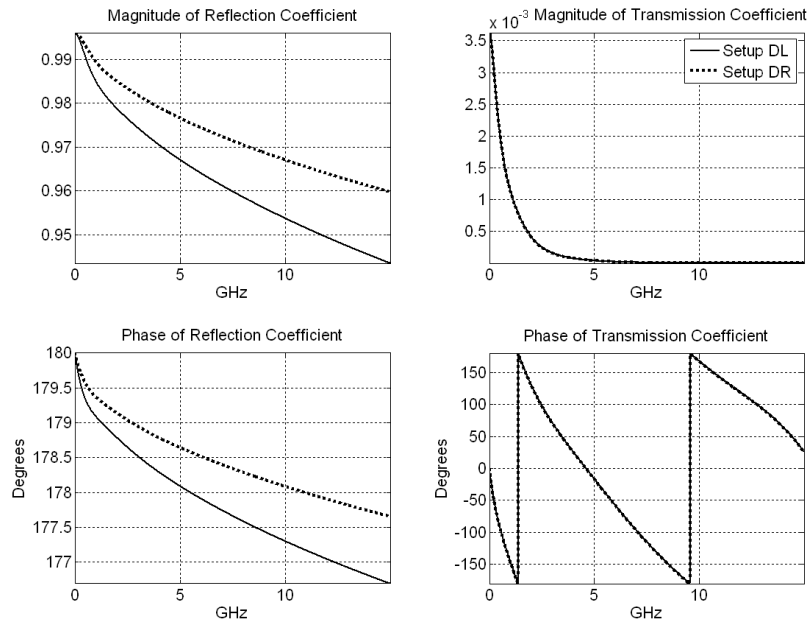
Figure 5.29. Reflection coefficients and transmission coefficients for the two setups DL and DR.

5.5.4.2 Symmetry with Fine Mesh setup

As a verification of the digital filter setup, consider the following pair of setups shown in Figure 5.30. They represent the fine mesh version of setups DL and DR discussed above. These setups use the same two materials that were used in the two-dimensional setups in the previous sections.
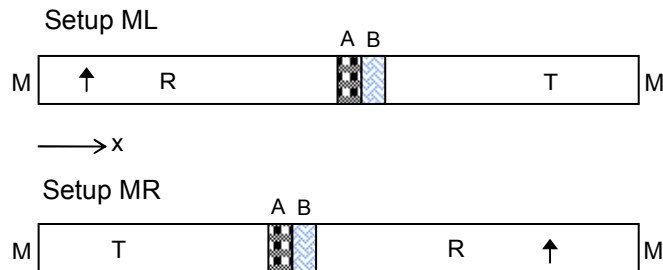
Figure 5.30. Two one-dimensional fine mesh setups. The excitation source is to the left of the reader in Setup ML. The excitation source is to the right of the reader in Setup MR. The reference setups are not shown.

The simulation parameters were set as follows: The space step (dl) is 0.05mm. The number of time iterations is $2^{17} = 131072$, which yields a

simulation time of 0.011μs. The setup size is 95 x 1 x 1 measured in *dl*.
The excitation is a Gaussian pulse with duration of 132ps. As with the
digital filter setups, the boundary conditions are set to characterise a
TEM transmission line, i.e., the setup ends (planes x = 0 and x = 94) are
set to matched condition. The y-direction walls (planes y = 0 and y = 1)
are set as perfect magnetic conductor (PMC). The z-direction walls
(planes z = 0 and z = 1) are set as perfect electric conductor (PEC).
Figure 5.31 shows the reflection coefficients and transmission
coefficients for the two setups ML and MR. This result verifies the
conclusion that was drawn from setups DL and DR.
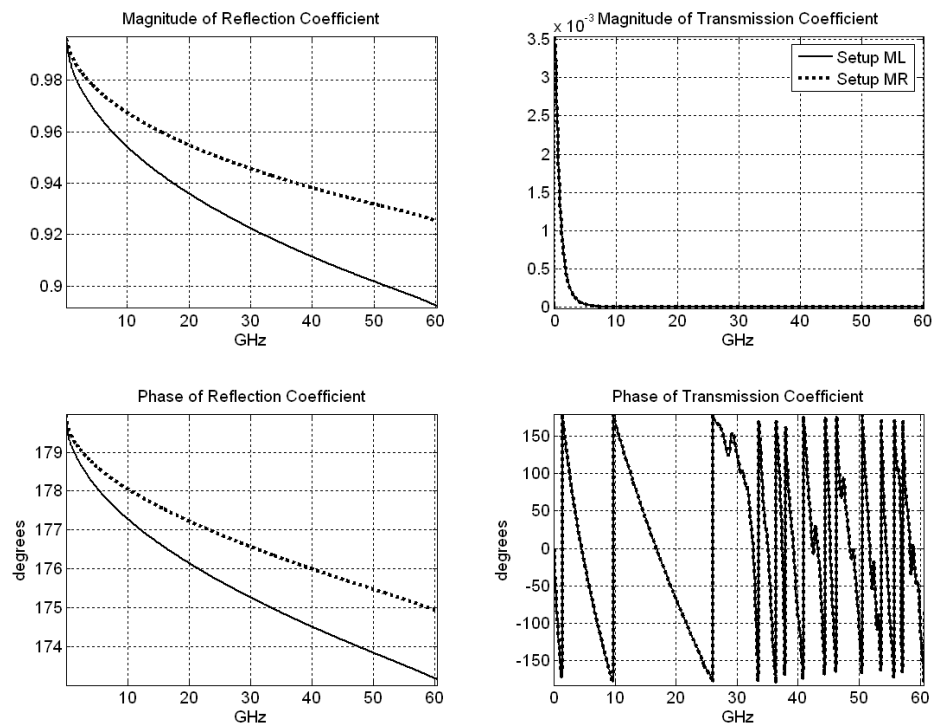
Figure 5.31. Reflection coefficients and transmission coefficients for the two
setups ML and MR.

Finally, Figure 5.32 shows the reflection coefficients and transmission
coefficients of the four setups: DL, DR, ML, and MR. The agreement
between the fine mesh and the coarse mesh/digital filter setups are
clearly illustrated.
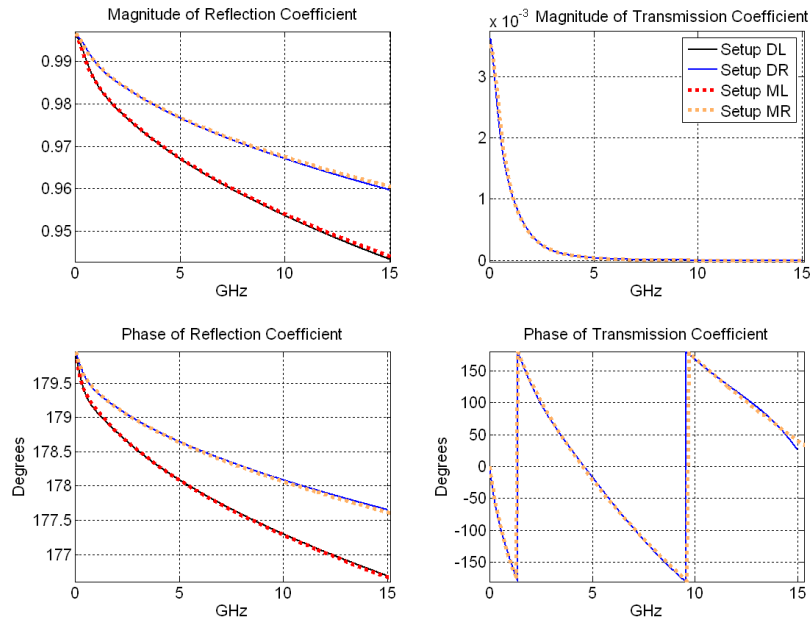
Figure 5.32. Reflection coefficients and transmission coefficients for the four setups DL, DR, ML, and MR.

5.6 Filter Stability

It is important to ensure that IIR filters are stable. This is because, in general, when a stable system is disturbed by a small input, the response of the system will eventually decay to zero or a constant value, or at most be bounded within a finite limit [5.26]. A linear time-invariant system is stable if its impulse response, *h(k)*, is absolutely summable or so called convergent [5.27]. This condition can be expressed mathematically as

$$\sum_{k=-\infty}^{\infty} |h(k)| < \infty \qquad (5.33)$$

The physical meaning is that the area under the discrete curve of the filter impulse response must be finite [5.28]. Throughout this project all the designed digital filters have been tested and proved to be stable. Using the complex plane, if at least one pole is located on the right-hand

side (i.e., if it has a positive real part), the filter is said to be unstable. Thus, to ensure stability, all the poles must not have a positive real part. This is ensured on all the filters involved in modelling the setup. Figures 5.33, 5.34, and 5.35 show the locations of poles and zeros for the filters that model the cascade coefficients S_{11}, S_{21}, and S_{22} respectively as they have been derived in the example discussed in §5.5. Poles are drawn as crosses and zeros are drawn as circles. The values of these poles and zeros are listed in Table 5.5 stated in §5.5.2.1.4.
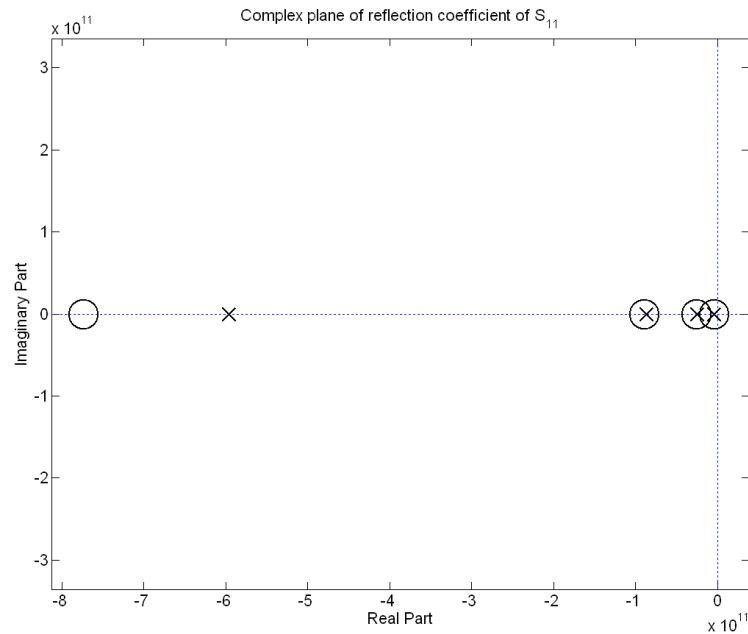
Figure 5.33. A Pole-zero diagram for parameter S_{11}. A Pole is shown as a cross and a zero is shown as a circle.
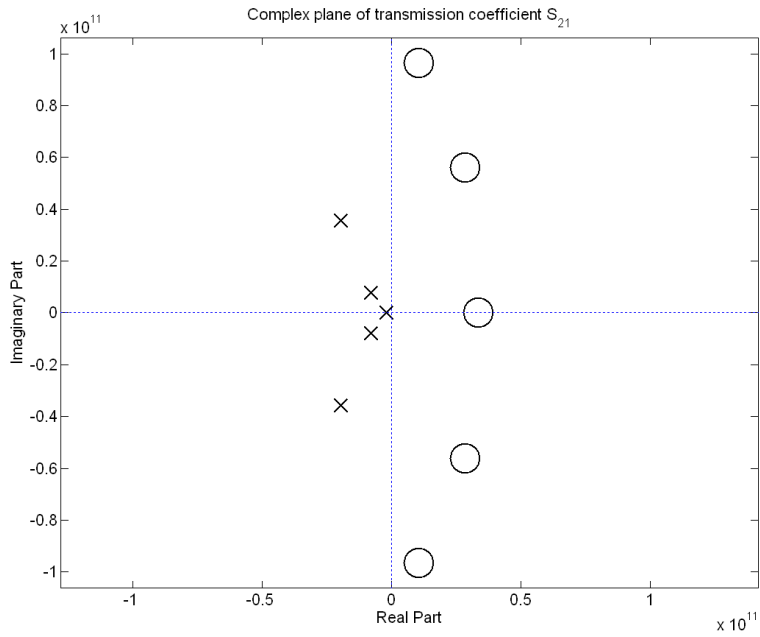
Figure 5.34. A Pole-zero diagram for parameter S_{21}. A Pole is shown as a cross and a zero is shown as a circle.
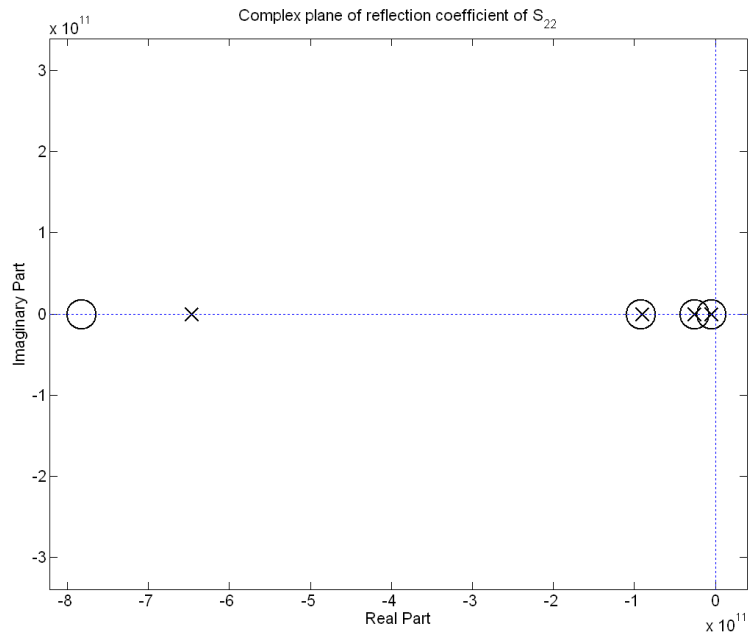
Figure 5.35. A Pole-zero diagram for parameter S_{22}. A Pole is shown as a cross and a zero is shown as a circle.

5.7 Speedup with Digital Filtering

Speeding up modelling simulation was achieved when replacing the fine mesh of a thin layer with a digital filter and a coarse mesh. This section

will deduce a relationship between speedup and the frequency range over which the shielding effectiveness is calculated. Simulation speedup (S) in terms of elapsed time can be defined as

$$S = \frac{T_{em}}{T_{eDF}} \qquad (5.34)$$

where T_{em} is elapsed time of fine mesh simulation and T_{eDF} is elapsed time of simulation of digital filter with coarse mesh.

It was found that speedup (S) can be given as

$$S = F \frac{C_m}{C_{DF}} \qquad (5.35)$$

where C_m and C_{DF} are the total number of TLM cells for the meshed setup, and the digital filter with coarser mesh respectively. C_m and C_{DF} can be found from regSolve input file as the multiplication of NX by NY by NZ of the relevant case to obtain the volume of the space under modelling in units of dl^3. F is a factor that ranges between 0.7 and 0.9.

The use of factor F is because, in regSolve, N TLM cells can be modelled within shorter time than if there is a digital filter defined in these N cells. It has been found that simulation with no digital filter is faster so that it takes less run time by a factor of 0.7 to 0.9 and hence the use of F. This can be expressed as follows.

$$\text{if } C_m = C_{DF} \quad \rightarrow \quad T_{em} < T_{eDF} \Rightarrow T_{em} = F \cdot T_{eDF}$$

$$\frac{T_{em}}{T_{eDF}} < \frac{C_m}{C_{DF}} \rightarrow \frac{T_{em}}{T_{eDF}} = F \frac{C_m}{C_{DF}}$$

where F is less than one.

It is possible to write

$$\frac{C_m}{C_{DF}} = \left(\frac{dl_{DF}}{dl_m}\right)^D \tag{5.36}$$

since dl (space step) is scaled in the opposite way of scaling the dimensions in x, y, and z. Notice that dl_m and dl_{DF} are the space steps chosen for the meshed case and the digital filter with coarser mesh cases respectively. D can be 1, 2, or 3 depending whether the object under modelling is 1-D, 2-D, or 3-D in terms of TLM cells.

The valid frequency range is up to f_{max} which can be given by

$$f_{max} = \frac{c}{10 \, dl} \tag{5.37}$$

assuming 10 samples per wavelength as a minimum number of samples for a sufficient representation of one wavelength. c is the speed of light in free space.

Solving equation (5.37) for dl for the case of the digital filter setup yields

$$dl_{DF} = \frac{c}{10 \, f_{max \, DF}} \tag{5.38}$$

Substituting equation (5.38) in equation (5.36) implies

$$\frac{C_m}{C_{DF}} = \left(\frac{c}{10 \, dl_m \, f_{max \, DF}}\right)^D \tag{5.39}$$

By substituting equation (5.39) in equation (5.35) we obtain

$$S = F\left(\frac{c}{10 \, dl_m \, f_{max \, DF}}\right)^D \tag{5.40}$$

which is the speedup amount assuming that the number of time iterations (NT) is adjusted to obtain the same simulation time (T_S) for the fine and the coarse mesh as well. The following example demonstrates the use of the equations of this section.

Example

Consider a digital filter setup that is used for modelling with a total number of TLM cells of 50 x 60 x 50 = 150000 cells with dl_{DF} of 1mm. It is required to estimate the maximum useful frequency for this run and also the execution time of the corresponding fine mesh setup if dl_m is 0.1mm i.e., 10 times finer mesh. The simulation time for the DF case is 14 hours and 42 minutes = 882 minutes.

Let F be taken as 0.8 then speedup will be given as

$$S = F\left(\frac{C_m}{C_{DF}}\right) = F\left(\frac{dl_{DF}}{dl_m}\right)^D = 0.8\left(\frac{1mm}{0.1mm}\right)^3 = 0.8 \times 1000 = 800$$

where C_m =500 x 600 x 500 = 150 000 000 cells

$T_{em} = S\,(T_{eDF}) = 800$ x $882 = 705600$ minutes $= 11760$ hours $= 490$ days

Applying equation (5.40) we get

$$800 = 0.8\left(\frac{3 \times 10^8}{10 \times 10^{-4} \times f_{max\,DF}}\right)^3$$

Solving for f_{maxDF} yields f_{maxDF} = 30GHz.

However, the actual maximum frequency may be less than the calculated value depending on the physical model of the material under modelling. Another important point is that it is necessary when comparing between fine mesh and coarse mesh to run both of them for the same amount of simulation time (T_S). This can be set by adjusting the total number of time iterations (*NT*) in regSolve simulation. This is because the simulation time is

$$T_S = NT \cdot dt = NT \cdot \frac{dl}{2c} \tag{5.41}$$

where *dt* is the time step in TLM method.

5.8 Summary

This chapter has introduced the development of digital filters and has presented the reasons for adopting them for the thin panel problem. The presence of a thin panel can overburden the simulation with heavy computational costs in terms of memory and run time. The use of digital filters turns the modelling problem from fine mesh to coarse mesh. In this case, the limiting factor in equation (5.5) will probably be the second term, which is fulfilling that $dl < \lambda_{min}/10$. The need for filter cascading is also discussed. The cascading formulae are derived to cover cases where more than one embedded material panel is present in a sandwich. A speedup formula is derived to be used in assessing simulation speed compared to the conventional fine mesh method. It was demonstrated that the use of digital filter results in a substantial speed up in computation and also facilitates the modelling of complex configurations comprising several composite layers in different parts of the structure.

References

[5.1] E.C. Ifeachor and B.W. Jervis, *Digital Signal Processing: A Practical Approach*. Prentice Hall, Harlow, England, Second edition, 2002.

[5.2] C. Christopoulos, *Multi-Scale Modelling in Time-Domain Electromagnetics*. International Journal of Electronics and Communications, Vol. 57, No. 2, 2003, pp.100-110.

[5.3] H.W. Ott, *Electromagnetic Compatibility Engineering*. John Wiley & Sons Inc, New York, NY, 2009.

[5.4] K.L. Kaiser, *Electromagnetic Compatibility Handbook*. CRC Press, Boca Raton, 2005.

[5.5] C.C. Wong and W.S. Wong, *Multigrid TLM for Diffusion Problems*. International Journal of Numerical Modelling: Electronic networks, devices and fields, Vol. 2, pp.103-111, 1989.

[5.6] R. Ait-Sadi, A.J. Lowery and B. Tuck, *Combined Fine-Coarse Mesh Transmission-Line Modelling Method for Diffusion Problems*. International Journal of Numerical Modelling: Electronic networks, devices and fields, Vol. 3, pp.111-126, 1990.

[5.7] S.H. Pulko, I.A. Halleron and C.P. Phizacklea, *Substructuring of Space and Time in TLM Diffusion Applications*. International Journal of Numerical Modelling: Electronic networks, devices and fields, Vol. 3, pp.207-214, 1990.

[5.8] N.P.G. Smith and C. Christopoulos, *Models of Thin Panels in Combined Electromagnetic and Thermal Problems*. Fifth International Conference on Microwave and High Frequency Heating: 17-21 Sep 1995.

[5.9] J. Paul, C. Christopoulos and D.W.P. Thomas, *Generalized material models in TLM – Part 1: Materials with frequency-dependent properties*. IEEE Transactions on Antennas and Propagation, Vol. 47, pp. 1528-1534, Oct 1999.

[5.10] J. Paul, C. Christopoulos and D.W.P. Thomas, *Generalized material models in TLM – Part 2: Materials with anisotropic properties*.

IEEE Transactions on Antennas and Propagation, Vol. 47, pp. 1535-1542, Oct 1999.

[5.11] J. Paul, C. Christopoulos and D.W.P. Thomas, *Generalized material models in TLM – Part 3: Materials with nonlinear properties*. IEEE Transactions on Antennas and Propagation, Vol. 50, pp. 997-1004, Jul 2002.

[5.12] J. Paul, V. Podlozny, D.W.P Thomas and C. Christopoulos, *Time-domain simulation of thin material boundaries and thin panels using digital filters in TLM*. Turkish J. Elect. Eng. Comp. Sci., Vol. 10, no.2, pp.185-198, 2002.

[5.13] J. Paul, V. Podlozny and C. Christopoulos, *The Use of Digital Filtering Techniques for the Simulation of Fine Features in EMC Problems Solved in the Time Domain*. IEEE Transactions on Electromagnetic Compatibility, Vol.45, No.2, May 2003.

[5.14] J. Paul, M. Alsadi and C. Christopoulos, *Simulation of Thin Conductive Panels Using Digital Filters in Transmission-Line Modelling*. EMC Europe 2010, September 13-17, Wroclaw, Poland.

[5.15] *Understanding Poles and Zeros,* Analysis and Design of Feedback Control Systems, Department of Mechanical Engineering, Massachusetts Institute of Technology, 2002. Accessed on web.mit.edu/2.14/www/Handouts/PoleZero.pdf on 30 Dec 2011.

[5.16] A. Karousos, G. Koutitas and C. Tzaras, *Transmission and Reflection Coefficients in Time-Domain for a Dielectric Slab for UWB Signals*. 2008 IEEE 67th Vehicular Technology Conference – Spring VTC, Marina Bay; Category number CFP08VTC, code 72724.

[5.17] K. Sato, H. Kozima, H. Masuzawa, T. Manabe, T. Ihara, Y. Kasashima, and K. Yamaki, *Measurements of reflection characteristics and refractive indices of interior construction materials in millimeter-wave bands*. IEEE 45th Veh. Technol. Conference vol. 1, pp. 449-453, 25-28 Jul 1995.

[5.18] P.C.D. Hobbs, *Building Electro-optical Systems: making it all work*. John-Wiley and Sons, New Jersey, second ed., 2009.

[5.19] Matlab help on `invfreqs.m`, Mathsworks.

[5.20] B.Gustavsen, *User's Guide for vectfit3.m Fast, Relaxed Vector Fitting for Matlab*. 2008.

[5.21] J. Paul, *A 3-D Time-Domain TLM Electromagnetic Field Solver: The regSolve Manual*. University of Nottingham, UK, July 2008.

[5.22] D.A. Frickey, *Conversions between S, Z, Y, h, ABCD, and T Parameters which are Valid for Complex Source and Load Impedances*. IEEE transactions on Microwave Theory and Techniques, Vol. 42, No. 2 Feb 1994, pp.205-211.

[5.23] A.L. Drozd, *Progress on the Development of Standards and Recommended Practices for CEM Computer Modeling and Code Validation*. Proceedings of the 2003 IEEE Symposium on EMC, Boston, MA, pp. 313-316, 18-22 August 2003.

[5.24] L. D. Landau and E. M. Lifshitz, *Electrodynamics of Continuous Media.* Addison-Wesley, Reading, MA, 1960.

[5.25] D.K. Cheng, *Fundamentals of Engineering Electromagnetics*. Addison-Wesley, Reading, 1993

[5.26] B.A. Shenoi, *Introduction to Digital Signal Processing and Filter Design.* John Wiley & Sons Inc, New Jersey, 2006.

[5.27] J.G. Proakis and D.G. Manolakis, *Digital Signal Processing*, Prentice-Hall, Second edition, 1996.

[5.28] K.V. Rangarao and R.K. Mallik, *Digital Signal Processing: A Practitioner's Approach*. John Wiley & Sons Inc, West Sussex, England, 2005.

6

Model Evaluation Based on Simulated Results for SE and S_{21}

The purpose of this chapter is to present an overview of the results that were achieved by simulating the developed models. A discussion of the simulation design parameters will be followed by presenting the effect of certain features in the model. Some noticeable observations will be demonstrated along with their interpretation. The key simulation results will be shown along with their discussion and analysis.

6.1 Introduction

The main work was simulating different setups of objects with various features and excitation sources. Results are presented starting with the geometry of the setup. The simulation settings are listed in tables after each result figure. If not otherwise stated, the implemented digital filters have the same number of poles (*NP*) and that of zeros (*NZ*). Assuming that the number of poles equals the number of zeros, then each digital filter has a set of 2(*NPr*+1) coefficients characterising its reflection parameter and 2(*NPt*+1) coefficients for its transmission parameter, where *NPr* is the number of poles in the reflection coefficient and *NPt* is the number of poles in the transmission coefficient. The digital filter coefficients are listed in Appendix A.

Simulations were performed using *regSolve*[*] software [6.1] with permission from Dr J. D. Paul. Pre-processing and Post-processing with plotting the results were performed using Matlab script [6.2].

---

[*] regSolve code was developed by Dr John D. Paul using C programming language. It is based on the TLM method.

6.2 Simulation Design

There are a number of parameters that affect model performance. Models are applicable over a range of parameters. All these factors need to be taken into consideration when post-processing the simulation results.

6.2.1 Simulation Parameters

A simulation requires setting of a number of parameters. Among these are the source of excitation, time iterations, and the boundary conditions.

6.2.1.1 Excitation Source

Throughout this work, the source of excitation was chosen according to specific set of parameters. These parameters provide the required stimulus.

The excitation was chosen to be a Gaussian pulse since it has a smooth rising edge and smooth falling edge. This is necessary to obtain a Gaussian-shape frequency spectrum and has no pre-ripple and post-ripple caused by Gibbs phenomenon as it is the case with a rectangular pulse shaped excitation. A Gaussian pulse has a limited frequency range when compared with the rectangular pulse. The Gaussian pulse duration is set to 132ps which gives a frequency range that extends from DC up to around 10.7GHz when the amplitude spectrum falls into its 3dB point. This choice results in the desired simulation maximum frequency range as well as the available laboratory equipment frequency range.

6.2.1.2 Time Iterations

The total simulation time (T_S) can be found by

$$T_S = NT \cdot dt \tag{6.1}$$

where NT is the total number of iterations and dt is the time discretisation step. The next two subsections will comment on the choice of dt and NT.

6.2.1.2.1 Discretisation

The time step is determined according to the space discretisation step (dl) as given by

$$dt = \frac{dl}{2c} \tag{6.2}$$

where c is the speed of light in free space, which equals 2.99792458×10^8 m/s. For a given object dimensions, minimum excitation wavelength (λ_{min}), and the thickness of the panel (L_d) to be represented by a digital filter, then the space step (dl) can be determined according to equation (5.5) which is revisited here as

$$5L_d \leq dl \leq Min\left[\frac{L_{min}}{5}, \frac{\lambda_{min}}{10}\right] \tag{6.3}$$

where L_{min} is the thickness of the panel that is modelled by a digital filter.

To let the time step (dt) adequately resolve the excitation pulse, the excitation pulse duration needs to be at least twenty to forty times the time step.

6.2.1.2.2 Number of Time Steps

The basic condition for choosing an adequate number of time steps (*NT*) is that it should be at least twice the maximum number of the object dimensions expressed in numbers of TLM cells. This is expressed as

$$NT_{\min} \geq 2 \times \left[Max(NX, NY, NZ)\right]$$ (6.4)

where *NX, NY*, and *NZ* represent the dimensions of the object under modelling with units of *dl* metres in the directions of x, y, and z respectively. This condition will allow at least one complete pulse reflection from all the walls. In practice, several transitions are necessary for good accuracy. For lossy material *NT* needs to be increased to a higher number in order to cope with the pulse dispersion. Setting the right number of *NT* is important to obtain a reliable frequency response in the lower frequency region. Finally, it is always recommended to round up the resultant *NT* value from the above discussion to be in a form of two raised to a power of an integer. This will eliminate the need to add padded zeros when computing the Fast Fourier Transform (FFT) to find its frequency response. Adding padded zeros can affect the resolution of the frequency domain response which produces a non-smooth curve especially at lower frequencies.

6.2.1.3 Boundary Conditions

The walls of the modelled cavity that contains the panel must be set appropriately. In the examples shown, one or more of the following boundary states have been used.

- Perfect Electric Conductor (PEC) that has a reflection coefficient of minus one and hence shows total reflection that is out of phase of the incident field,

- Perfect Magnetic Conductor (PMC) that has a reflection coefficient of one and hence shows total reflection that is in-phase with the incident field. In real life, this state is not easily obtained. However, in simulation, it is the choice of an open boundary and used as a periodic boundary condition,

- Matched (M) that can be thought of as applying a total absorption of the incident field.

In the one-dimensional case, the Transverse Electromagnetic (TEM) waveguide has been chosen to be simulated. This arrangement requires periodic boundaries to be set as shown in Figure 6.1.
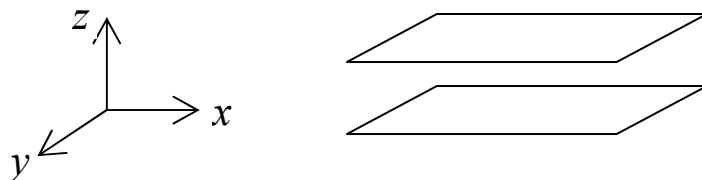
Figure 6.1. One-dimensional model resembling TEM waveguide arrangement. Boundary conditions are set such as M in x, PMC in y, and PEC in z.

The choice of setting the z planes (the upper and lower planes) to PEC is necessary to let the setup support the TEM mode and hence getting a propagating wave along the waveguide.

Two- and three-dimensional cases can be simulated as a rectangular waveguide. This arrangement requires boundaries to be set as shown in Figure 6.2.
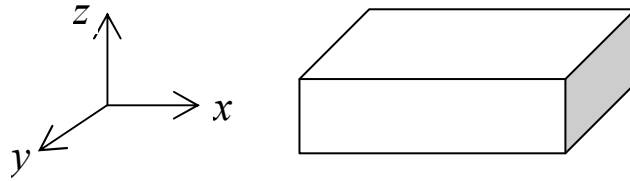
Figure 6.2. Two- and three-dimensional model that represent a metallic waveguide with boundary conditions are set such as M in x, PEC in y and z.

When a cavity is simulated using a conducting walls, it will act as a cavity resonator, which is a feature that can be used to check the resonant frequencies of the relevant laboratory measurements.

6.2.2 Post Processing

Simulation using regSolve produces a set of data files that can be processed and displayed using Matlab script. Certain issues need to be taken into consideration when processing these data files.

6.2.2.1 Frequency Range

Every simulated model has a frequency range that is defined by the minimum frequency (f_{min}) and the maximum frequency (f_{max}). This frequency range defines the domain over which reliable data can be used and displayed.

6.2.2.1.1 Minimum Frequency

In a three-dimensional TLM simulation, every one time step (dt), the excitation pulse traverses a distance of half the space discretisation ($dl/2$) metre. Thus, larger wavelengths (lower frequency components) require

longer simulation time ($NT \times dt$) in order to be fully resolved. Therefore, there is a lower frequency limit below which the frequency components are not fully resolved and hence should be excluded when post-processing the simulated data. From the above, one can deduce that for a given space step (dl), the minimum frequency (f_{min}) can be improved (lowered) by increasing the number of time iterations (NT). More analysis for the steady-state solution by TLM can be found in [6.3].

The minimum useful frequency (f_{min}) can be determined by producing a frequency response plot of the simulated data using the total number of time iterations (NT). This first plot will be regarded as the reference plot that is assumed to have lower f_{min} than the next plot. Then, the same plot is re-produced using the number of points which is half the number of time iterations, i.e., $NT/2$. A third plot can be produced by further halving the last number of points to work on $NT/4$ points. By plotting the produced plots on the same grid, the minimum frequency for each case of the two cases can be determined. To decide f_{min} for a given simulation, a relatively large number of time iterations (NT) is required since $NT/2$ and $NT/4$ should still satisfy equation (6.4).

An example of estimating the minimum frequency is illustrated in Figure 6.3. The magnitude of S_{21} is shown for two cases (with and without the material) for the same setup. For each of the two cases, the simulation is carried out with five values of the number of time iterations (NT). Obviously, at higher frequencies, all these curves agree. It is noticeable that the case of no material needs more time iterations to reach the same f_{min} value of the case with a lossy material. This can be explained by the

fact that the excitation wave decays (and hence reaches the steady state) faster in lossy materials.
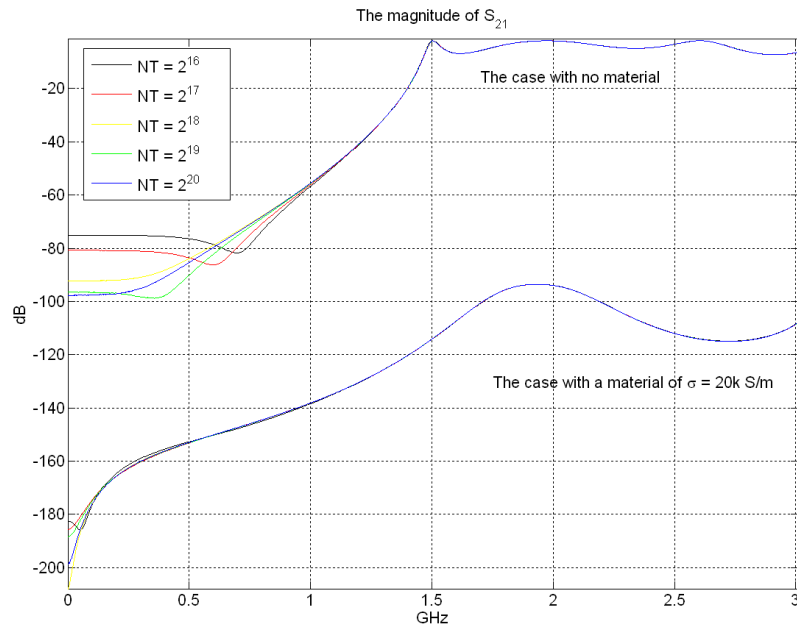
Figure 6.3. The effect of the number of time iterations (*NT*) on the magnitude of S_{21} is less prominent with the presence of a lossy material.

Figure 6.4 takes a closer look at the case when there is no material. Presuming that the case of $NT = 2^{20}$ (the blue curve) is the reference curve to compare with; the other curves show "departure" from the reference at different frequencies. These departure frequencies are regarded in this study as the minimum frequencies corresponding to the relevant value of *NT*.
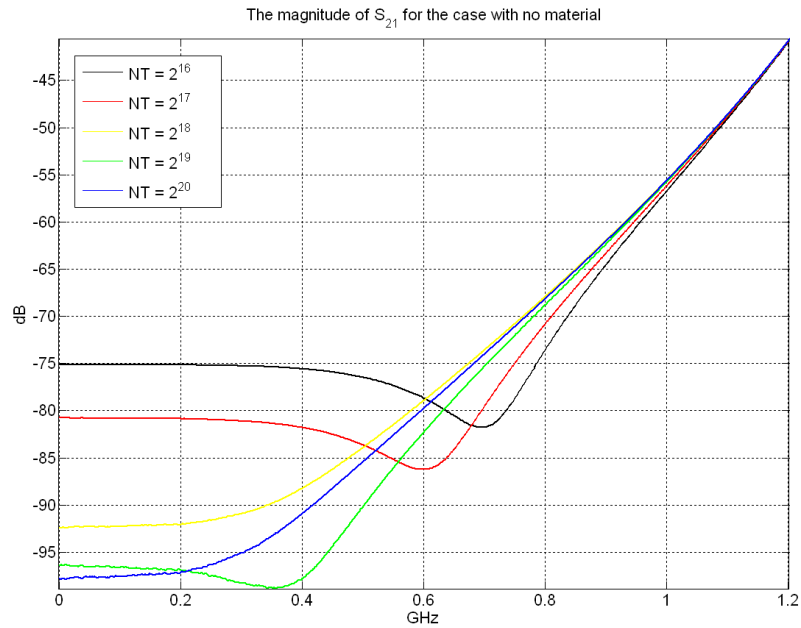
Figure 6.4. The first 1.2GHz of the set of curves obtained in Figure 6.3 above showing the case when no material present.

Similarly, Figure 6.5 shows the case with a lossy material. It is interesting to notice here that the case of $NT=2^{16}$ has a minimum frequency of about 450MHz while the rest of the curves have minimum frequencies which are less than 150MHz. The last two numbers are stated assuming that a difference by more than 0.5dB is unacceptable.
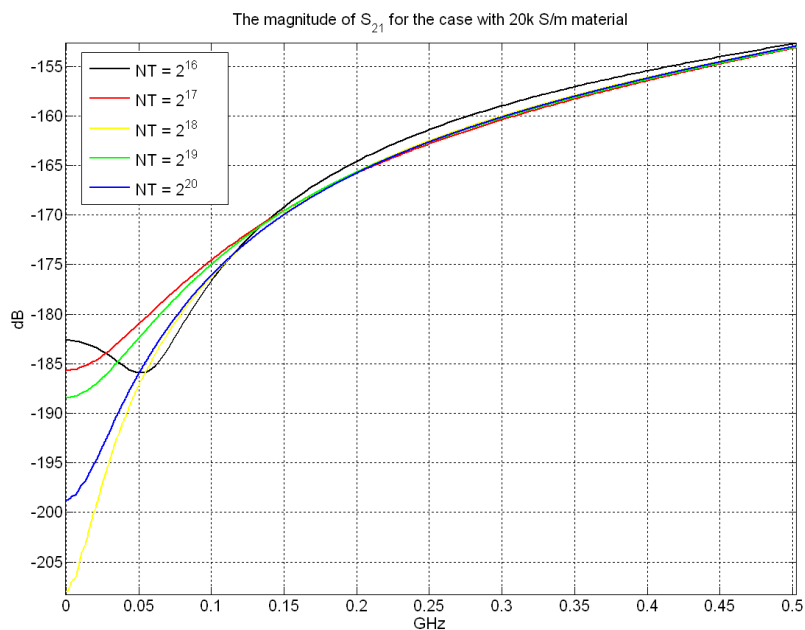
Figure 6.5. The first 0.5GHz of the set of curves obtained in Figure 6.3 above showing the case when a lossy material with $\sigma = 20$k S/m present.

6.2.2.1.2 Maximum Frequency

For an object with a panel made of a given material, the maximum useful frequency can be determined according to two factors. These are space discretisation and excitation pulse spectrum.

1. *Space Discritisation*: The minimum wavelength of the excitation needs to be represented by typically ten samples. The relevant maximum useable frequency is hence given by

$$f_{max} = \frac{c}{\lambda_{min}} \Rightarrow f_{max} = \frac{c}{10\,dl} \qquad (6.5)$$

where the constant c is the speed of light in free space and it equals 2.99792458×10^8 m/s.

2. *Excitation Spectrum*: It was noticed from simulation that the narrower the Gaussian pulse is, the higher the maximum useful frequency can be achieved. This is because of the increased bandwidth in the frequency domain. It was found from simulation that the Gaussian pulse spectrum can still have enough energy to represent wide range of frequencies. In this case, a bandwidth of up to the point of around -60dB from the maximum response can still give reliable interpretations for the reflection and transmission coefficients.

In general, space discritisation is the dominant factor with coarse mesh setups. On the other hand, the excitation spectrum is the dominant factor

in the case of fine mesh. This is because in the case of fine mesh, the space step (*dl*) is much smaller than that with the coarse mesh. This leads to producing a value for f_{max} defined by equation (6.5), which is greater than the 60-dB bandwidth. Thus, a unified statement can be made as shown in equation (6.6) for a given material properties.

$$f_{max} = Min \left[\frac{c}{10 \ dl}, BW_{Gaussian} \right] \qquad (6.6)$$

where BW$_{Gaussian}$ is the Gaussian pulse 60dB-bandwidth.

6.2.2.2 Resonant Frequencies

When exciting a cavity with conducting walls, a resonant pattern is formed in the cavity at certain frequencies. Rectangular cavities were used in this project. The values of resonant frequencies in a rectangular cavity are given by [6.4]

$$f_{mnp} = \frac{u}{2} \sqrt{\left(\frac{m}{a}\right)^2 + \left(\frac{n}{b}\right)^2 + \left(\frac{p}{d}\right)^2} \qquad (6.7)$$

Equation (6.7) is valid for both TE$_{mnp}$ and TM$_{mnp}$ modes, where u is the speed of light in the medium that fills the cavity. It is given by equation (6.8) in terms of the permeability (μ) and permittivity (ε) of the medium.

$$u = \frac{1}{\sqrt{\mu\varepsilon}} \qquad (6.8)$$

The three constants *a*, *b*, and *d* are the inner dimensions of the cavity along the *x*, *y*, and *z* coordinates respectively as shown in Figure 6.6.
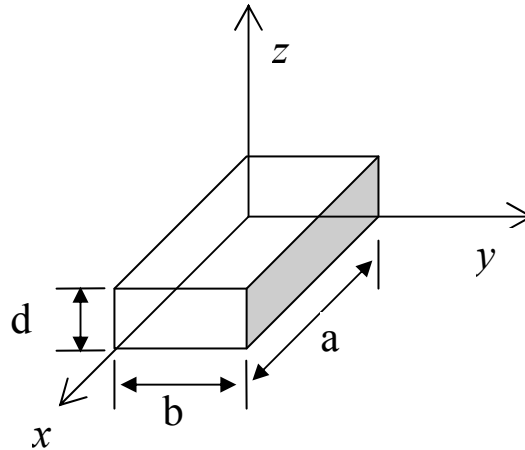
Figure 6.6. Coordinates of a rectangular cavity.

The three integers m, n, and p represent the number of half-wave periodicity in the x, y, and z directions respectively. There are some restrictions [6.5] on the possible values of m, n, and p. In the TE$_{mnp}$ modes, p should not equal zero; also, m and n should not both be equal to zero. In the TM$_{mnp}$ modes, neither m nor n should equal zero.

In the next figures, wherever applicable, the resonant frequencies will be indicated on the same grid in a form of vertical lines. These lines extend to the same height and are located at the relevant resonant frequencies calculated according to equation (6.7).

6.2.2.3 Penetration Time

The time of penetration shows the amount of delay that the incident pulse has experienced when penetrating the object by diffusion. When post-processing the simulated time-domain pulses, the penetration time can be found as the time difference between the peaks of two pulses. The first is the free space pulse in the case when no object is present and the

second is the transmitted pulse through the object, as demonstrated by

Figure 6.7.
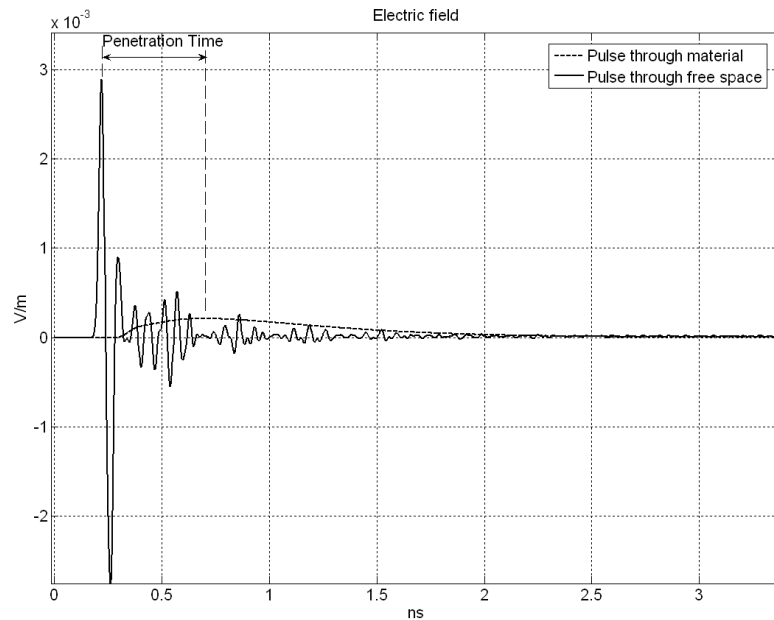
Figure 6.7. An example on how to find the penetration time where the pulse transmitted through the material is multiplied by 1000 to get comparable amplitude with the free space pulse.

6.3 Verification with Fine Mesh

It was shown in §5.5.3 that there is an agreement between fine mesh and

the corresponding coarse mesh in terms of the reflection/transmission

properties. Two-dimensional models were used for that purpose. In this

section, a comparison between fine and coarse-mesh setups will be

performed in terms of the shielding effectiveness for a three-dimensional

model as shown in Figure 6.8.
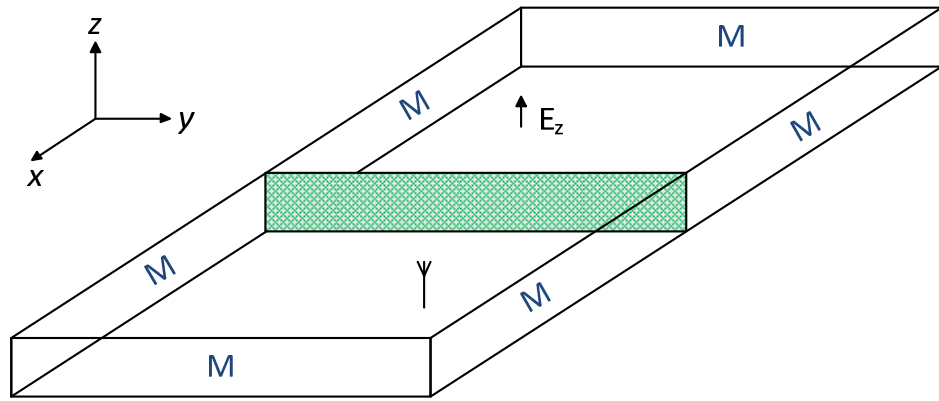
Figure 6.8. The geometry that is used in verifying coarse mesh with fine mesh.

Figure 6.8 represents a closed rectangular cavity with matched (M) boundary conditions in the x- and y-dimension side walls. Perfect Electric Conductor (PEC) boundary conditions were used for the z-dimension planes. The digital filter plane splits the cavity into two sub-cavities; each one has half the original volume. The excitation pulse has a Gaussian shape with a time-duration of 132ps and it is linearly-polarised in z-direction. As indicated in Table 6.1, the coarse mesh/digital filter model was derived from the fine mesh configuration by scaling up the space discretisation (*dl*) by a factor of 21. Accordingly, the space dimensions were scaled down by the same factor (21 times). It was not feasible to scale all the dimensions by 21. This is because of the large computation effort that would be produced in the fine mesh model. Therefore, this scaling has been applied on x- and y-dimensions only because they are more crucial than the z-dimension, which is parallel to the excitation polarisation. The highest feasible z-dimension is chosen as 0.5mm for the fine mesh compared to the coarse mesh of 6.3mm.

135

It is obvious from Figure 6.9 that there is a good agreement up to around 8GHz after which a difference of about 2dB of shielding effectiveness is introduced.
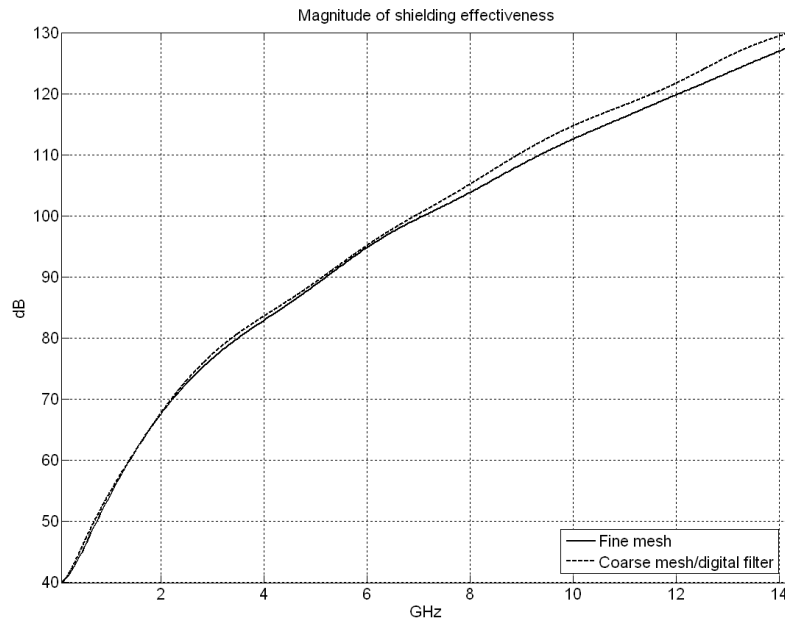
Figure 6.9. The magnitude of shielding effectiveness of a fine mesh conventional setup and its corresponding coarse mesh setup after using a digital filter to represent the embedded material.

Parameter	Fine mesh	Coarse mesh/DF
NT	131072	
$NX.NY.NZ$	882 x 441 x 5	42 x 21 x 3
dl (mm)	0.1	2.1
dt (ps)	0.166782	3.50242
Excitation signal	Gaussian pulse at z	
Excitation point	(220,115,1)	(10,5,1)
Number of poles	n/a	NPr=3 ; NPt=5
σ (S/m)	Cascade 0.5k + 1k	
L_d (mm)	Cascade 1 + 1	
ε_r	5	
Receiving point	(661,325,1)	(31,15,1)

Table 6.1. The simulation settings that produced Figure 6.9.

6.4 Shielding Effectiveness Simulation

A conductive box with one face including a panel made of a dielectric lossy material is simulated as illustrated in Figure 6.10. The aim is to find the shielding effectiveness of the box and the panel. In the following

136

sections, the effect of the material conductivity, panel dimensions, mesh size, excitation, position of the receiving point, and the panel thickness will be discussed.
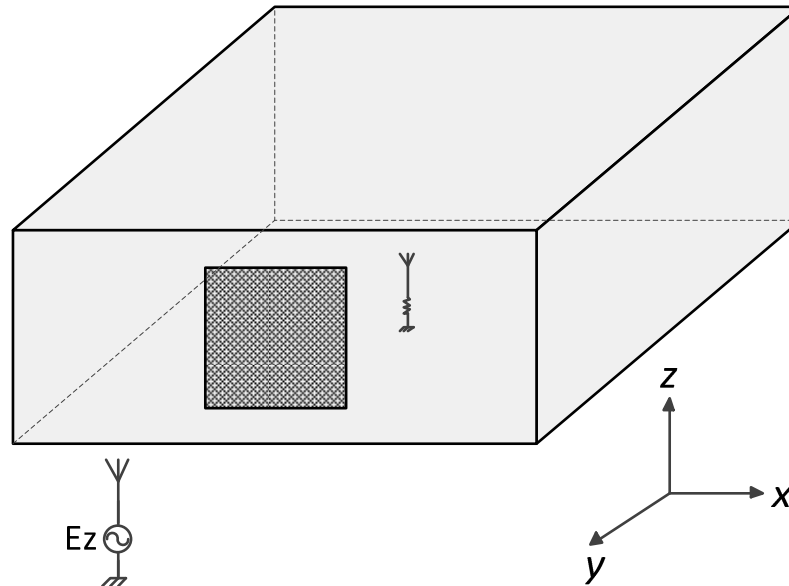
Figure 6.10. The setup that represents the model of the conductive box with the lossy material square panel on one face.

6.4.1 The Effect of Panel Material Conductivity

The geometry shown in Figure 6.10 has been used as a template to model the effect of the material conductivity. Figure 6.11 illustrates the shielding effectiveness for six different values of conductivity ranging between 500 S/m and 8000 S/m. In addition to that, the bottom curve shows the case when removing the panel from its window leaving a "free-space aperture". These seven models share the simulation parameters stated in Table 6.2.
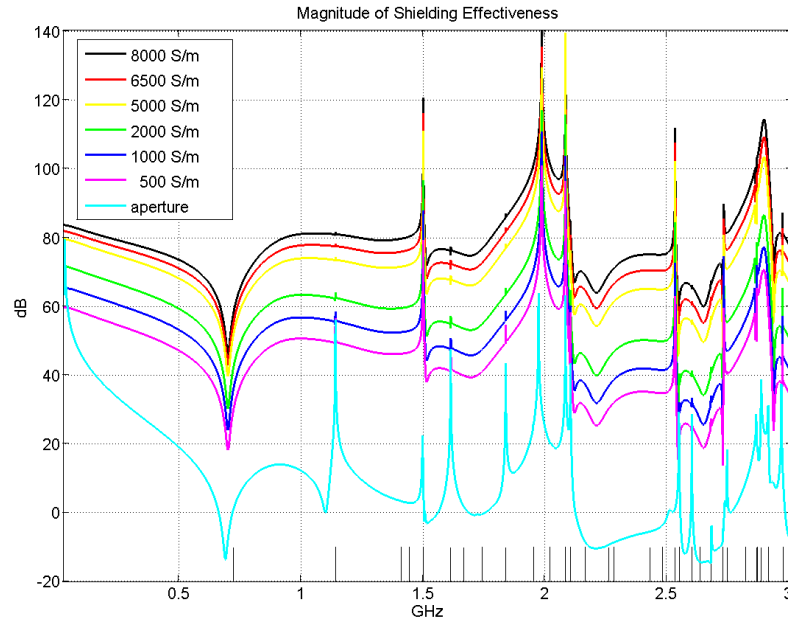
Figure 6.11. The shielding effectiveness of the box shown in Figure 6.10 with 78mm-by-78mm panel made of six different conductivities. The shielding effectiveness of an aperture window in the place of the panel is shown for comparison.

Parameter	Shared settings
NT	131072
NX.NY.NZ	49 x 49 x 19
dl (mm)	6.0
dt (ps)	10.0069
Excitation with polarisation	Gaussian pulse at z
Excitation plane	68 x 0 x 38
Number of poles	NPr=5 ; NPt=6
L_d (mm)	0.5
ε_r	5
Receiving point	(34,34,10)

Table 6.2. The simulation settings that produced Figure 6.11.

As it is expected, the higher the conductivity is, the higher the shielding effectiveness will be. The analytic values of the resonant frequencies are shown in a form of short vertical lines at the relevant frequencies. The conductivity value affects the shielding effectiveness such that doubling the conductivity means adding 6 dBs on the shielding effectiveness. This is noticeable when checking, for example, the difference between the 1000 S/m and the 2000 S/m curves. Moreover, it is clear that increasing

138

the conductivity from 6500 S/m to 8000 S/m have a smaller effect on SE when compared to increasing the conductivity from 1000 S/m to 2000 S/m. This point is important when considering the trade off between increasing the conductivity (which is accompanied with a high cost) and the gain in the corresponding SE. The aperture curve can be regarded as a reference curve from which the shielding effectiveness can be determined for certain conductivity at a given frequency.

6.4.2 The Effect of Panel Dimensions

Last section has discussed changing the material conductivity for a given geometry. This section discusses changing the window dimensions for a given material. Three different dimensions will be applied here as shown in Figure 6.12.
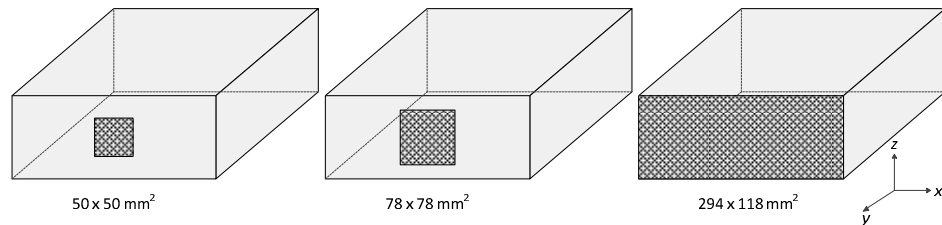
Figure 6.12. The geometry of Figure 6.10 in three different sizes for the panel.

These three boxes are modelled with the same conductivity (9000 S/m) for the panel material. Figure 6.13 shows the shielding effectiveness for the three cases with and without the presence of their panels. Table 6.3 states the simulation parameters common by the three models.
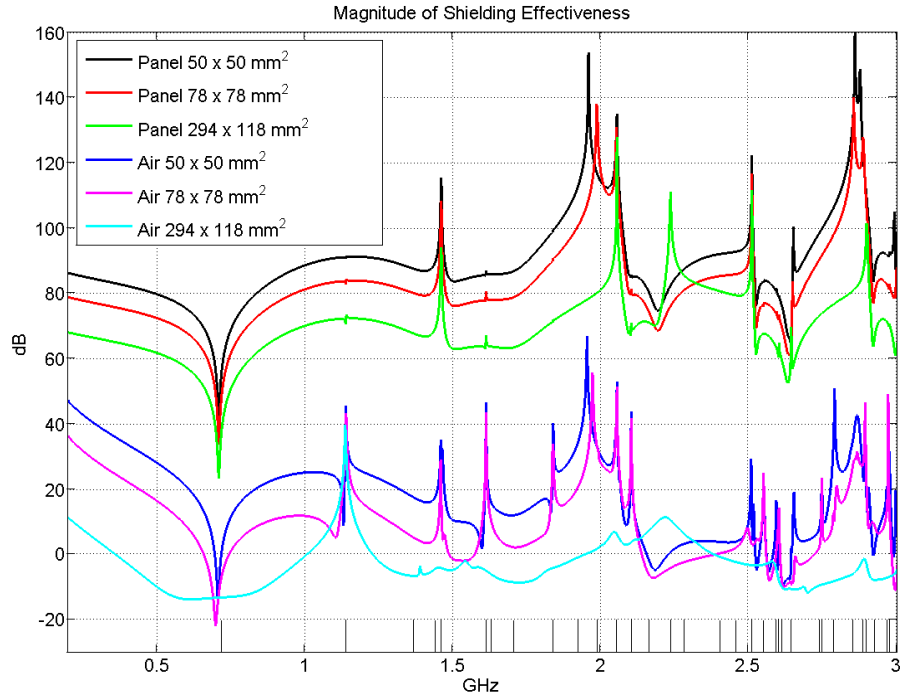
Figure 6.13. The shielding effectiveness of three different sizes of a panel made of conductivity of 9kS/m compared to the corresponding cases with no panels, which can be considered as air windows.

Parameter	Shared settings
NT	131072
NX.NY.NZ	147 x 147 x 59
dl (mm)	2.0
dt (ps)	3.33564
Excitation signal	Gaussian pulse at z
Excitation plane	(166 x 0 x 79)
Number of poles	NPr=5 ; NPt=6
σ (S/m)	9000
L_d (mm)	0.5
ε_r	5
V point	(83,83,10)

Table 6.3. The simulation settings that produced Figure 6.13.

As shown in Figure 6.13, the larger the window allows for higher field intensity to go through inside the box. This means a smaller shielding effectiveness than the case of smaller window. Table 6.4 indicates the area of each window along with one sample of shielding effectiveness taken at 1GHz.

140

Window name	Dimensions (mm)	Area (m²)	|SE| @ 1GHz (dB)		|SE| gain (dB)
			No panel	With panel	
Small window	50 x 50	0.0025	25.09	88.43	63.34
Large window	78 x 78	0.006084	11.85	81.12	69.27
Face window	294 x 118	0.034692	-0.70	69.95	70.65

Table 6.4. The features of the three windows used to produce Figure 6.13.

The effect of the panel presence. Figure 6.13 shows that the introduction of the panel has made a dramatic improvement to the shielding capability. The improvement is around 65dB. Table 6.4 shows that at 1GHz, the shielding effectiveness gets better improvement when introducing the panel in the larger window. It is also clear that the SE curve of the face window with no panel has no noticeable resonant-frequency spikes. This is because with the case of an air-window, the concept of a cavity is not valid any longer.

The effect of the panel size. For the next analysis, the shielding effectiveness at the frequency of 1GHz will be considered. From Table 6.4, one can relate the area multiplier (the ratio between two areas) to the SE improvement as follows.

$$\frac{A_L}{A_S} = 2.43360 \xrightarrow{\text{SE improved by}} 7.31\,dB \equiv 2.320$$

$$\frac{A_F}{A_L} = 5.70217 \xrightarrow{\text{SE improved by}} 11.17\,dB \equiv 3.618$$

$$\frac{A_F}{A_S} = 13.8768 \xrightarrow{\text{SE improved by}} 18.48\,dB \equiv 8.395$$

where A_F, A_L, and A_S are the areas of the face window, large window, and the small window respectively. These three observations can form three points in the plot shown in Figure 6.14. Since an "original"

window area (multiplied by one) has no SE improvement (SE is improved by one time) then a fourth point can be added as (1,1), as shown in Figure 6.14. Linear fitting has been applied to these four points with R-squared value of 0.9941 indicating a good fitting. This implies that at 1GHz for the case under discussion, if the panel area is multiplied by m_A, the shielding effectiveness (in ratio form) can increase by m_S times, following the equation

$$m_S = 0.5577\, m_A + 0.6244 \tag{6.9}$$
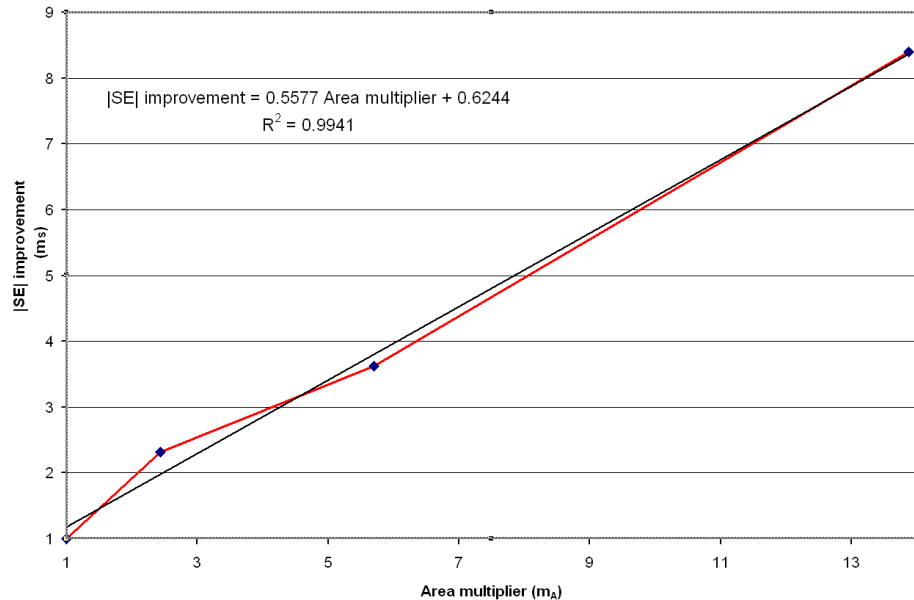
Figure 6.14. The almost linear relationship of the improvement in the SE versus the multiplier of the panel area for the geometry shown in Figure 6.12 when analysed at 1GHz.

6.4.3 The Effect of Mesh Size

The geometry shown in Figure 6.10 is used to model a half-millimetre thick panel in its window with conductivity of 6500 S/m. The space discretisation parameter (*dl*) has been chosen to take six values ranging between 2.0mm and 8.9mm. Table 6.5 indicates the space- and time-step

for each model along with the box dimensions, excitation and receiving

point coordinates.

dl (mm)	dt (ps)	NX.NY.NZ	Excitation plane	Receiving point
2.0	3.33564	147 x 147 x 59	166 x 0 x 79	(83,83,10)
4.7	7.78316	63 x 63 x 25	82 x 0 x 44	(41,41,10)
5.2	8.60244	57 x 57 x 23	76 x 0 x 42	(38,38,10)
6.0	10.0069	49 x 49 x 19	68 x 0 x 38	(34,34,10)
7.2	11.9595	41 x 41 x 17	60 x 0 x 36	(30,30,10)
8.9	14.8588	33 x 33 x 13	52 x 0 x 32	(26,26,10)

Table 6.5. The dimensions used to test the effect of the mesh size.

Figure 6.15 illustrates the shielding effectiveness for these six cases of

space discretisation coarseness. As can be seen, the change of space step

(dl) did not change the main features and pattern in the SE performance.

The slight changes are partially due to the difficulty to model exactly the

same dimensions of the box. In this way, larger error will be introduced

with coarser space discretisation. Table 6.6 indicates the settings that all

these six models share.
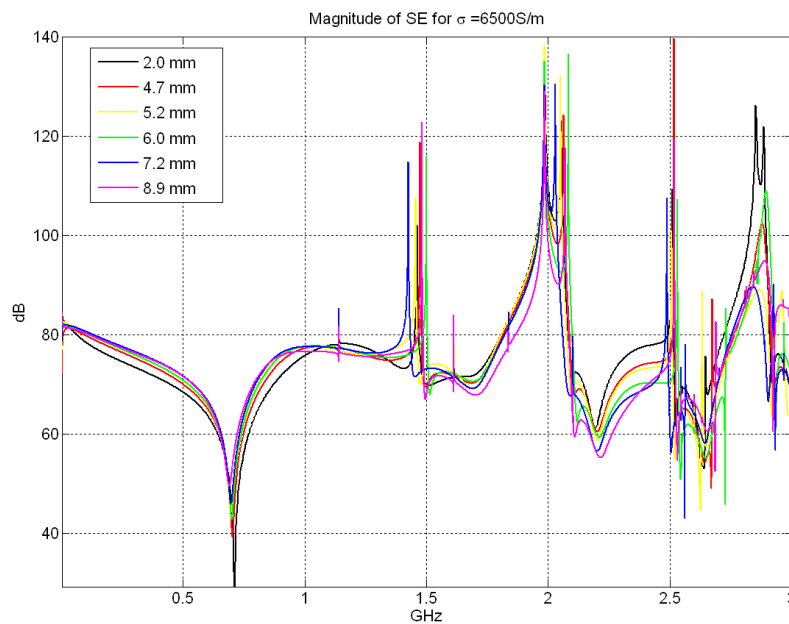
Figure 6.15. The shielding effectiveness of 78mm-by-78mm panel simulated using six values of mesh size (dl). The conductivity is 6500 S/m.

Parameter	Shared settings
NT	131072
Excitation signal	Gaussian pulse at z
Number of poles	NPr=5 ; NPt=6
σ (S/m)	6500
L_d (mm)	0.5
ε_r	5

Table 6.6. The simulation settings that produced Figure 6.15.

This slight difference in the SE is a sacrifice of savings in the computation effort in terms of memory and time. It is clear from Table 6.7 that it is possible (for this setup) to reduce the run time to less than 10 per cent if a space step of 6mm is used instead of 2mm.

dl (mm)	Elapsed time scaled by the finest run
8.9	4.6%
7.2	6.2%
6.0	8.6%
5.2	11.6%
4.7	14.3%
2.0	100.0%

Table 6.7. The elapsed time for the different space resolutions used to study the effect of space resolution.

6.4.4 The Two-Phase Observation

Throughout the series of simulation that were undertaken in this study, a number of observations have been made. This section will discuss a case that occurred when modelling a three-dimensional conducting box with one face replaced with a dielectric panel. With the absence of aperture effect, the main trend of shielding effectiveness (SE) starts with a positive value in dBs and increases with frequency as shown in Figure 6.16(a). This section is related to the case when SE behaviour is split into two different states or "phases". The first one takes aperture-like

behaviour with almost no variations then drops down in the SE in a sudden decrease to start the second phase. The second phase represents a diffusion-like behaviour which increases with frequency as illustrated in Figure 6.16(b). In this study, the frequency at which the two phases (behaviours) meet will be referred to as the *split frequency*, or f_{sp}. Notice that Figure 6.16 represents only the general trend so it does not show the resonant frequencies.
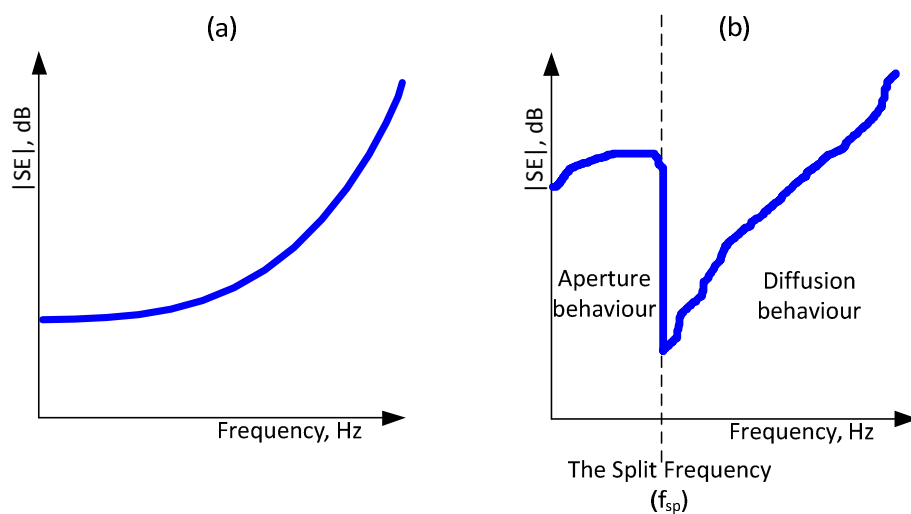
Figure 6.16. The general trend of the magnitude of shielding effectiveness in dBs against frequency for: (a) a typical case and (b) a case of the two-phase observation.

The base model for this observation is shown in Figure 6.17, which is a conductive box with one of its faces replaced with a dielectric panel of dimension of 300mm by 150mm. The excitation point is located inside the box near one of its corners. The receiving point is outside the box.

300 x 150 mm^2
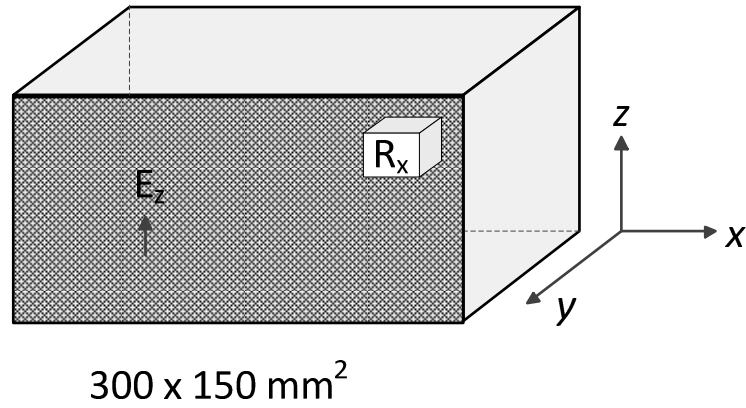
Figure 6.17. The geometry that shows the two-phase observation. Here, the excitation is shown in z polarisation.

6.4.4.1 The Effect of Excitation on SE components

In this section, the three components of the shielding effectiveness will be studied when changing the excitation polarisation. In rectangular coordinate, the SE can be represented by its three components given by

$$SE_x = 20 \log_{10} \left| \frac{E_{x\_ref}}{E_{x\_panel}} \right| \tag{6.9}$$

$$SE_y = 20 \log_{10} \left| \frac{E_{y\_ref}}{E_{y\_panel}} \right| \tag{6.10}$$

$$SE_z = 20 \log_{10} \left| \frac{E_{z\_ref}}{E_{z\_panel}} \right| \tag{6.11}$$

6.4.4.1.1 X-Polarised Excitation

The excitation polarisation is set with the maximum dimension of the box. The simulation settings were applied as stated in Table 6.8. Figure 6.18 demonstrates the general trend which manifests the two-phase

146

behaviour pointed to in Figure 6.16(b). The split frequency is found to be

1.5997GHz, which is the resonant frequency of TE_{011} mode.
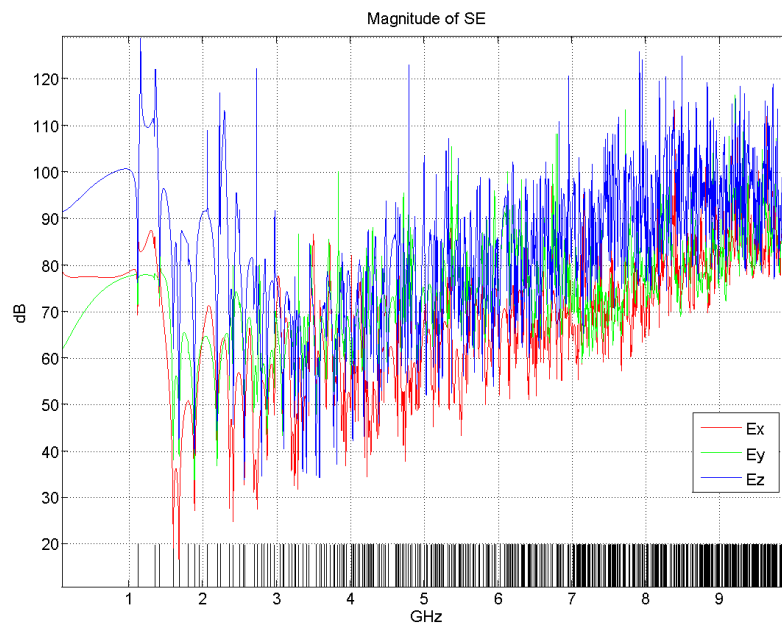
Figure 6.18. The shielding effectiveness in its three components in the x-, y-, and z-directions when the excitation electric field is linearly polarised in x direction.

By taking a close view of the first 2GHz of Figure 6.18, the three components of SE can be clearly seen in Figure 6.19. The SE_x component shows the highest change when going from the aperture phase to the diffusion phase.
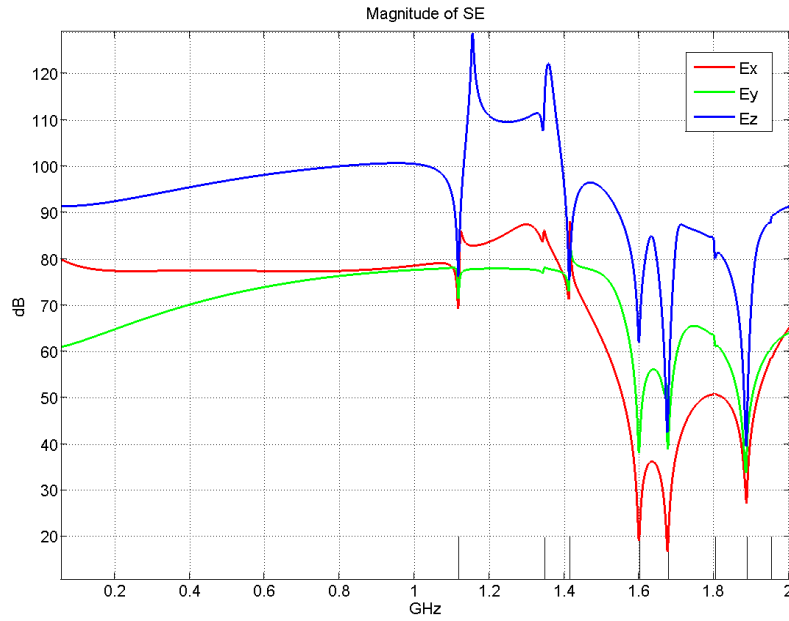
Figure 6.19. The frequencies up to 2GHz of the lower frequencies shown in Figure 6.18.

Parameter	Shared settings
NT	262144
NX.NY.NZ	100 x 40 x 50
dl (mm)	3.0
dt (ps)	5.00346
Excitation with polarisation	Gaussian pulse at x
Excitation point	(15,15,15)
σ (S/m)	Cascade 500 +1000
Number of poles	NPr=3 ; NPt=5
L_d (mm)	Cascade 1 + 1
ε_r	5 (for both)
Receiving point	(90,60,40)

Table 6.8. The simulation settings that produced Figures 6.18 and 6.19.

6.4.4.1.2 Y-Polarised Excitation

The excitation polarisation is set along with the minimum dimension of the box. The simulation settings were applied as stated in Table 6.9. Figure 6.20 demonstrates the general trend, which manifests the two-phase behaviour. The split frequency is found to be 1.1173GHz, which is the resonant frequency of TE_{101} mode.
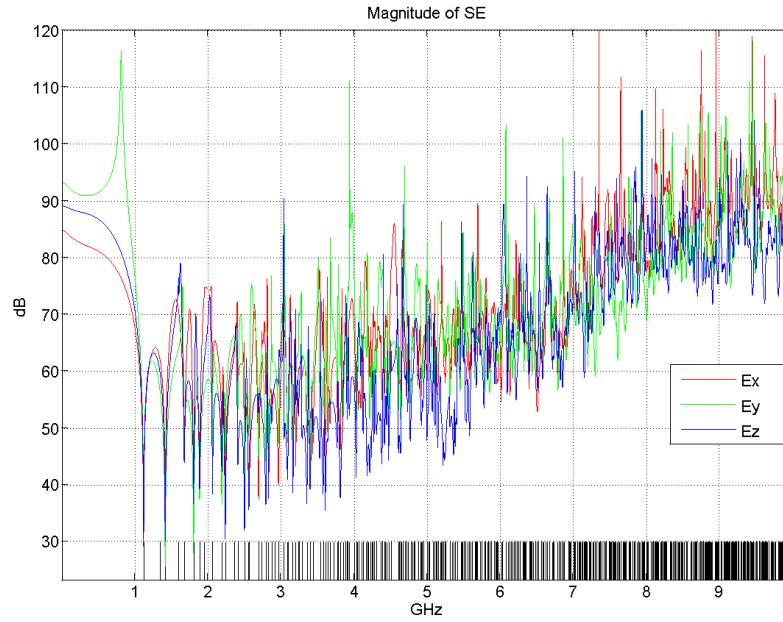
Figure 6.20. The shielding effectiveness in its three components in the x-, y-, and z-directions when the excitation electric field is linearly polarised in y direction.

Figure 6.21 shows the first 2GHz of Figure 6.20. Here, the SE$_y$ component shows the highest change when going from the aperture phase to the diffusion phase.
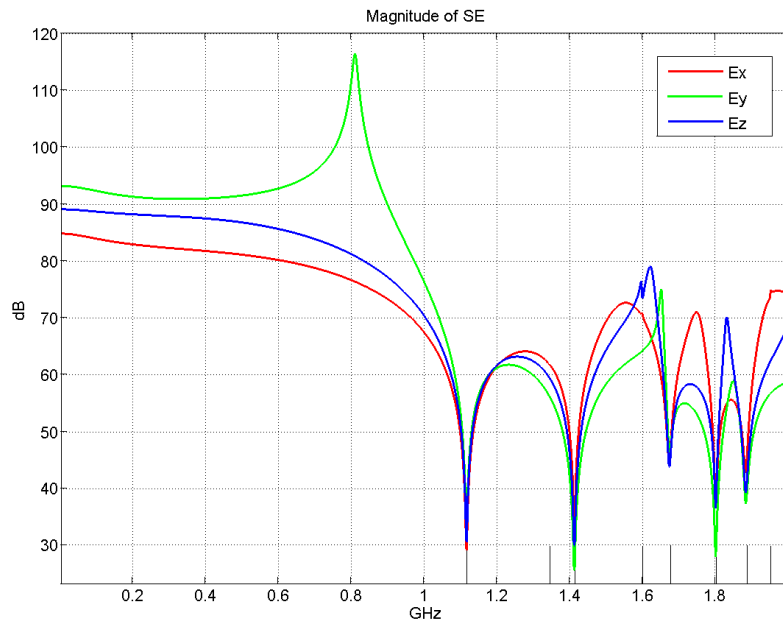
Figure 6.21. The frequencies up to 2GHz of the lower frequencies shown in Figure 6.20.

149

Parameter	Shared settings
NT	131072
NX.NY.NZ	100 x 40 x 50
dl (mm)	3.0
dt (ps)	5.00346
Excitation with polarisation	Gaussian pulse at y
Excitation point	(15,15,15)
σ (S/m)	Cascade 500 +1000
Number of poles	NPr=3 ; NPt=5
L_d (mm)	Cascade 1 + 1
ε_r	5 (for both)
Receiving point	(90,60,40)

Table 6.9. The simulation settings that produced Figures 6.20 and 6.21.

6.4.4.1.3 Z-Polarised Excitation

The simulation settings were applied as stated in Table 6.10, which differs from Table 6.8 and Table 6.9 with only the polarisation of the excitation source. Figure 6.22 demonstrates the general trend, which manifests the two-phase behaviour up to 10GHz. The split frequency is found to be 1.3454GHz, which is the resonant frequency of TE$_{110}$ mode.
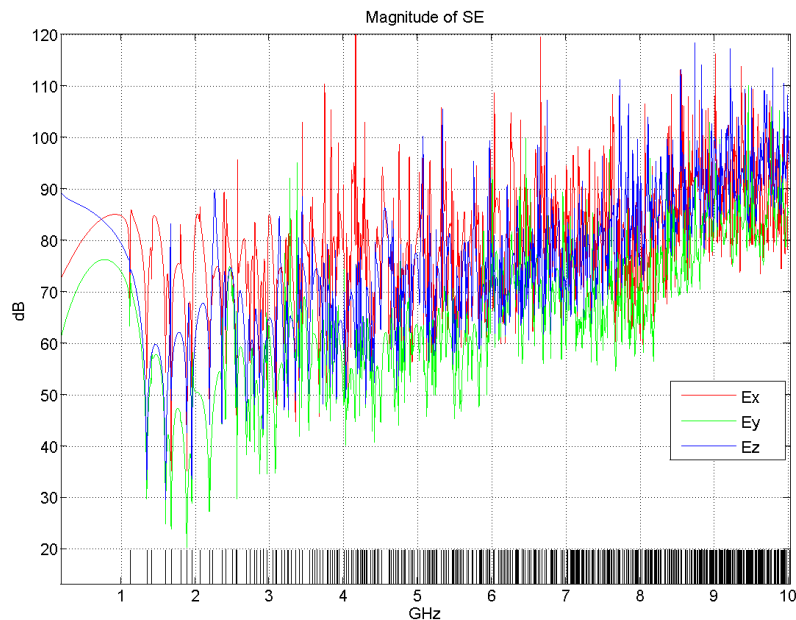
Figure 6.22. The shielding effectiveness in its three components in the x-, y-, and z-directions when the excitation electric field is linearly polarised in z direction.

Figure 6.23 shows the first 2GHz of Figure 6.20. Here, the SE$_z$ component shows the highest change when going from the aperture phase to the diffusion phase.
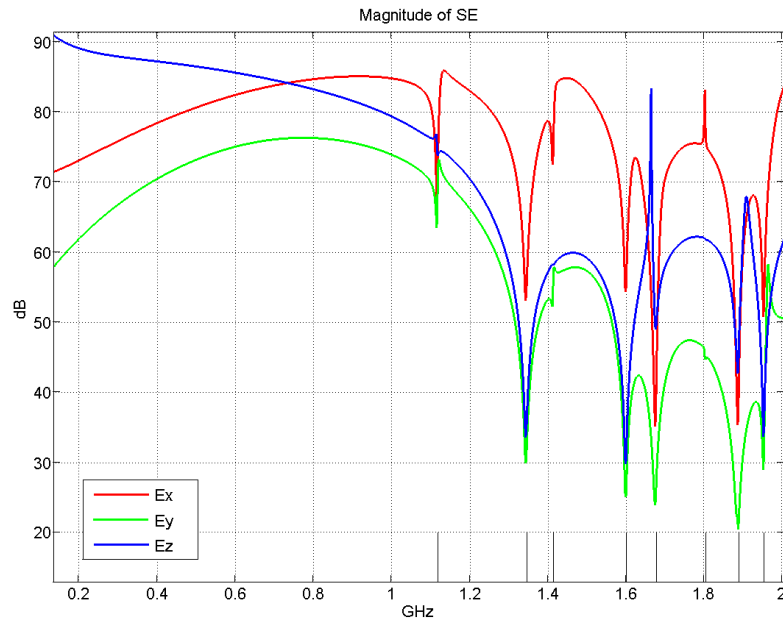
Figure 6.23. The frequencies up to 2GHz of the lower frequencies shown in Figure 6.22.

Parameter	Shared settings
NT	131072
NX.NY.NZ	100 x 40 x 50
dl (mm)	3.0
dt (ps)	5.00346
Excitation with polarisation	Gaussian pulse at z
Excitation point	(15,15,15)
σ (S/m)	Cascade 500 +1000
Number of poles	NPr=3 ; NPt=5
L_d (mm)	Cascade 1 + 1
ε_r	5 (for both)
Receiving point	(90,60,40)

Table 6.10. The simulation settings that produced Figures 6.22 and 6.23.

6.4.4.1.4 Discussion

It has been found that the split frequency (f$_{sp}$) is the frequency of mode TE$_{011}$, TE$_{101}$, and TE$_{110}$ for excitation polarised in x, y, and z respectively. This result was verified with other different setups. This observation will be discussed further in §6.4.4.4. It is found that the split

frequency value can be controlled only by the excitation polarisation regardless of the box physical size, the panel material, the excitation pulse shape, the position of the excitation point and the position of the receiving point.

6.4.4.2 The Position of the Receiving Point

In this section, shielding effectiveness will be discussed when obtained at points that are located in different positions. Instead of using one field point (as in Figure 6.17), thirty six field points have been used to find the SE. These points are arranged in a form of three-dimensional array of size 9 x 2 x 2 as shown in Figure 6.24. The field points shown in blue and red represent the points within plane y=60*dl* and y=70*dl* respectively. All these points share the settings that are stated in Table 6.11.
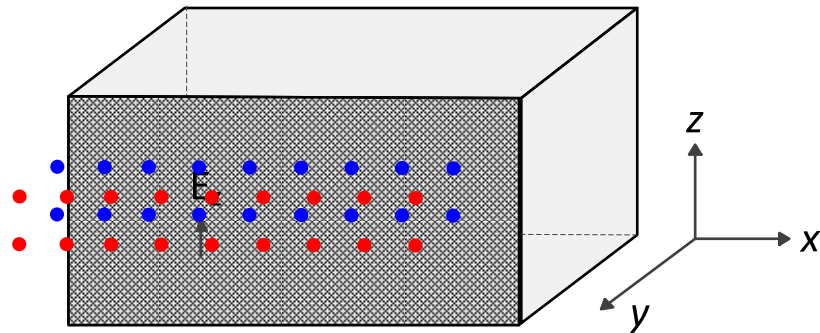
Figure 6.24. Geometry showing the positions of the 36 points that were used to measure the shielding effectiveness at.

Figure 6.25 shows the SE for the lower nine field points of the red group. The two-phase feature is still present in the SE for all these positions. Besides, it shows that at low frequencies, the SE increases when going farther from the excitation source.
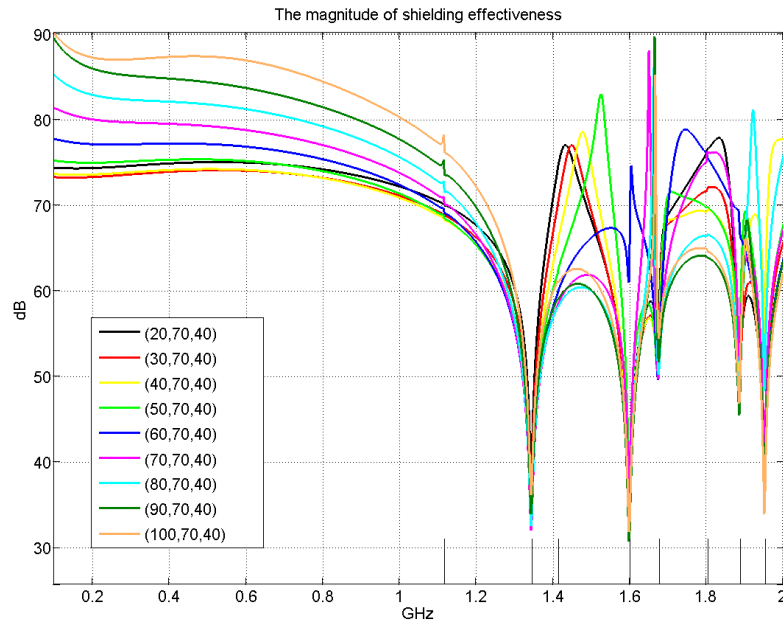
Figure 6.25. The shielding effectiveness of the line of receiving points that lies at y=70*dl*, z=40*dl*, and extends from x=20*dl* to x=100*dl*.

Parameter	Shared settings
NT	131072
NX.NY.NZ	100 x 40 x 50
dl (mm)	3.0
dt (ps)	5.00346
Excitation with polarisation	Gaussian pulse at z
Excitation point	(15,15,15)
σ (S/m)	Cascade 500 +1000
Number of poles	NPr=3; NPt=5
L_d (mm)	Cascade 1 + 1
ε_r	5 (for both)

Table 6.11. The simulation settings that produced Figures 6.25 and 6.26.

Figure 6.26 shows the contour lines of SE against x-axis distance (measured in *dl*) and frequency (measured in GHz). With this full-scale plot, one can see the gradual increase of the SE with frequency up to 10GHz. Moreover, the variation of SE with the distance in the x-axis is small in general.
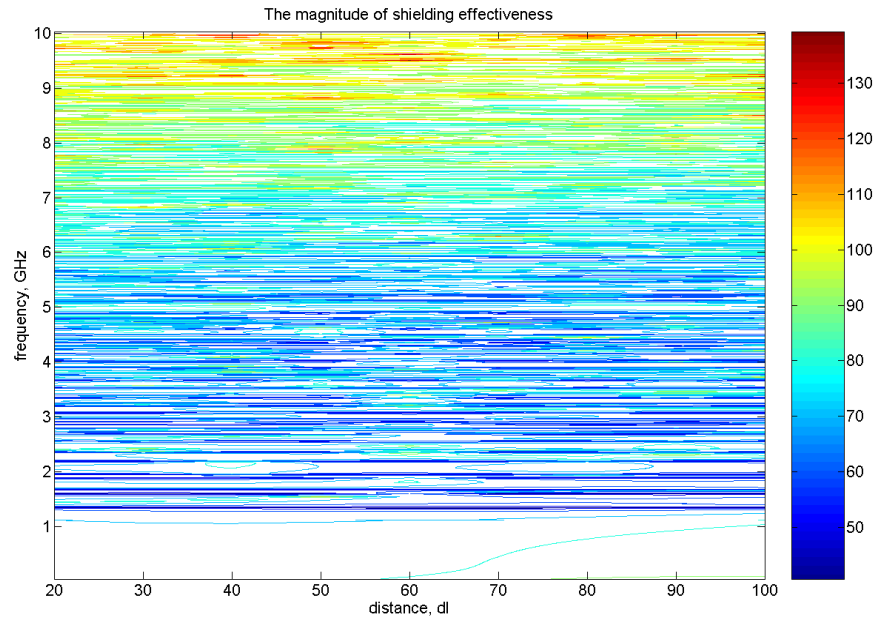
Figure 6.26. The shielding effectiveness (SE) of the line of receiving points that lies at y = 70*dl*, z = 40*dl*, and extends from x = 20*dl* to x = 100*dl*. The SE contours are plotted versus frequency and the position of the receiving point with respect to the origin point of the object geometry. The SE is plotted in dB.

6.4.4.3 Face-Current Distribution

In an attempt to understand the SE pattern, the surface currents have been plotted on the outside face of the panel. Surface current can be evaluated from the knowledge of the magnetic field as [6.6]

$$\bar{J} = \hat{n} \times \bar{H} \qquad (6.12)$$

where $\bar{J}$ is the current density vector in A/m^2, $\hat{n}$ is a unit vector normal and outwardly directed from the cavity walls, and $\bar{H}$ is the magnetic field intensity vector in A/m.

The next three figures show the surface current on the panel face for three different frequencies. The shared settings for the three cases are indicated in Table 6.12. The surface current vector-field is represented by line segments with their length represents the strength of the field. They are pointing towards the direction of the surface current that can be

154

found from equation (6.12). For clarity, the arrows of these line segments are not shown. However, the direction is towards increasing x and decreasing z.

Parameter	Shared settings
NT	131072
NX.NY.NZ	100 x 40 x 50
dl (mm)	3.0
dt (ps)	5.00346
Excitation with polarisation	Sinusoidal at y
Excitation point	(15,15,15)
σ (S/m)	Cascade 500 +1000
Number of poles	NPr=3 ; NPt=5
L_d (mm)	Cascade 1 + 1
ε_r	5 (for both)
Receiving points	Panel face (99 x 0 x 49)

Table 6.12. The simulation settings that produced Figures 6.27, 6.28, and 6.29.

6.4.4.3.1 Frequency is higher than Split Frequency

The frequency for the first case (illustrated in Figure 6.27) was chosen such that it is higher than the split frequency relevant to the excitation wave. The highest current is directed towards increasing x and it lies between two current minima.
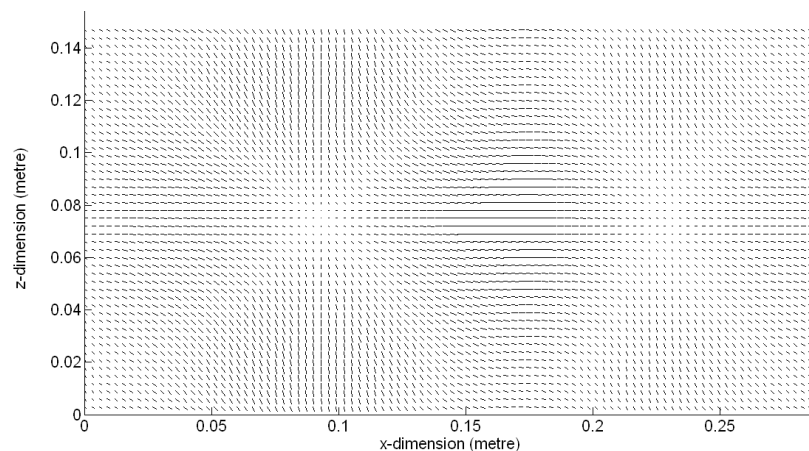
Figure 6.27. The face current distribution for the case of y-polarised sinusoidal excitation at frequency of 1.5GHz which is above the split frequency.

6.4.4.3.2 Frequency is the Split Frequency

The frequency for the second case (illustrated in Figure 6.28) is the split frequency relevant to the excitation wave. The current distribution is symmetric around the central point where a current minimum is shown. This symmetry is expected since the split frequency is the resonant mode TE_{101}. This means that this frequency develops one half of a wavelength in both x- and z-dimension. The highest current is directed towards decreasing z and it lies at the middle value of the x dimension of the box.
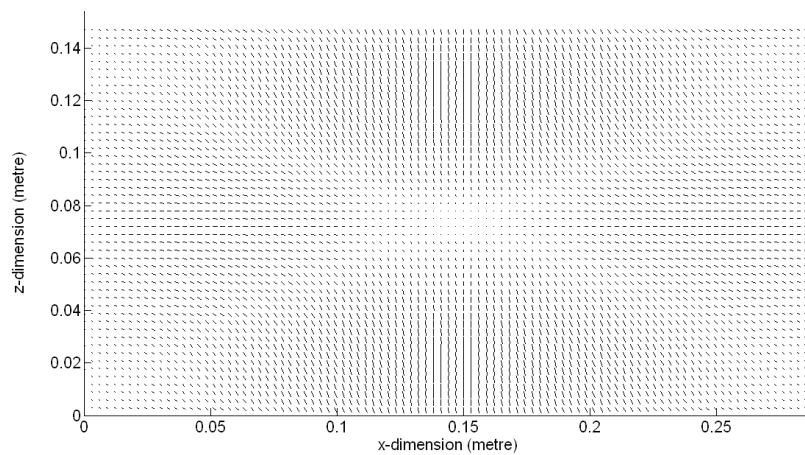
Figure 6.28. The face current distribution for the case of y-polarised sinusoidal excitation at frequency of 1.1173GHz which is the split frequency.

6.4.4.3.3 Frequency is lower than Split Frequency

The frequency for the third case (illustrated in Figure 6.29) was chosen such that it is lower than the split frequency relevant to the excitation wave. There is a current-minimum centred 8cm from the box edge nearer to the excitation. High current is found directed towards decreasing z and it lies at 7.5cm distance from the box edge that is nearer to the excitation point. High current can also be observed, which is directed towards increasing x at 6cm in z dimension.

156
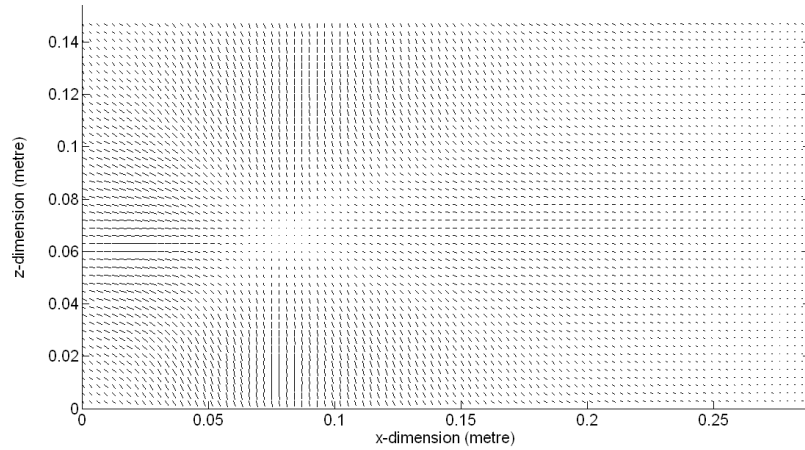
Figure 6.29. The face current distribution for the case of y-polarised sinusoidal excitation at frequency of 0.7GHz which is below the split frequency.

6.4.4.4 The Panel Thickness to the Cavity Dimension

In a further attempt to find the reason that triggers the two-phase case, different thickness of the panel has been applied. Figure 6.30 illustrates the geometry that was used for this purpose. The panel dimension is 30mm x 30mm. Four thicknesses have been applied which are 1mm, 0.5mm, 0.1mm, and 0.05mm. The source point is inside the box near one of its corners and the field point is outside the box.
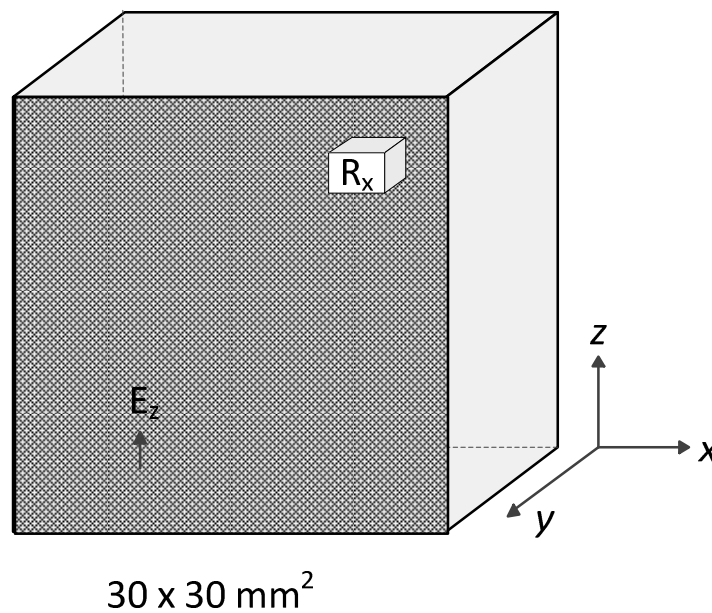
Figure 6.30. The geometry that is used to test the effect of the panel thickness on the two-phase observation.

Figure 6.31 shows the SE of the four cases of panel thickness. Being excited by z-polarised wave, the split frequency is the resonant mode TE_{110} which is 13.4536GHz. It is clear that the four curves can be viewed as shifted versions of the same SE pattern for frequencies higher than 13GHz. However, the SE for frequencies below 13GHz has a different behaviour. The differences in Phase One "the aperture behaviour" (below 13GHz) can be observed in the slope of the first rise. This slope region is represented by the first 7 GHz. It is obvious from Table 6.13 that, in general, this slope increases with increasing the panel thickness.

L_d (mm)	Slope of the first rise
1.0	17.4dB/5GHz
0.5	6.5dB/5GHz
0.1	2.1dB/5GHz
0.05	2.3dB/5GHz

Table 6.13. Comparison between the four cases of panel thickness based on the slope of the first rise.
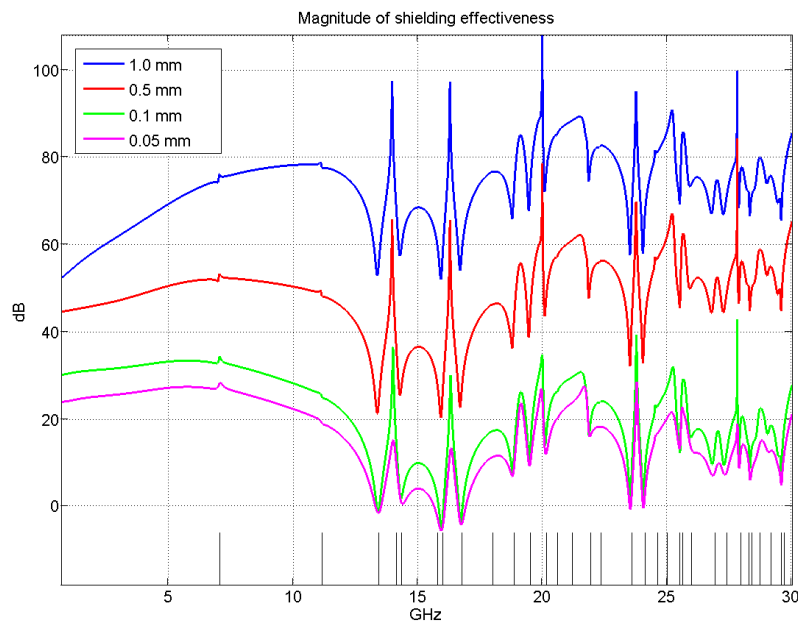
Figure 6.31. The magnitude of shielding effectiveness for four different cases of thickness for panels in the same conducting box.

Table 6.14 states the settings that these four cases share.

Parameter	Shared settings
NT	131072
NX.NY.NZ	30 x 12 x 30
dl (mm)	1.0
dt (ps)	1.66782
Excitation with polarisation	Gaussian pulse at z
Excitation point	(15,15,15)
σ (S/m)	1000
ε_r	5
Receiving point	(30,32,20)

Table 6.14. The simulation settings that produced Figure 6.31.

Table 6.15 indicates the differences in the number of poles for the designed digital filters used to model the relevant panel thickness.

L_d (mm)	NPr	NPt
1.0	3	3
0.5	3	3
0.1	1	1
0.05	1	1

Table 6.15. The number of poles for the reflection- and transmission parameters of the used digital filters with these four panel thicknesses.

From the above discussion, one can conclude that Phase One can represent aperture behaviour when the thickness of the panel is made smaller for a given cavity dimensions. By increasing the panel thickness, Phase One starts to form a continuation of the diffusion part. This is manifested by the tendency of gradual increase of the SE with frequency.

6.5 Transmission Simulation

While §6.4 is concerned with the shielding effectiveness, this section will study more directly the transmission parameter S_{21} of the S-matrix. In this way, two S_{21} curves can be obtained for each setup. One is for the panel case (referred to as $S_{21}{}^{panel}$) and the other is for the reference case (referred to as $S_{21}{}^{ref}$). They are given by

$$S_{21}^{panel}(f) = 20\log_{10}\left|\frac{2\,V_{out}^{panel}(f)}{V_S}\right| \qquad (6.13)$$

$$S_{21}^{ref}(f) = 20\log_{10}\left|\frac{2\,V_{out}^{ref}(f)}{V_S}\right| \qquad (6.14)$$

where the units are in dBs. The output voltages $V_{out}{}^{panel}$ and $V_{out}{}^{ref}$ are for the cases: with the panel and without the panel respectively. The source voltage is denoted as V_S.

This section is based on the geometry shown in Figure 6.32. This is a closed rectangular cavity of conducting walls. The dielectric material is splitting the cavity into two halves. The excitation source lies in the left-hand side and the testing point lies in the right-hand side. The source and the field point were replaced with monopoles in some stages as will be demonstrated in §6.5.2.
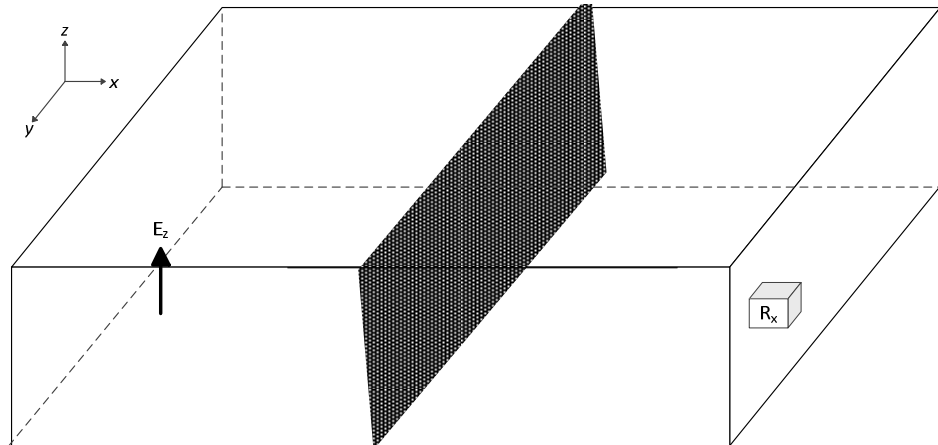
Figure 6.32. The geometry that is used to find the S_{21} parameter for different material types and monopoles.

6.5.1 The Space Resolution

When modelling panels using digital filters, the space resolution (*dl*) has a lower limit as well as an upper limit. These two limits were set in

equation (5.5) in §5.2.2 and they are restated in equation (6.3) in §6.2.1.2.1. According to the minimum limit in this equation, better accuracy can be achieved when the space resolution (dl) is set to be at least five times larger than the panel thickness.

Figures 6.33 and 6.34 show the case of modelling a panel of thickness 0.5mm using two values of space step (dl).

1) $dl = 2L_d = 2(0.5) = 1$mm

2) $dl = 5.92405L_d = 5.92405(0.5) = 2.962025$mm

The consequences of the difference in space step are indicated in Table 6.16. Figure 6.33 represents the panel S_{21} parameter that is defined by equation (6.13). It is clear that the position of some resonant frequencies is not accurate in the case of small space step (dl=1mm). This accuracy is enhanced when going for the coarser space step (dl=2.962025mm). This result has been discussed in §3.9 with Figure 3.5.
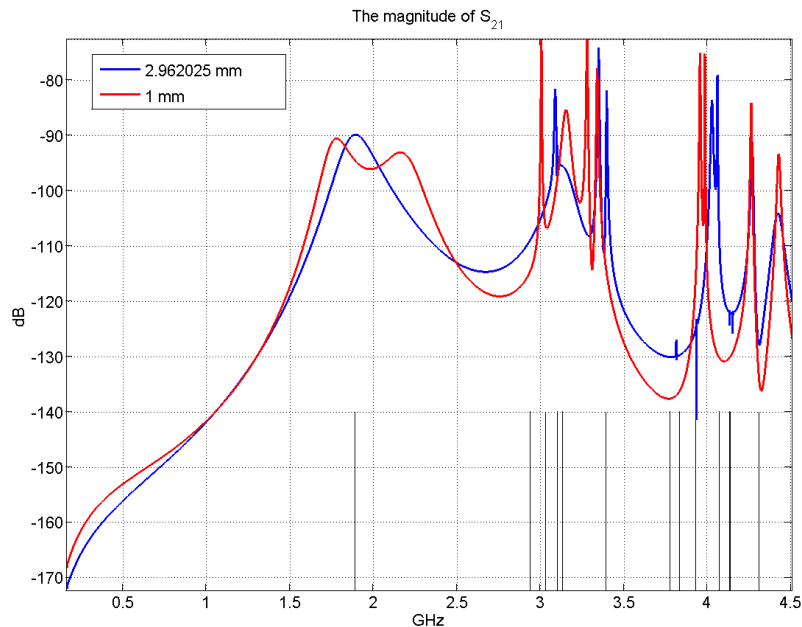
Figure 6.33. The magnitude of S_{21} parameter for the panel case of conductivity of 20k S/m showing the effect of reducing the space step beyond the recommended limit. Too small space step leads to modelling errors.

Parameter	Blue curve	Red curve
NT	1048576	524288
NX.NY.NZ	78 x 37 x 18	234 x 109 x 55
dl (mm)	2.962025	1.0
dt (ps)	4.94013	1.66782
Excitation with polarisation	Gaussian pulse at z	
Excitation plane	3 x 3 x 1	11 x 11 x 1
σ (S/m)	20000	
Number of poles	NPr=6 ; NPt=9	
L_d (mm)	0.5	
ε_r	5	
Receiving point	(73,18,16)	(219,54,53)

Table 6.16. The simulation settings that produced Figures 6.33 and 6.34.

Figure 6.34 represents the reference S_{21} parameter that is defined by equation (6.14). As with the panel S_{21}, the representation of some resonant frequencies is not as accurate as in the case of coarser space step.
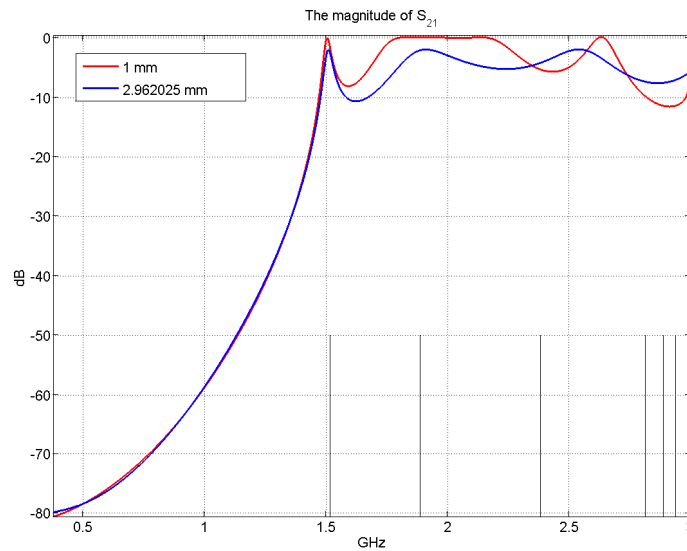
Figure 6.34 The magnitude of S_{21} parameter (without the presence of the panel) showing the effect of reducing the space step beyond the recommended limit.

6.5.2 The Effect of Monopoles

In this section, the geometry of Figure 6.32 will be used to get the reference S_{21} (no panel) with different configurations for the transmitting and receiving monopoles. The purpose of this section is to investigate the effects of changing the configuration of the transmitting and

receiving antennas. The settings that are stated in Table 6.17 were applied on the models in this section. Figure 6.35 represents the case when the transmitting element is identical to the receiving element. This figure shows the effect when replacing the isotropic point source and the field point by wire monopoles of different lengths. There are three effects for changing the monopole length.

1) *The amplitude of the resonant frequency peaks*. These amplitudes are close to zero dB when using monopoles while they are lower in the case of the point source/receiving points.

2) *The difference between the peaks and troughs*. This difference is smaller when the wire monopole is longer.

3) *The resonant frequencies*. Their representation gets some error from the analytic values, which are shown as vertical lines. This error increases noticeably with using longer monopoles. Moreover, this error increases more noticeably with higher frequencies.
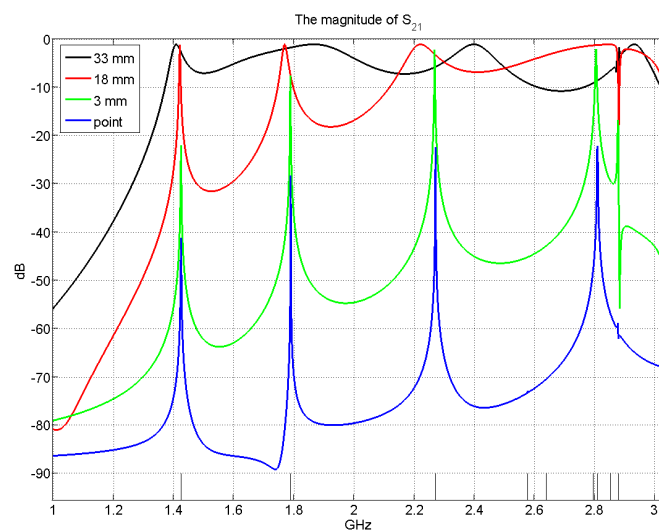
Figure 6.35. The magnitude of *S$_{21}$* for three different lengths of wire monopoles compared with the case of point source/receiving field point. All curves represent the reference case, i.e., without the presence of the panel.

Parameter	Shared settings
NT	131072
NX.NY.NZ	80 x 39 x 20
dl (mm)	3.0
dt (ps)	5.00346
Excitation with polarisation	Gaussian pulse at z

Table 6.17. The simulation settings that produced Figures 6.35, 6.36, 6.37, 6.38, 6.39, and 6.40.

Effects number two and number three are also applicable when using volume (thick) monopoles as it is the case with Figure 6.36. Instead of wire monopoles, a volume monopole with a cross-sectional area of 3*dl* by 3*dl* is used here, where *dl* = 3mm.
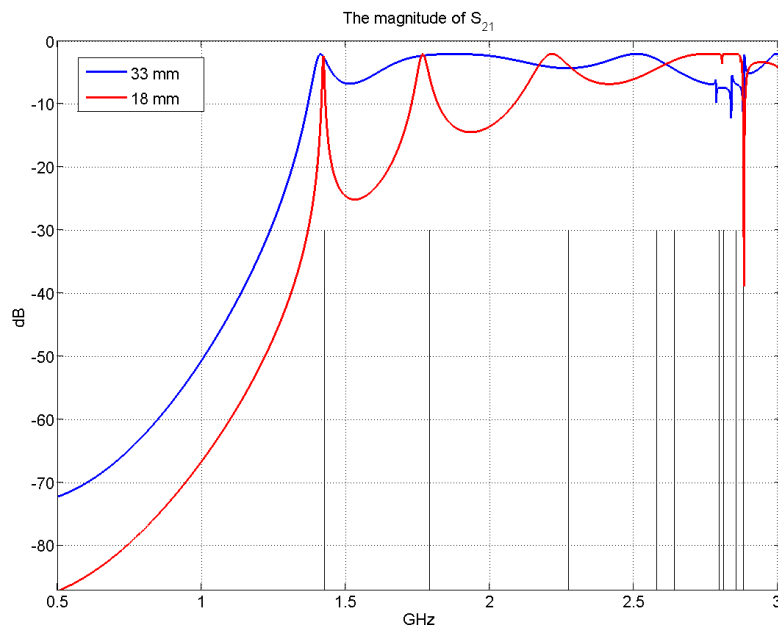
Figure 6.36. The magnitude of S_{21} (without the presence of the panel) for two different lengths of thick monopoles.

Figure 6.37 compares between the cases of the wire monopole and that of the volume monopole of the same length. It can be seen that the wire monopole produces more accurate result in terms of the resonant frequencies.
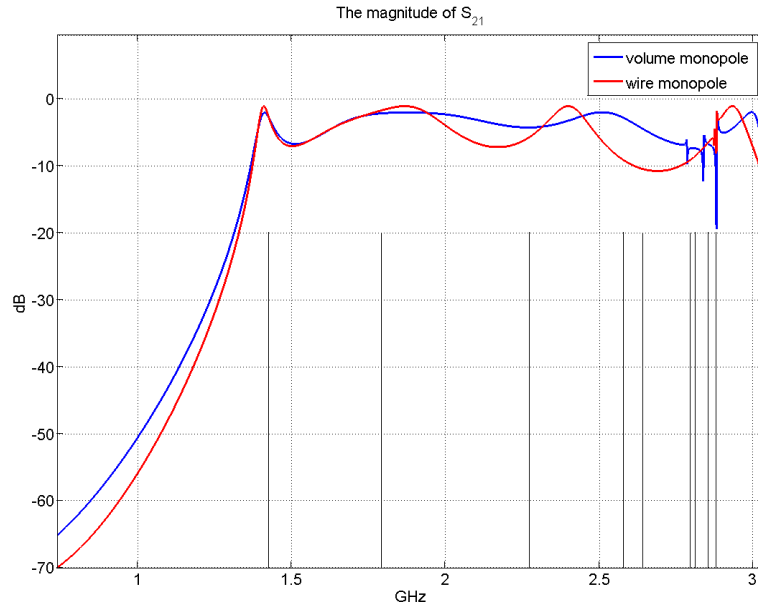
Figure 6.37. The magnitude of S_{21} (without the presence of the panel) for two 33-mm monopoles. One is wire monopole and the other has a cross section of 9mm-by-9mm.

Figure 6.38 shows the case when the transmitting and receiving elements are not identical. It shows the effect when swapping the transmitting wire monopole with the receiving field point. One case seems like a shifted version of the other. The difference between the two curves is in terms of 111dB.
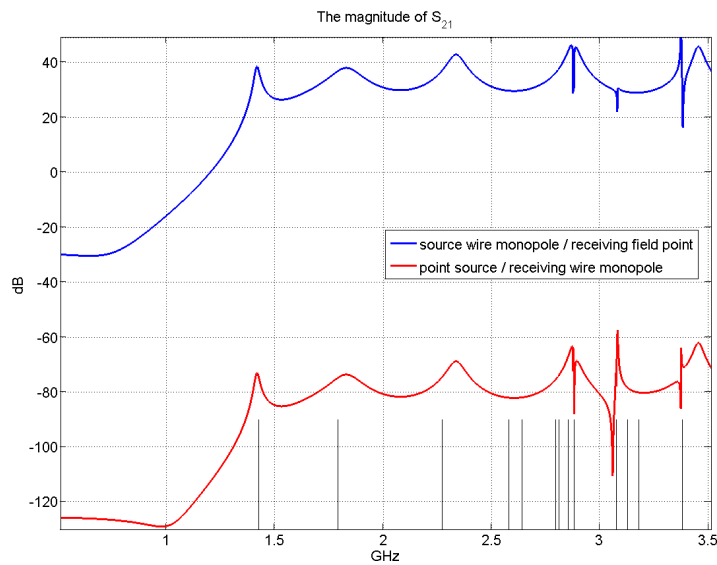
Figure 6.38. The magnitude of S_{21} for two cases of different excitation antennas and different receiving antennas. This was obtained by interchanging an isotropic antenna with a wire monopole in the reference case.

165

Figure 6.39 demonstrates the case when changing the position of the volume monopoles inside the cavity by one or two space steps (*dl*). Three trials of different monopole positions are simulated such that the three of them keep the distance between the two monopoles fixed. As a result, the S_{21} curve for the three setups is almost the same. However, there is a small difference from the original setup (called "reference" in Figure 6.39) between 1.5GHz and 1.7GHz.
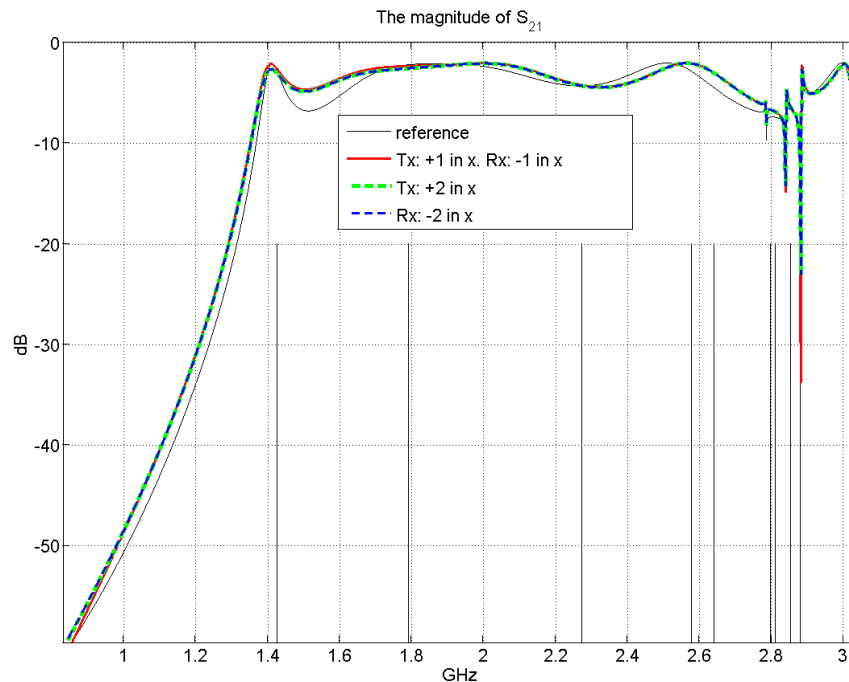
Figure 6.39. The magnitude of S_{21} (without the presence of the panel) showing the effect of changing the positions of the two volume monopoles in *x* dimension while keeping the distance between them fixed as in the reference case.

Figure 6.40 shows other setups of relocating the positions of the two monopoles, however, this time the monopoles are shifted in y dimension as well. The conclusion here is that unless the monopole is shifted in both *x* and *y*, the effect of this relocation on the S_{21} is negligible. The S_{21} curve is not sensitive to a change of monopoles by one or two space step.
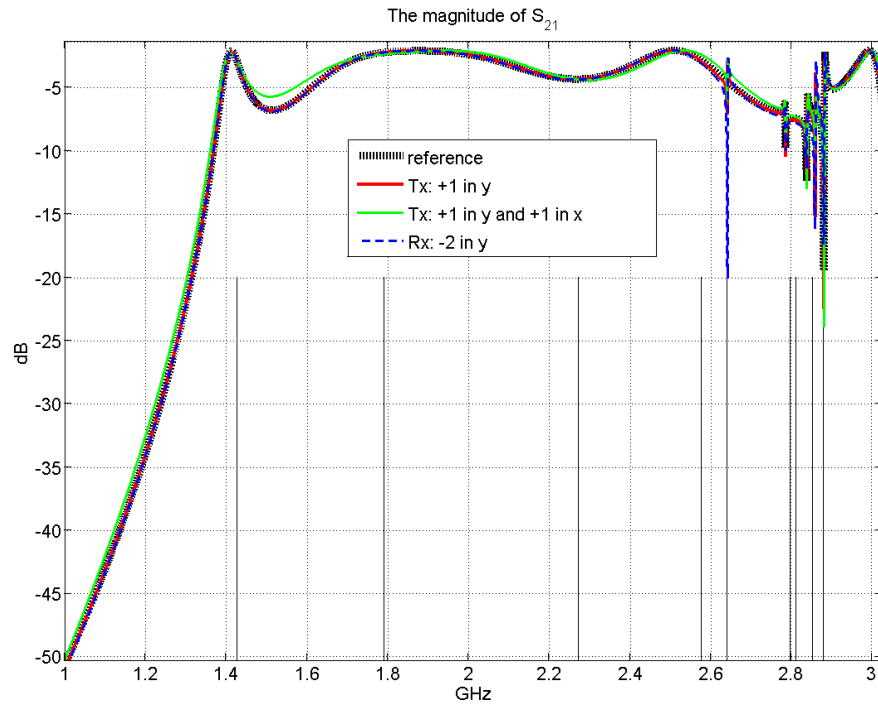
Figure 6.40. The magnitude of S_{21} (without the presence of the panel) showing the effect of changing the positions of the two volume monopoles in *x* and *y* dimensions.

The summary of what has been discussed in this section is that three forms of antennas (isotropic, wire monopole, and volume monopole) were used as transmitting and receiving antennas to investigate their effects on the final S_{21} pattern. The slight change of the antenna position was also modelled by shifting the antenna position in *x*- and *y*-direction. It was shown that in general the volume monopole has less sharp features in the S_{21} pattern. This is due to its Q factor which is lower than that of wire monopole. Also, it was noticed that the same effect of less sharp features can occur when using longer monopoles even if they are wire monopoles. Moreover, it was observed that by using longer monopole, high resonant-frequencies are shifted to frequencies which are higher than their analytic frequencies. The importance of the results in this section is to get a sufficient confidence when modelling the real

setup that was used in the laboratory. This is because the exact modelling of the real monopoles (in terms of size and position) is not always possible when applying a coarse space step (*dl*). Also, this gives an idea of the effect of replacing the ideal isotropic antennas with practical monopoles and thus may explain the differences observed between measurements and simulations.

6.5.3 The Effect of Panel Material

Using the same geometry in Figure 6.32, panels with different material conductivities were modelled. The relevant *S$_{21}$* curves are shown in Figure 6.41. The vertical lines represent the resonant frequencies of this model. These resonant frequencies are corresponding to a cavity that has half the volume of the whole cavity illustrated in Figure 6.32. This is because (as mentioned in the beginning of §6.5) this panel halves the cavity into two identical cavities. To understand Figure 6.41, equation (6.13) needs to be revisited. For a given source voltage, the higher the conductivity is, the weaker (lower) the output voltage at the receiving monopole and hence the smaller the value of the S$_{21}$ parameter. Based on this, Figure 6.41 can be analysed as follows. Increasing the material conductivity of the panel does not affect the main features. However, it is clear that the smaller the conductivity is, the closer the behaviour will be to a "free-space-like window" and hence the closer the behaviour to mimic an aperture. This pattern is manifested in the lower conductivity curves, where the *S$_{21}$* curves fluctuate around a rather constant value. On the other hand, when using higher values of conductivity, we notice a

gradual deviation from the low-conductivity curves. This diversion increases with frequency. This is demonstrated in Figure 6.41 by 25.3dB difference at 1GHz against 69.1dB difference at 10GHz when checking the difference between the 5k S/m curve and the 20k S/m curve.
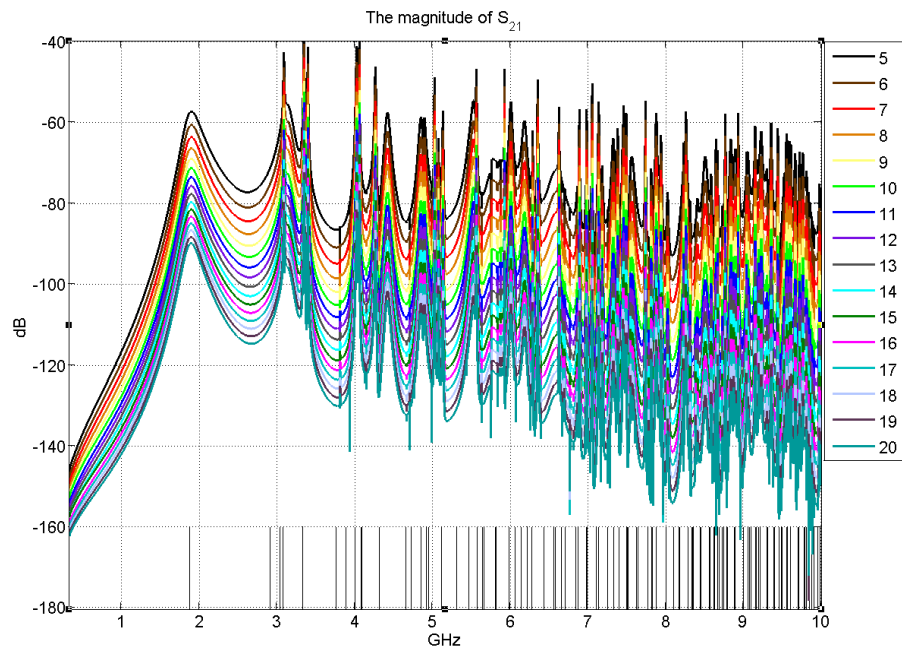
Figure 6.41. The transmission s-parameter for a material with sixteen different conductivities that ranges from 5k S/m to 20k S/m.

Figure 6.42 shows the lower frequency part of Figure 6.41. It can be seen sometimes, that by changing the position of the source, we start to see some new resonant frequencies. However, this is not the situation here where the material conductivity is changed.
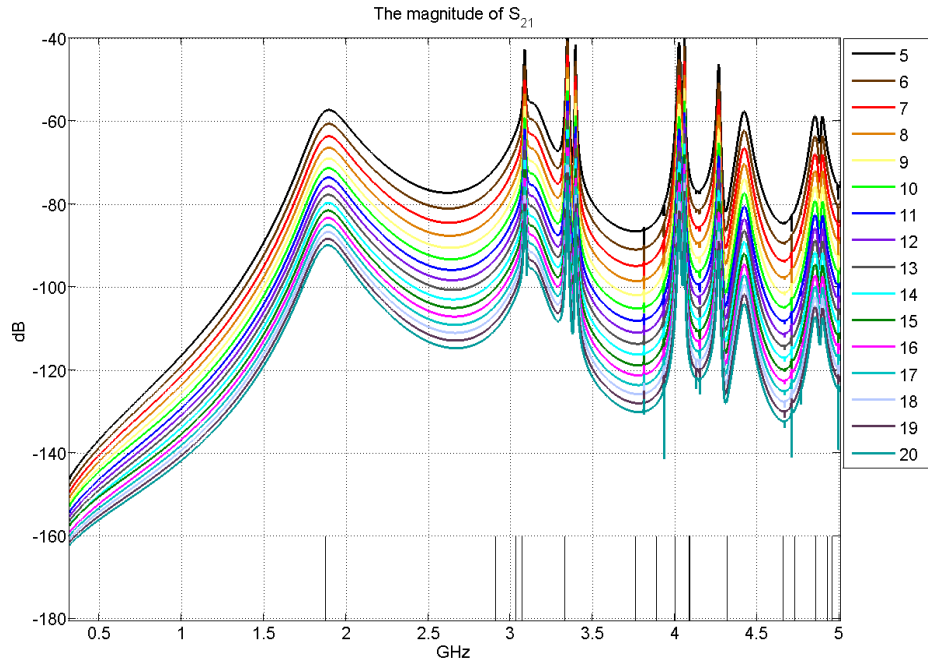
Figure 6.42. The first 5GHz of Figure 6.41 Shown above.

Table 6.18 indicates the shared simulation parameters for the sixteen models, while Table 6.19 states the differences of the number of poles that were used in designing the relevant digital filters.

Parameter	Shared settings
NT	1048576
NX.NY.NZ	78 x 37 x 18
dl (mm)	2.962025
dt (ps)	4.94013
Excitation with polarisation	Gaussian pulse at *z*
Excitation plane	3 x 3 x 1
L_d (mm)	0.5
ε_r	5
Receiving point	(73,18,16)

Table 6.18. The simulation settings that produced Figures 6.41 and 6.42.

σ (kS/m)	5	6	7	8	9	10	11	12	13	14	15	16	17	18	19	20
NPr	4	5	5	6	5	6	6	6	6	6	6	6	6	6	6	6
NPt	5	6	6	6	6	7	7	7	7	7	8	8	8	9	9	9

Table 6.19. The number of poles for the reflection- and transmission-coefficients used to design the digital filters of the above-mentioned conductivities.

170

6.6 Summary

This chapter has presented some representative results of the simulation work that took place in this study. It explained the setting of the simulation parameters. The post-processing aspects are clarified in terms of getting the right frequency range and finding the resonant frequencies. Results started by the verification of the coarse mesh/digital filter model with the conventional fine mesh. The rest of the results are divided mainly into two cases. The first is modelling the shielding effectiveness where the effect of a number of parameters has been investigated along with noticeable features. The second case is modelling a transmission through a panel that lies inside a closed cavity. The effect of setup parameters has been explained using some sample results. Some of the practical issues concerned with modelling and measurement were also discussed as they affect comparisons.

References

[6.1] J.D. Paul, C. Christopoulos, and D.W.P. Thomas, *A 3-D Time-Domain TLM Electromagnetic Field Solver: regSolvel*. University of Nottingham, Nottingham, 2008.

[6.2] MathWorks Matlab version 7.0.0.19920 (R14), produced in May, 6 2004. http://www.mathworks.co.uk/products/matlab/

[6.3] J.L. Herring, *Developments in the Transmission-Line Modelling Method for Electromagnetic Compatibility Studies*. PhD thesis, The University of Nottingham, Nottingham, 1993 (section 4.2).

[6.4] S.Y. Liao, *Microwave Devices and Circuits*. Prentice-Hall, N.J., 3rd ed., 1990.

[6.5] D.K. Cheng, *Fundamentals of Engineering Electromagnetics*. Addison-Wesley, Reading, 1993.

[6.6] J. Helszajn, *Microwave Engineering: Passive, Active and Non-reciprocal Circuits*. McGraw-Hill, London, 1992.

7

Experimental Results

This chapter is dedicated to presenting the results that were obtained using laboratory setups in an attempt to validate the simulation results that are presented in Chapter 6. At the beginning, a brief review of the main methods of measurements is presented.

7.1 Introduction

Experimental work is necessary for verifying the models that were derived by simulation work. This kind of verification is necessary to check whether any important parameters were not taken into consideration when designing the model. Throughout this study, experimental work helped in making a number of amendments to the model. Laboratory work is not without difficulties. A number of experimental setups were tried before reaching the setup that will be presented in this chapter. Laboratory work was performed in the microwave laboratory of the department of Electrical and Electronic Engineering.

7.2 Types of Measurements

Microwave techniques for material characterisation differ according to a number of factors [7.1 to 7.6]. These factors include the material parameter to be measured, the degree of accuracy, the required frequency range, the material thickness, and the conductivity of the material. Microwave methods for material characterisation can be divided into two categories.

174

1. *Resonant methods*. These are recommended whenever an accurate knowledge of dielectric properties is required at specific frequency(s).

2. *Non-resonant methods*. These are suitable to obtain a general knowledge of the electromagnetic properties over a frequency range.

Since this study is concerned with modelling materials over a frequency range then the non-resonant methods are more suitable. A closer look to the non-resonant methods reveals two sub-categories:

1. *Reflection methods*. As the name indicates, in these methods, electromagnetic waves are directed towards the material and the properties of this material are deduced from the reflection coefficient. This means that no transmission is involved here.

2. *Transmission/reflection methods*. In these methods, the material is inserted in a piece of transmission line and the properties of the material are deduced by the reflection from the material and the transmission through the material.

The latter method is the closest to this study. Reference [7.2] has discussed four types under the transmission/reflection methods. These types are stated as follows.

1. *Coaxial air-line method*. This method requires a toroidal-shaped sample material to be inserted between the inner and outer conductors of a coaxial line. This method can cover a wide range of frequencies. However, the material sample needs to be fabricated in a way that it fits into the coaxial structure. This

process should be precise to avoid air gaps that can cause large uncertainties in the measurement results.

2. *Hollow metallic waveguide method*. This method utilises a rectangular or circular metallic waveguide. With the use of rectangular waveguide, material sample can be fabricated easier than the coaxial air-line method. However, it does not support a frequency range as wide as the coaxial air-line. Moreover, it has a limited use with the inhomogeneous materials. This is because of the unwanted higher-order modes that can be excited at an air dielectric interface [7.2].

3. *Surface waveguide method.* This method uses rectangular or circular dielectric waveguide. In this method, the sample transverse dimension must be greater than or equal to the transverse dimension of the waveguide.

4. *Free space method.* This method involves using two precision horn lens antennas with far-field focus ability. In this case, there is no need to reshape the sample. Moreover, since it is contact-free method, it can be used to measure samples under special conditions. Furthermore, no higher-order modes are generated.

Taking into account the availability of equipment and tools, the hollow metallic waveguide method can be regarded as the closest method to the one that was used in this study. Therefore, a brief description to this method will be presented before proceeding on with the experimental setup. The hollow-metallic waveguide method is used to find the material characteristics. In this method, the material under test is inserted

in a piece of waveguide (Figure 7.1), and the properties of the material are deduced on the basis of the reflection from the material and the transmission through the material [7.2, 7.3, 7.5].
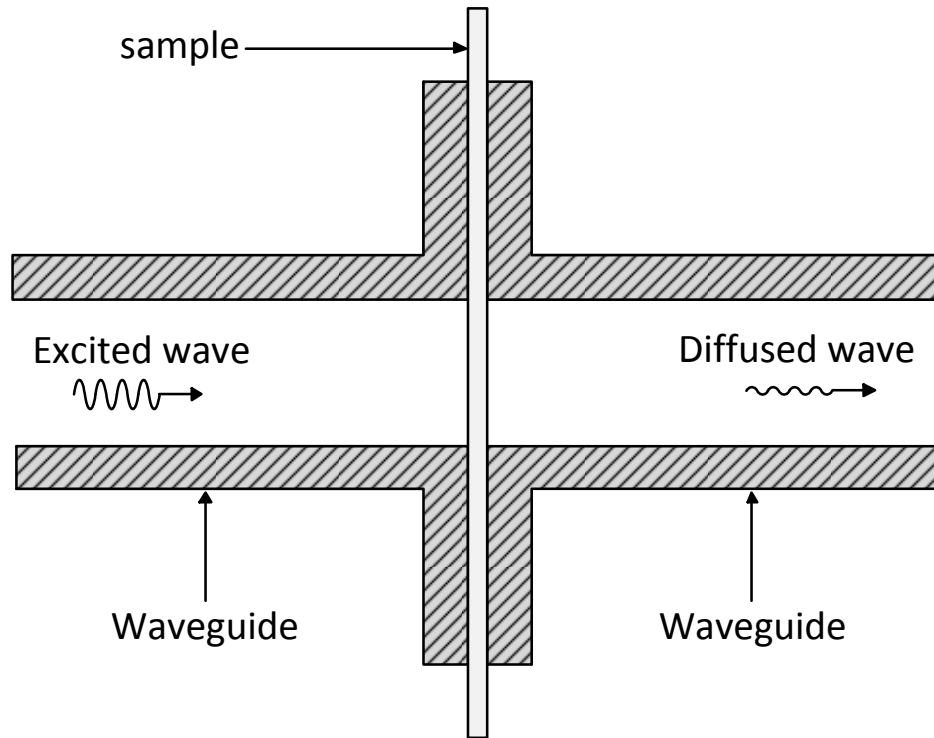
Figure 7.1. The configuration of the hollow-metallic waveguide method.

This method is widely used in the measurement of the permittivity and permeability of low conductivity materials, and it can also be used in the measurement of the surface impedance of high-conductivity materials.

7.3 Experimental Setup

The nearest standard to this configuration is the ASTM D4935 [7.7]. The setup was built using two identical waveguide-to-coaxial transitions (Figure 7.2) with the material sample inserted in between of them.

177

Figure 7.2. A waveguide-to-coaxial transition. Two identical transitions of this kind were used to insert the panel in between for this experiment.

This transition is of band W with inner dimensions of the following. The length is 117mm. Regarding its waveguide side, the width (a) and the height (b) are 109.22mm and 54.61mm respectively. The complete setup with the inserted panel is shown in the schematic of Figure 7.3.

The configuration shown in Figure 7.3 can be looked at as the equivalent electrical circuit in Figure 7.4. The transmitting antenna is a wire monopole with 50-Ohm impedance. The transmitting monopole is derived by a source voltage (V_S) generating a source current (I_S). The input voltage (V_i) is the voltage across the transmitting monopole. The receiving antenna is also a monopole with 50-Ohm impedance that generate a received current (I_R) upon receiving the excited pulse. The output voltage (V_o) is found as $50I_R$.
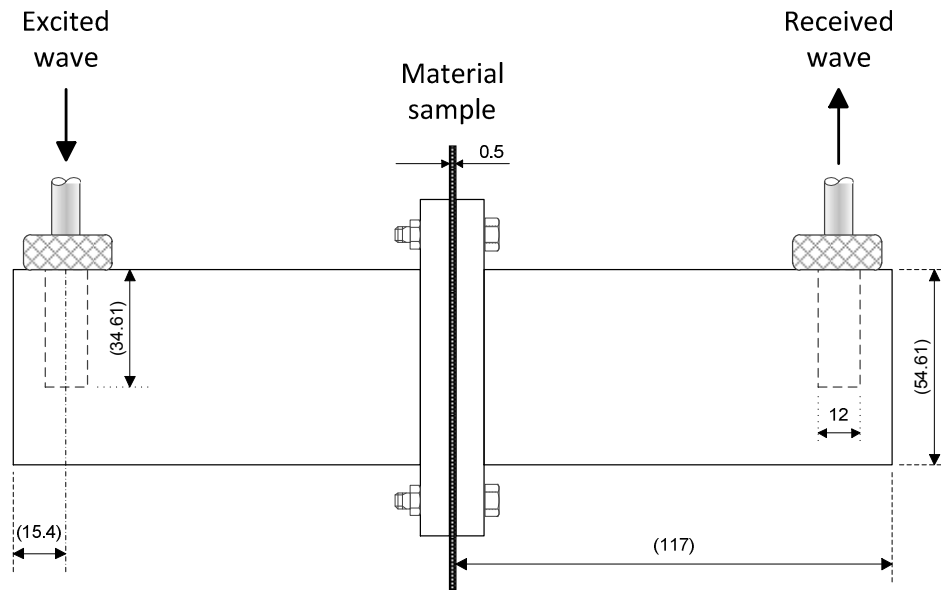
Figure 7.3. Side view of the setup that was used to verify the S_{21} simulation. The material sample is shown inserted between the two waveguide-to-coaxial transitions. Dimensions stated between parentheses are inner dimensions. All dimensions are expressed in millimetres.
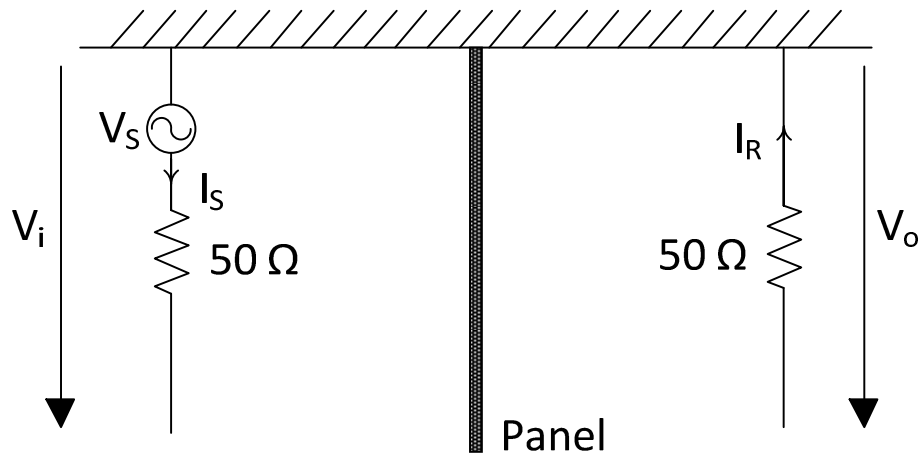
Figure 7.4. Equivalent circuit of the experimental configuration that was used in this study.

The approach that was adopted in this study has the following features when compared to the hollow metallic waveguide method.

- *Multiple-mode support*. The experimental setup in this study can

  work with multiple modes with multiple polarisations, while the

179

hollow metallic waveguide is designed to work with single polarisation. Multiple mode coupling was discussed in a number of studies [7.8 to 7.10]. This feature can omit the undesirable effect of the unwanted higher-order modes that are excited at the air-dielectric interface. Being not sensitive to the change of polarisation, our method can be used for inhomogeneous materials and is perhaps a more thorough test of material response.

- *Wider frequency range*. To ensure the single-mode requirement in the hollow metallic waveguide method, the frequency range determination should follow the following formula assuming TE_{10} mode, which is dominant mode for the rectangular waveguide.

$$a < \lambda < 2a$$

where λ is the operating wavelength and a is the inner larger dimension of the waveguide cross section. In terms of frequency limits, the minimum (cut off) frequency for TE_{10} mode is given by [7.2]

$$f_c = \frac{c}{2a} \qquad (7.1)$$

while the maximum frequency is given by [7.2]

$$f_{max} = \frac{c}{a} = 2f_c \qquad (7.2)$$

where c is the speed of light in free space which equals 2.99792458×10^8 m/s. The frequency range given by equations

(7.1) and (7.2) represent the theoretical values. To ensure good propagations, about ten per cent of frequency range next to f_c and f_{max} is not used. The experimental setup has used the waveguide under band W which has its inner larger dimension as 109.22mm. This gives a working frequency range 1.7GHz to 2.6GHz using the hollow metallic waveguide method. Our method has achieved a frequency range of 0.5GHz to 3GHz. The minimum limit was set to 0.5GHz since below this frequency, a higher amplification is required to produce a non distorted response for S_{21}.

- *Cost Implications*. Upon setting up the hollow metallic waveguide with the material sample, a specific distance (L_1 and L_2) should be assigned before and after the sample as shown in Figure 7.5. This distance is required for single mode propagation to settle down. On the other hand, our method is more general in the sense that it takes account of all generated modes. This is because we fit experimental results to a full simulation of the experiment setup; therefore we are able to account in the fitting process of all modes and other features of the configuration. In this way, this method can work with the total received wave components (reactive and real component). In this way, there is no need for the extra two waveguide sections to let the excited wave settle down.
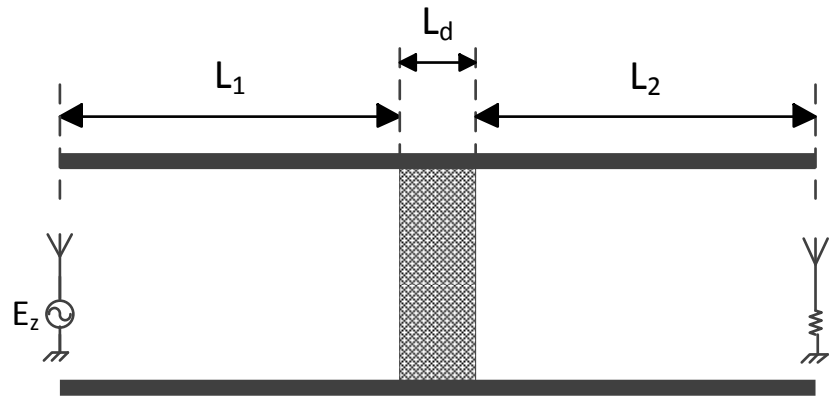
Figure 7.5. The hollow metallic waveguide structure showing the unavoidable distance $L_1 + L_2$ that should be taken into account [7.2].

- *Practical excitation*. Being more general, our method can model an excitation signal that can mimic some practical disturbance like the case when an aircraft is hit by a radar signal. In this case, real component as well as reactive component are generated. This situation cannot be modelled in the hollow metallic waveguide.

However, the hollow metallic waveguide method is more suitable if it is required to find the conductivity in a given direction inside the material, which is not the case in this study.

7.4 Measurement Procedure

An experimental configuration has been set to conduct the practical phase of this study. The apparatus that were used are stated in Table 7.1. This experiment was applied on two composite material samples. The two samples are referred to as CFC1 and CFC2.

Equipment	Description
Network Analyser	Agilent Technologies E5062A Frequency range: 300kHz – 3GHz
RF Amplifier	Amplifier Research AR25S1G4A 44dB, 25W, 800MHz – 4.2GHz
Attenuator	40dB
Waveguide-to-coaxial transition	Mega Industries standard WR430
Two different CFC Sample	Thickness = 0.5mm each

Table 7.1. List of the equipments that were used in the experiment.

To measure the S_{21} parameter for a given setup, the following procedure was followed.

1) *Cable calibration*. The network analyzer is loaded with only the cables of type N-to-N as shown in Figure 7.6. The *start* point and *stop* point of the network analyzer frequency sweep are set to the required values. Calibration can then be done by the *Calibrate* button. This step is necessary to take into account any losses that are introduced to the circuit by the insertion of the cables.

Network Analyser

N-to-N female connector
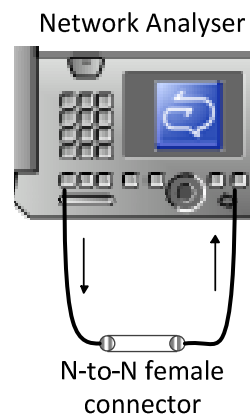
Figure 7.6. Cable calibration is the first step.

2) *Introducing the attenuator*. An attenuator set to 40dB is inserted in the wave path as shown in Figure 7.7. The

received data by the network analyzer can be saved under

the name of *att.dat*.
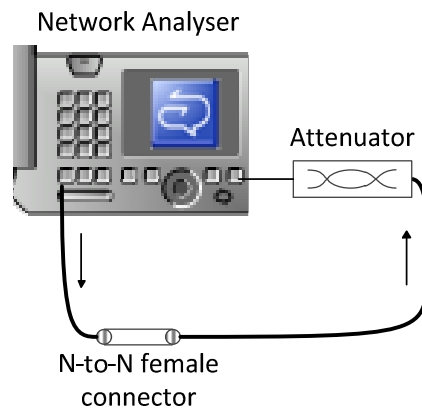
Figure 7.7. The attenuator is set to 40dB and its transmission parameter is measured.

3) *Setting the amplifier*. An RF amplifier can now be added

in the place of the N-to-N female connector as shown in

Figure 7.8. The amplifier must be switched off when

connected or disconnected. The amplifier gain should be

set such that the magnitude of S_{21} displayed by the

network analyzer shows a smooth curve, i.e., free of

distortion.
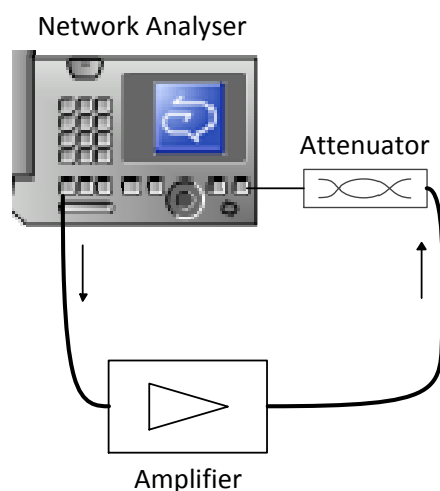
Figure 7.8. The amplifier is used to obtain distortion-free measurements.

4) *Network analyzer safety precaution.* This step is necessary to provide protection for the network analyzer especially if the power dissipation of the setup (Figure 7.3) is not known. After switching off the amplifier, the setup can be added to the circuit. This intermediate step is illustrated in Figure 7.9.
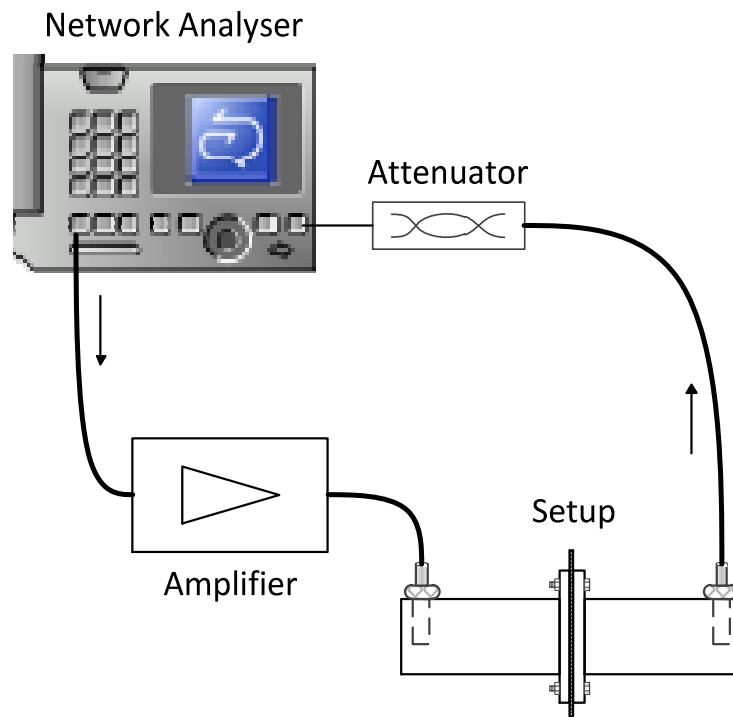
Figure 7.9. To protect the network analyzer, the setup is connected to the measurement circuit before disconnecting the attenuator.

The measured S_{21} can now be observed in the network analyzer. If the magnitude of S_{21} is showing less than the attenuator setting (40dB in this illustration), this means that removing the attenuator will not apply more than 1Watt of power on the network analyzer. This is because the maximum power rating of the network analyzer is

1Watt. On the other hand, if the magnitude of S_{21} is reading more than the attenuator setting, then the attenuator needs to be replaced with higher value of attenuation. This means repeating step number 2.

5) *Removing the attenuator*. After switching off the amplifier, the attenuator is disconnected leaving the circuit connection as shown in Figure 7.10. The received data by the network analyzer can now be saved after switching the amplifier on. The data file has the name *set.dat*.

Network Analyser
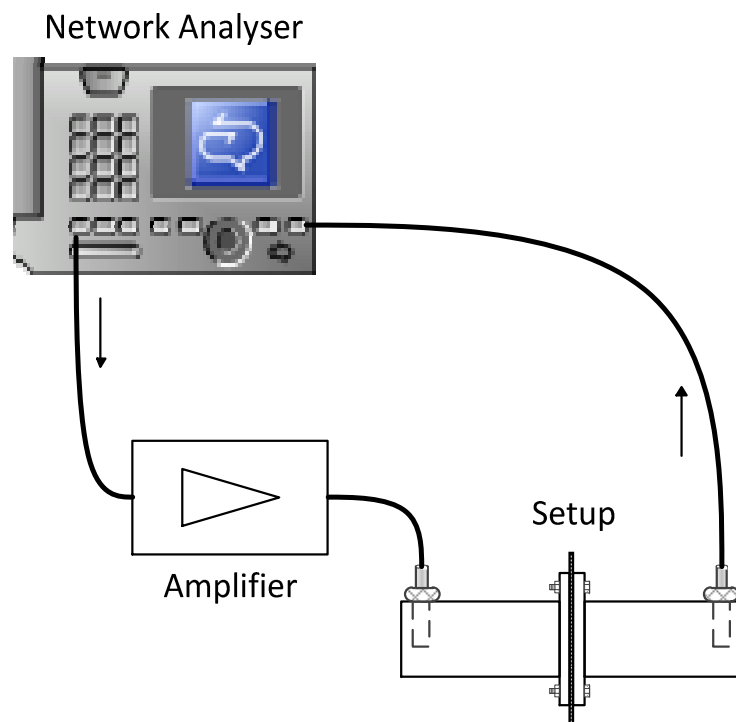
Figure 7.10. The transmission parameter of the setup can now be measured after removing the attenuator.

Over a given frequency range, two data files can be obtained from the above mentioned procedure. These steps can be repeated to cover different frequency range or to find S_{21} for different material samples. In

this study, this procedure was applied on three objects: material sample CFC1, material sample CFC2, and the third case is what will be referred to as the *empty case*. This case represents the original setup (Figure 7.3) but without the presence of the material sample. This case is important in providing a reference case which is required in comparison with the simulated reference case. Figure 7.11 shows the actual arrangement that was used in the laboratory.

Figure 7.11. The final configuration that represents Figure 7.10.

7.5 Measurement Results

The data stored in *att.dat* file represent the magnitude of S_{21} in the configuration illustrated in Figure 7.7. This means that ideally this should be a constant line at 40dB. However, practical RF attenuators have a frequency response which is not at the same magnitude over all

frequencies. That is the reason of saving this data file. In the ideal case, the magnitude of S_{21} that was measured with the object (Figure 7.10) should be shifted down by 40dB to compensate for the attenuation. In the practical case, the magnitude of S_{21} with the object can be added to the data saved as *att.dat*, which are fluctuating close to the -40dB as shown in Figure 7.12.
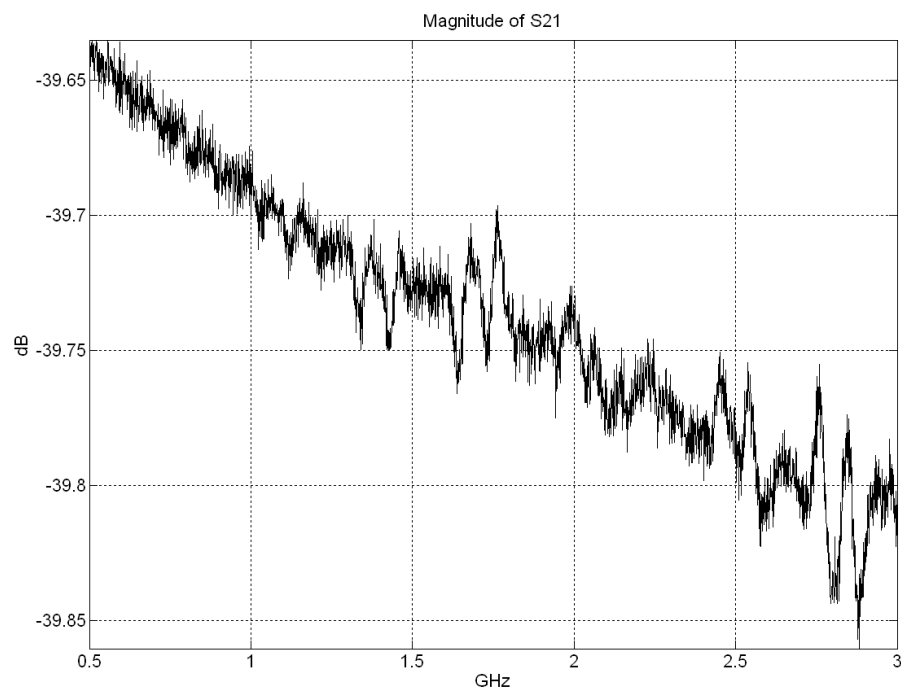
Figure 7.12. The magnitude of the S_{21} for the attenuator over the required frequency range.

It is worth mentioning that in the case of measuring S_{21} for the empty cavity object, there is no need to use the amplifier. This means there is no need for the attenuator. This is because the network analyzer signal will be propagating in free space, and thereby the excited signal will not suffer from losses. Figure 7.13 shows the magnitude of S_{21} for the three

cases: material sample CFC1, material sample CFC2, and the empty reference case.
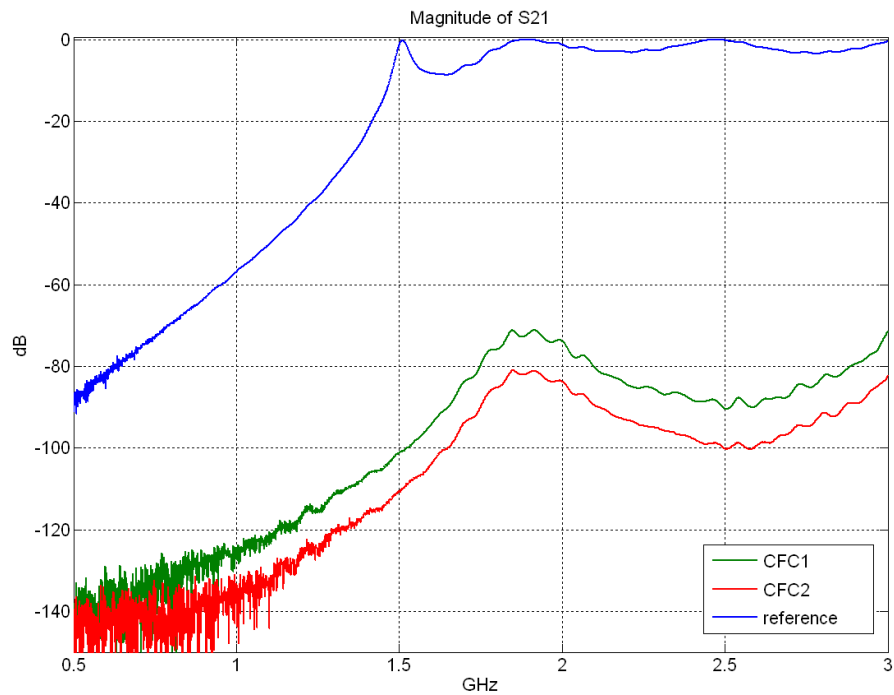
Figure 7.13. The magnitude of S_{21} for the three cases that were used in the setup shown in Figure 7.3.

Concerning the S_{21} curve in the presence of the material, it is clear from Figure 7.13 that the S_{21} curves have almost no distortion at frequencies higher than 1.3GHz. This is the result of using the RF amplifier, which has amplified the signal that was attenuated by the material panel. This case is not applicable in the setup without the material sample i.e., the empty case. As expected, the change of the material only shifts the S_{21} curve without changing its main features. The difference between the two curves is 9.69dB at the curves peaks at 1.897GHz. The peaks of the empty reference curve are -0.1951dB, -0.07778dB, and -0.1008dB at 1.51GHz, 1.897GHz, and 2.488GHz respectively.

7.6 Validation of Simulation

A model has been derived to simulate the experimental setup shown in Figure 7.3. Due to its coarse mesh (dl = 2.962025mm), the simulation did not represent the actual box precisely. Table 7.2 shows the differences between the actual setup that was used in the laboratory and the simulation model.

Dimension (all in mm)	Actual laboratory configuration	Simulated configuration	Error
Inner length (x)	234.00	231.04	1.3%
Inner width (y)	109.22	109.59	0.3%
Inner height (z)	54.61	53.32	2.4%
Panel thickness	0.50	0.50	0.0%
Monopole length	34.61	32.58	5.9%
Monopole diameter	12.00	8.89	25.9%
Monopole-to-monopole distance (centre to centre)	203.20	204.38	0.6%

Table 7.2. The differences in dimensions between the actual and the simulated model.

It was shown in Chapter 6 that the monopole thickness or diameter is not a crucial factor in determining the S_{21} behaviour. Generally, monopoles are designed with larger cross sectional area when they are supposed to work in high power applications.

Figure 7.14 illustrates the two experimental material samples with a set of simulated curves representing the magnitude of the S_{21} parameter. The simulated curves represent materials with conductivities that range from 6k S/m to 16k S/m.
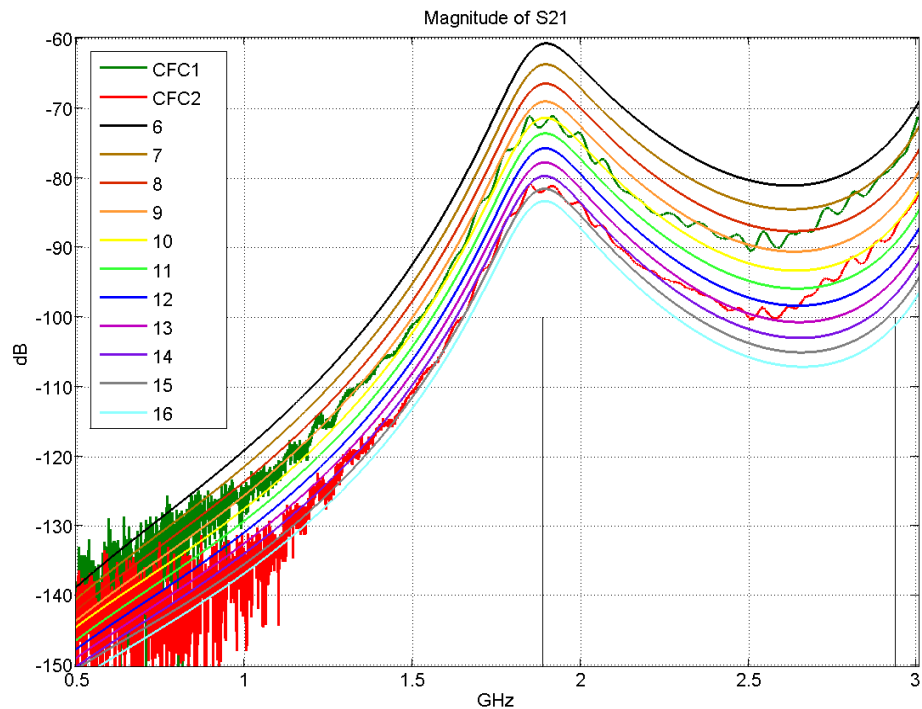
Figure 7.14. The magnitude of S_{21} for the two material samples plotted over a set of materials with conductivities that vary from 6kS/m to 16kS/m.

It can be noticed that the experimental curve does not follow only one simulation curve. This observation suggests that the properties of the composite materials used as CFC1 and CFC2 may be frequency dependent. The general behaviour is that these composite materials have lower conductivities when frequency increases [7.11].

The skin depth of the two samples CFC1 and CFC2, accordingly, will be defined over different values of conductivities. The next step is to find a piece-wise approximation that demonstrates the change of skin depth with frequency. Firstly, for each material sample S_{21} curve, a piece-wise approximated conductivity and frequency vector was obtained. This was achieved by finding the fix-conductivity curve (say σ_A) that is the closest to the measured curve at a specific frequency (say f_A). Next step is plotting the skin depth value against the values of the obtained

conductivity-frequency vector. The skin depth (δ) was introduced in §2.5 and was re-visited in §5.2. It is given by

$$\delta = \sqrt{\frac{2}{\omega\mu\sigma}} \qquad (7.3)$$

where ω is the radian frequency, μ and σ are the permeability and conductivity of the panel material respectively. Being a non-magnetic material, the free space permeability ($\mu_o = 4\pi\times10^{-7}$H/m) is used. In this way, the skin depth of one pair of conductivity-frequency values will be given as

$$\delta(\sigma_A, f_A) = \sqrt{\frac{2}{2\pi f_A \mu_o \sigma_A}} \qquad (7.4)$$

By plotting the skin depth for the two material samples, we get Figure 7.15.
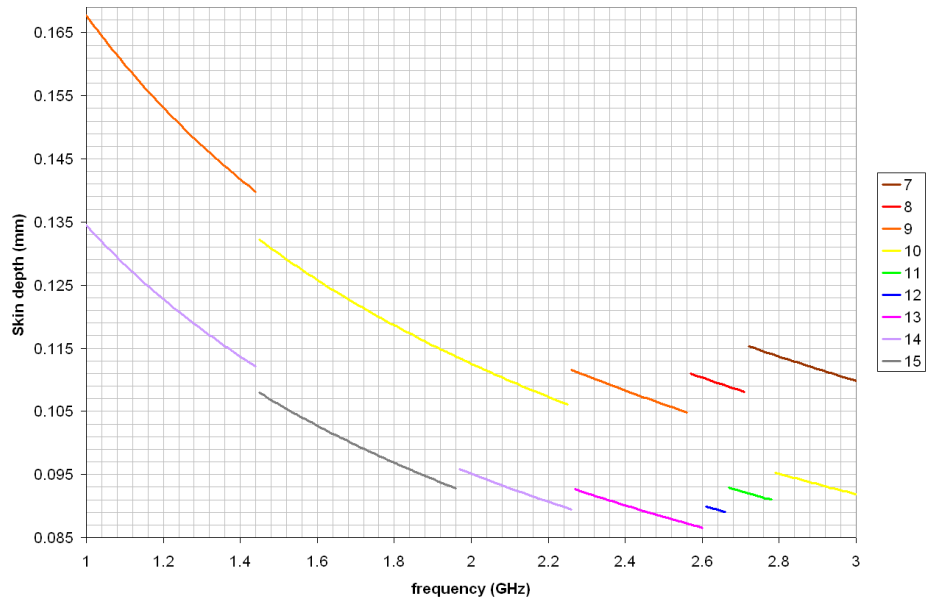
Figure 7.15. A piece-wise approximation to the skin depth corresponding to the measurement curves shown in Figure 7.14. The upper approximated curve is related to CFC1 and the lower is for the CFC2. These curves segments are relevant to conductivities ranging from 7k S/m to 15k S/m as indicated in the figure legend.

Figure 7.16 illustrates the case with the empty cavity that can be regarded as a reference when assessing the transmission parameter (S_{21}) of the two composite materials. The third peak (at about 2.5GHz) for the two curves is misaligned with the analytic value of the resonant frequency. It was suggested in §6.5.2 that this difference is introduced with the use of the transmitting and receiving monopoles.
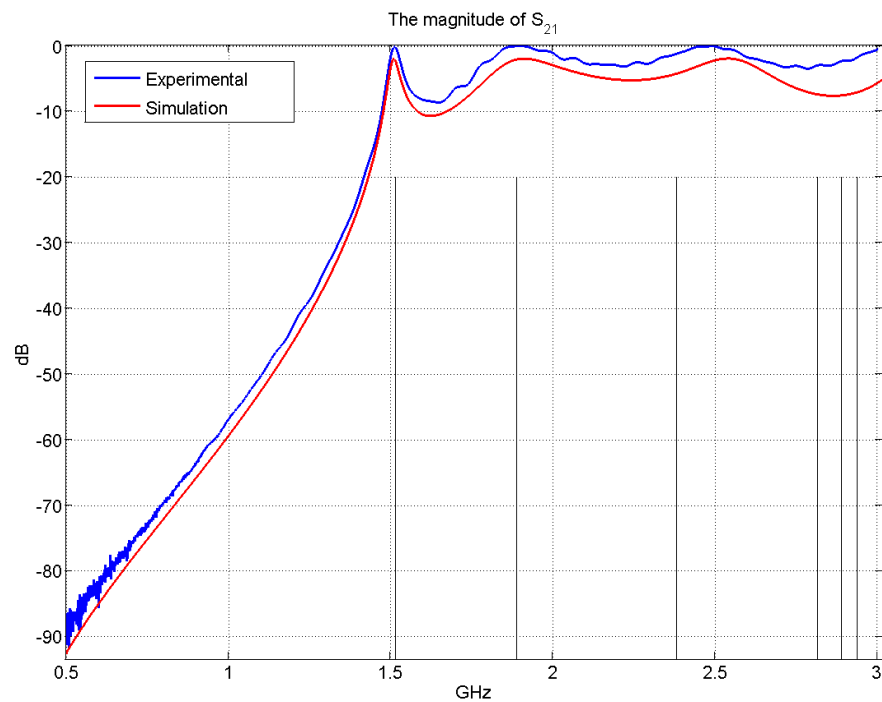
Figure 7.16. The magnitude of the S_{21} parameter in the case of empty cavity. Analytic resonant frequencies are shown as vertical lines.

7.7 Validation with Drude Model

This section aims to provide further validation by deriving a theoretical model from the experimental measurements. Figure 7.14 has suggested frequency-dependent material properties. This behaviour is further emphasised in Figure 7.15 that has suggested values of conductivities for samples CFC1 and CFC2. The frequency-dependent conductivity is a

complex term that can be characterised by the Drude model as given by the following equation [7.2, 7.12 to 7.14].

$$\sigma(\omega) = \frac{G_o}{1 + j\omega\,\tau_o} \qquad (7.5)$$

where G_o is the complex conductivity at DC value and τ_o is the relaxation time for electron scattering.

Equation (7.5) can be looked at as a capacitor connected in parallel with a branch of a series combination of conductance and an inductance. This equivalent circuit is shown in Figure 7.17
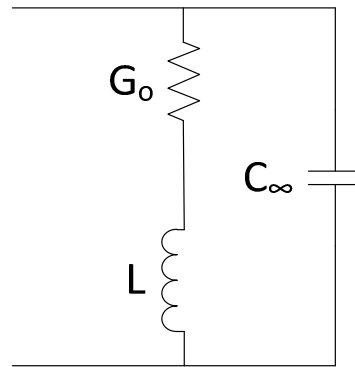
Figure 7.17. The equivalent circuit for a conductor that complies with Drude Model.

To find the Drude model for the two material samples that were used in this study, two parameters need to be found, namely G_o and τ_o. Figure 7.18 is derived from Figure 7.14 by expressing the conductivities over their relevant frequencies. Frequencies below 1.44GHz are excluded because of the noise involved. Presuming that the conductivity does not decay by a noticeable amount, the DC value of conductivity (G_o) can be assumed to be 10kS/m and 15kS/m for CFC1 and CFC2 respectively. These are the representative conductivities at 1.44GHz. The relaxation time (τ_o) can be found by

$$\tau_o = \frac{1}{2\pi f_o} \qquad\qquad (7.6)$$

where f_o is the frequency at which the corresponding conductivity $\sigma(\omega)$ is equal to half the value of G_o. To find its value a quadratic polynomial has been fitted to the piece-wise approximation (Figure 7.18) to extrapolate the value of f_o. The fitted curve equation can be solved for the variable **f** after setting the conductivity to 5kS/m and 7.5kS/m for CFC1 and CFC2 respectively. In this way f_o was found to be 3.307GHz and 3.267GHz for CFC1 and CFC2 respectively. According to equation (7.6), the relaxation factor was found to be 48.13ps and 48.72ps for CFC1 and CFC2 respectively.
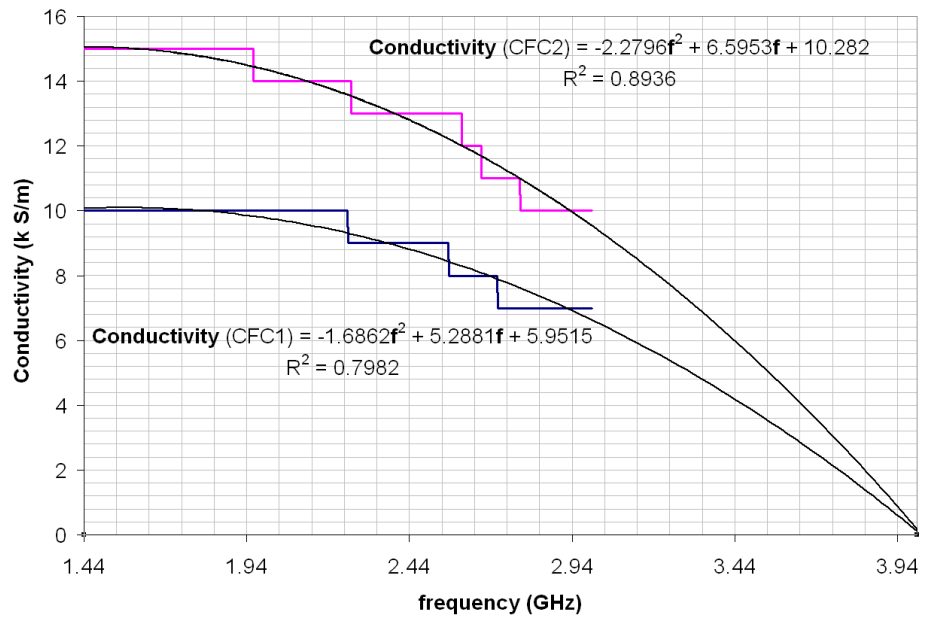
Figure 7.18. A piece-wise approximation for the conductivities that the CFC1 and CFC2 samples have covered. Quadratic polynomial fit shows the frequency at which half the maximum conductivity can be determined.

However, by trial and error better agreement for Drude model was achieved for different values of G_o and τ_o. Thus, a better G_o was found to be 8.5k S/m and 13k S/m for CFC1 and CFC2 respectively. Similarly,

better τ_o was found to be 70ps and 80ps respectively. Despite following the right approach in finding G_o and τ_o, there was a large error in estimating their values. This could be due to the relatively large difference (1000S/m) between each two successive fixed-conductivity S_{21} curves. This has significantly reduced the resolution and hence increased the error in estimating Drude model parameters.

The real part and imaginary parts of equation (7.5) are given by

$$\mathrm{Re}[\sigma(\omega)] = \frac{G_o}{1 + \omega^2\, \tau_o^2} \tag{7.7}$$

$$\mathrm{Im}[\sigma(\omega)] = \frac{-G_o\, \omega\tau_o}{1 + \omega^2\, \tau_o^2} \tag{7.8}$$

Equations (7.7) and (7.8) have been used with the updated Drude parameters to produce Figure 7.19 for the two samples CFC1 and CFC2. The imaginary part is shown multiplied by minus one.
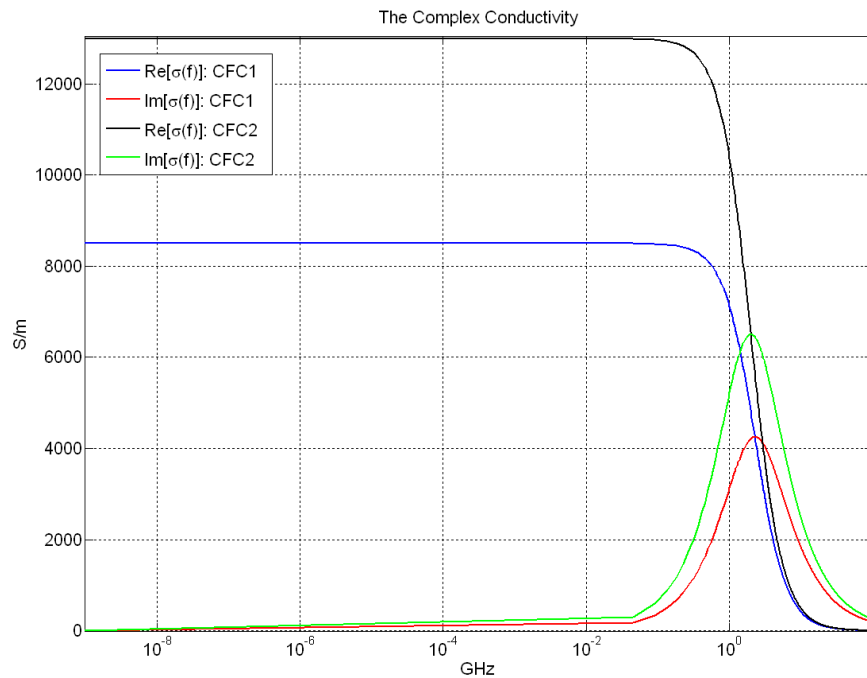
Figure 7.19. The theoretical complex conductivity for the two samples CFC1 and CFC2. The absolute value is shown for the imaginary parts.

Further attempt to verify the analytic Drude model was carried out by producing a one-dimensional TLM model in two forms: fine-mesh and coarse mesh with digital filter simulating the material sample. Both samples were modelled in the two forms. Thus, four sets of results were obtained to be compared to the analytic solution. For the fine mesh model, the sample width was represented by 20 TLM cells. The two 1D models are shown in Figure 7.20.
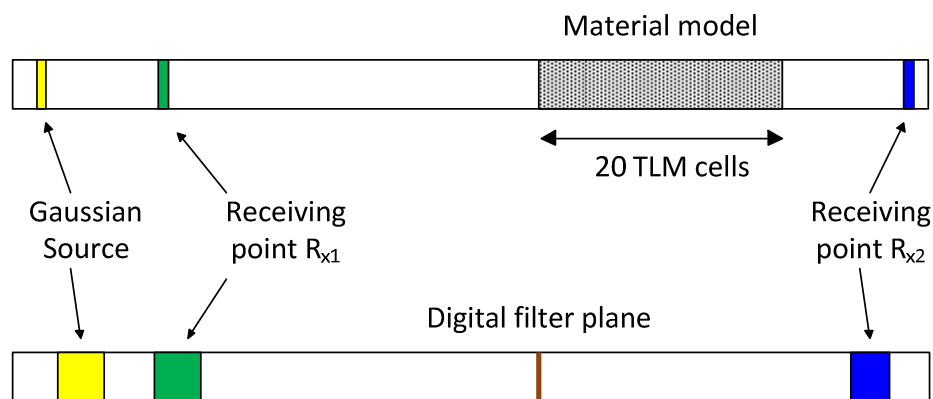
Figure 7.20. The one-dimensional geometries that were used to simulate the Drude model for the two material samples. The conventional fine mesh is at the top and its coarse mesh version is shown in the bottom.

Concerning the fine mesh model, using the one-dimensional setup, the reflection coefficient (Γ) and the transmission coefficient (T) were found from the received pulse at points R_{x1} and R_{x2} respectively. These Γ and T curves are shown in Figure 7.21 compared to the analytic curves that can be found according to the digital filter design equations (5.8 to 5.12) with complex conductivity. This complex conductivity is defined according to Drude model given by equation (7.5), where G_o and τ_o are given in Table 7.3 for the two samples. It is clear from Figure 7.21 that there is a good agreement with the analytic Drude model.
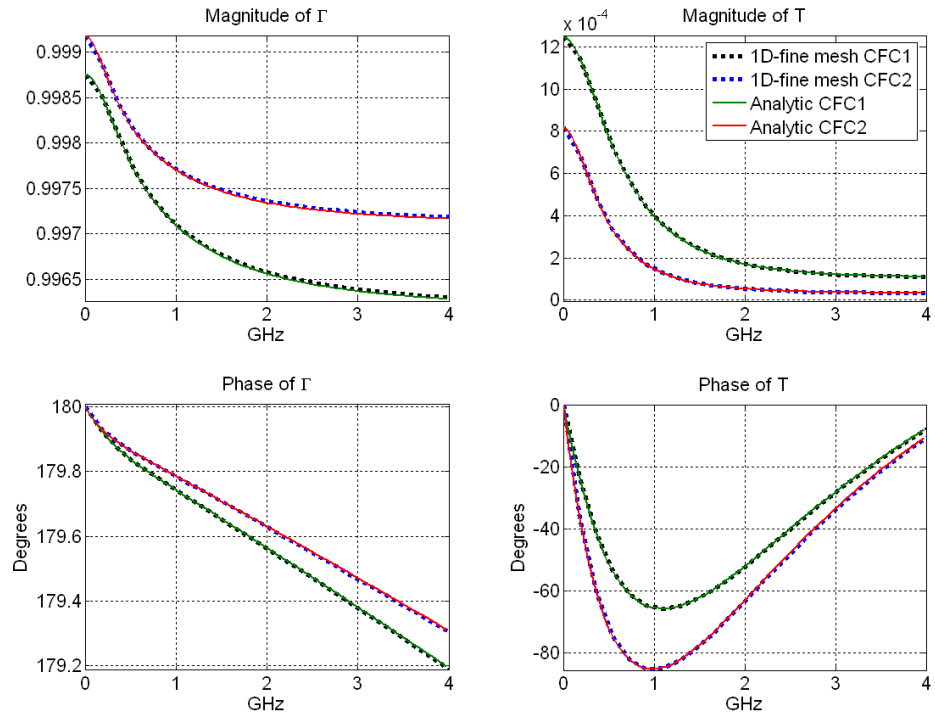
Figure 7.21. Validation of the one-dimensional fine mesh simulated model with the Drude analytic model.

Parameter	CFC1	CFC2
NT	131072	
NX.NY.NZ	1222 x 1 x 1	
dl (mm)	0.025	
dt (ps)	0.0416955	
Excitation with polarisation	Gaussian pulse at z	
Excitation point	(100,0,0)	
G_o (S/m)	8500	13000
τ_o (ps)	70	80
Receiving point R_{x1}	(300,0,0)	
Receiving point R_{x2}	(1199,0,0)	

Table 7.3. The setting parameters that were used to produce Figure 7.21.

The results of the digital filter version are compared with the analytic solution in Figure 7.22, which has shown a good agreement between the model and the analytic solution. As can be seen in Table 7.4, the coarse mesh space step is a hundred times larger than that in Table 7.3 for the fine mesh. This means that the coarse mesh / digital filter model has produced the same accuracy with much less computational efforts.
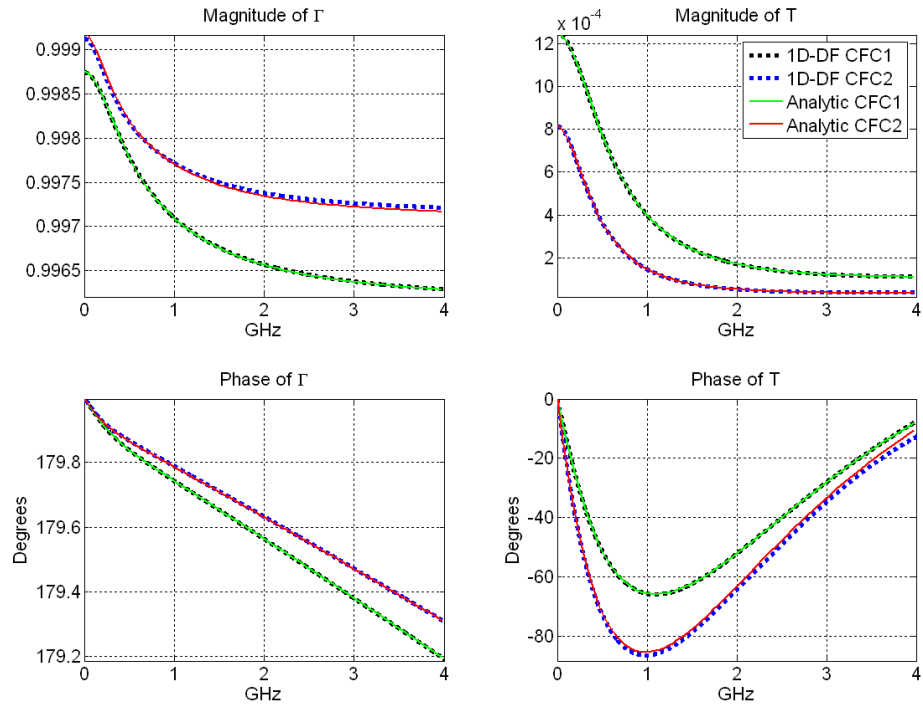
Figure 7.22. Validation of the one-dimensional model of coarse mesh with digital filter with the Drude analytic model.

Parameter	CFC1	CFC2
NT	131072	
NX.NY.NZ	14 x 1 x 1	
dl (mm)	2.5	
dt (ps)	4.16955	
Excitation with polarisation	Gaussian pulse at z	
Excitation point	(1,0,0)	
G_o (S/m)	8500	13000
τ_o (ps)	70	80
Receiving point R_{x1}	(3,0,0)	
Receiving point R_{x2}	(12,0,0)	

Table 7.4. The setting parameters that were used to produce Figure 7.22.

Returning back to the three-dimensional geometry that was presented in Figure 6.32, the Drude model was applied instead of the fixed conductivity material. The results of the Drude model are compared to the case of fixed conductivity and the laboratory experimental data in Figure 7.23. Table 7.5 states the simulation settings that were applied to

produce the four simulation curves in Figure 7.23. It is obvious that the application of Drude model has improved the S_{21} curve over the frequencies from 2GHz to around 2.6GHz, where the fixed conductivity model has failed to represent.
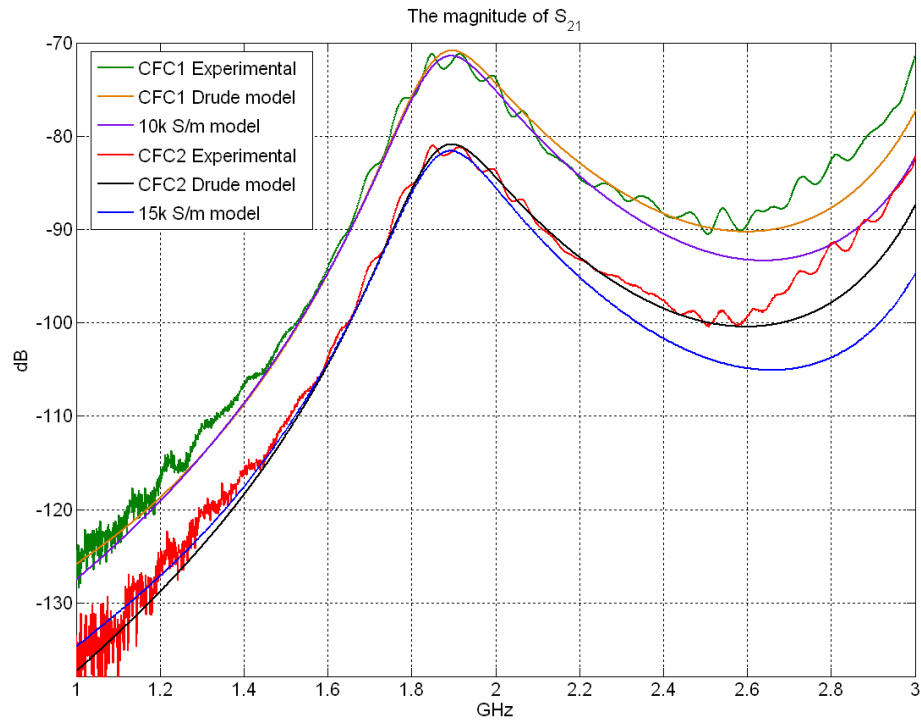
Figure 7.23. The application of the frequency-dependent conductivity using the Drude model proved to provide better representation for the measurement data.

Parameter	Shared settings
NT	524288
NX.NY.NZ	78 x 37 x 18
dl (mm)	2.962025
dt (ps)	4.94013
Excitation with polarisation	Gaussian pulse at *z*
Excitation plane	3 x 3 x 1
L_d (mm)	0.5
ε_r	5
Receiving point	(73,18,16)

Table 7.5. The simulation settings that produced Figure 7.23.

7.8 Summary

In this chapter experimental results for a range of configurations were presented. The experimental results were compared with simulations based on numerical models derived in previous chapters.

The experimental configuration is then demonstrated and the measurements procedure steps were clarified. The results were presented with their analysis. It was shown how these measurements have validated the simulation modelling that was the subject of chapter six. Finally, an analytic model was developed to serve in further validation for the achieved results.

References

[7.1] M.T. Sebastian, *Dielectric Materials for Wireless Communications*. Elsevier, Amsterdam, 2008.

[7.2] L.F. Chen, C.K. Ong, C.P. Neo, V.V. Varadan and V.K. Varadan, *Microwaves Electronics: Measurement and Material Characterisation*. John Wiley & Sons Inc, New York, NY, 2004.

[7.3] J. Krupka, *Frequency domain complex permittivity measurements at microwave frequencies*. Measurement Science and Technology, Vol. 17, pp. R55-R70, 2006

[7.4] M.S. Sarto and A. Tamburrano, *Innovative Test Method for the Shielding Effectiveness Measurement of Conductive Thin Films in a Wide Frequency Range*. IEEE Transactions on Electromagnetic Compatibility, Vol. 48, No.2, pp. 331-341, May 2006.

[7.5] J. Baker-Jarvis, E.J. Vanzura, and W.A. Kissick, *Improved Technique for Determining Complex Permittivity with the Transmission/Reflection Method*. IEEE Transactions on Microwave Theory and Techniques, Vol. 38, No.8, pp. 1096-1103, Aug 1990.

[7.6] A.M. Nicolson, *Measurement of the Intrinsic Properties of Materials by Time-Domain Techniques*. IEEE Transactions on Instrumentation and Measurement, Vol. IM-19, No.4, pp. 377-382, Nov 1970.

[7.7] ASTM D4935-99, *Standard Test Method for Measuring the Electromagnetic Shielding Effectiveness of Planar Materials*, ASTM, 2001.

[7.8] T. Konefal, J.F. Dawson, A.C. Denton, T.M. Benson, C. Christopoulos, A.C. Marvin, S.J. Porter, and D.W.P. Thomas, *Electromagnetic Coupling Between Wires Inside a Rectangular Cavity Using Multiple-Mode-Analogous-Transmission-Line Circuit Theory*. IEEE Transactions on Electromagnetic Compatibility, Vol. 43, No.3, pp. 273-281, Aug 2001.

[7.9] T. Konefal, J.F. Dawson, A.C. Marvin, M.P. Robinson, and S.J. Porter, *A Fast Multiple Mode Intermediate Level Circuit Model for the Prediction of Shielding Effectiveness of a Rectangular Box Containing a Rectangular Aperture*. IEEE Transactions on Electromagnetic Compatibility, Vol. 47, No.4, pp. 678-691, Nov 2005.

[7.10] S.W. Wong and L. Zhu, *EBG-Embedded Multiple-Mode Resonator for UWB Bandpass Filter with Improved Upper-Stopband*

Performance. IEEE Transactions on Microwave and Wireless Components Letters, Vol. 17, No.6, pp. 421-423, Jun 2007.

[7.11] D.C.L. Chung, *Carbon Fiber Composites*. Butterworth-Heinemann, Boston, 1994.

[7.12] B.K.P. Scaife, *Principles of Dielectrics*. Clarendon Press, Oxford, 1989.

[7.13] J.D. Jackson, *Classical Electrodynamics*. John-Wiley and Sons, New York, 3rd ed., 1999.

[7.14] Dressel and Grüner, *Electrodynamics of Solids*. Cambridge University Press, UK, 2002

8

Discussion and Conclusion

This chapter provides an overall assessment of the work conducted in this study. It starts with a review where the principal points are discussed. Throughout this work, a number of difficulties have triggered some ideas that can serve to improve this work in the future. Some suggestions are stated in the next section. The thesis ends with the final conclusion.

8.1 Discussion

The work in this study has addressed two issues. The first is building models for electromagnetic shields for some practical cavities. The second is validating the developed models by conducting practical experimental setups using anisotropic panels as shields. In the following, the major findings of the study work are discussed.

Chapter 2 has shown that EMI can be reduced by the use of the proper shield. It was emphasised that the two basic forms of behaviour of an electromagnetic (EM) wave going through a barrier are: 1) leaking through apertures (if there are any) governed by the wave theory; 2) penetrating through the barrier wall governed by the diffusion theory (also called the shielding theory). It was stated that the material conductivity and permittivity determine the dominant behaviour of a wave propagating at a given frequency. For example, at low frequencies, the material permittivity controls the magnetic SE, while at high frequencies, the material conductivity controls the electric SE. The shielding effectiveness (SE) was defined in two ways and the factors that affect it were stated.

Chapter 3 has presented the carbon fibre composites (CFCs) as promising material that have attractive material properties. Moreover, CFC materials can be fabricated to provide conductivities that are sufficient to make them suitable for EMI shielding. CFC can be modelled by homogenising the material or by applying the cascading formulae to the individual layers that collectively form the stacked CFC panel. The CFC structure was explained and it was shown how this structure can determine the panel strength and shielding effectiveness (SE). The CFC electrical properties were stated with some typical values. A formula that can estimate the conductivity of a composite material from its constituents was given along with its validity constraints. It was stated that anisotropic media show a position-dependent property. This may affect the alignment between E and D; between H and B; and between E and J due to the material permittivity, permeability, and conductivity respectively. Homogenisation can be applied to a particular layer within the composite panel or on the whole panel. With the reduction in CFC prices, it was expected that the future will witness new fields of applications for the CFC.

Chapter 4 has revealed that numerical modelling by simulation is recommended for complex structure due to the lack of analytic solution. The choice of the TLM method was justified by comparing it to the other candidate methods and by demonstrating its attractive features. It is clear that under some circumstances, TLM may not be the best choice. After introducing the three-dimensional symmetrical condensed node, some guidelines were shown on how to implement TLM in this study.

Chapter 5 has introduced the concept of thin panels. Due to the multiple reflections, special treatment is required for thin panels in two ways: 1) the multiple reflections call for the use of special formulae that take into considerations the total reflection and the total transmission. These formulae are modifications for Fresnel's basic equations; 2) being thin, numerical modelling can impose a huge burden on computational resources. This is due to the small space step required to resolve the thickness of the panel. A digital filter structure was derived based on the physical properties of the reflection and the transmission of EM waves. The choice of the design parameters of digital filters was described in detail. The computation of the reflection coefficient (Γ) and the transmission coefficient (T) was illustrated. The design and implementation of models that use digital filters was demonstrated through a detailed example, which has also exemplified the application of the cascade formulae with a successful test of symmetry as shown in Figures 5.29 and 5.31. Good agreement has been shown between fine mesh and the corresponding coarse mesh that has implemented digital filters as shown in Figure 5.32. It was shown that speed up in simulation run time due to the use of digital filters has been greatly boosted especially in three-dimensional configurations.

Chapter 6 has reviewed the digital filter design parameters with some guidelines on how to select their values. As demonstrated in Chapter 5, good agreement was shown between fine mesh model and the corresponding digital filter version. This is demonstrated in Figure 6.9 for a three-dimensional geometry. It was shown that the material

conductivity has a direct effect on the SE such that doubling the conductivity means adding 6dBs on SE as shown in Figure 6.11. In addition to the material properties of the panel, the dimensions of the panel have been investigated in terms of their effect on SE. For a given cavity at a specified frequency, an empirical formula (equation 6.9) has been found that links the SE improvement to the size of a window that is made of a material with known properties. The elapsed run time has been shown to be reduced dramatically when using digital filters with coarse mesh as illustrated in Table 6.7. Moreover, when using digital filters, the SE can still be obtained (with negligible differences) when increasing the space step (dl) by three or four times. A special shield behaviour (referred to as the two-phase feature) was noticed in the main pattern of the SE, which is found to be linked to the thickness of the shielding panel (Figure 6.31) and the polarisation of the excitation (Figures 6.18 to 6.23). The effect of the receiving point location has shown to have some effect on SE amplitude as shown in Figure 6.25 and 6.26. However, no impact on the two-phase feature was found. The surface current was determined on the outer face of the modelled box and it showed a pattern of symmetry when the excitation frequency is equal to the split frequency as shown in Figure 6.28. The effect of the monopoles on the transmission coefficient S_{21} was investigated, where a thick monopole was found to cause less sharp features in S_{21} pattern compared to the wire monopole as shown in Figure 6.37. Moreover, the less sharp effect was also observed when using longer wire monopoles as shown in Figure 6.35 and 6.36. The resonant frequencies over 2GHz were found to

get shifted from their analytic values when using thicker or longer monopoles. The investigation of the effect of the panel material has revealed that the general trend of S_{21} for low conductivity (e.g., 5kS/m) has almost a wave-like behaviour at frequencies greater than 3GHz while higher conductivities have exemplified diffusion behaviour as shown in Figure 6.41.

Chapter 7 has reviewed the main known microwave characterisation measurement methods and has compared the closest method (denoted as the hollow metallic waveguide method) to the practical approach that was adopted in this study. The comparison has shown a number of advantages for our method over the hollow metallic waveguide method. Unlike the hollow metallic waveguide method, the adopted practical method supports multiple–mode excitation and it works over wider frequency range by 1.6GHz. Also, it has an attractive cost-effectiveness feature being able to be set up without the need to the extended waveguide sections as clarified in §7.3. The experimental results were used to validate the models that were developed. The experimental results have manifested frequency-dependent characteristics as shown in Figure 7.14. Accordingly, a Drude model was developed based on the fixed-conductivity models. Drude model has shown better agreement to the experimental data as shown in Figure 7.23.

8.2 Future Work

Further work can be done regarding a number of parameters that govern the modelling process and its validation as follows.

- *Lower frequencies*. It was shown in Chapter 6 that frequencies below 1GHz do not always reveal accurate values in terms of shielding effectiveness (SE) or the transmission parameter (S_{21}). Such low frequencies can be obtained with higher accuracy when using frequency-domain method like the Method of Moment (MoM). Later, validation can be performed using the GTEM cell.

- *Higher frequencies*. Usually, for each model there is a highest frequency limit that beyond which the model is not valid. The highest experimental frequency was 3GHz. This is the maximum frequency limit of the network analyser. By using equipment with higher frequency rates, attempts can be made to find out the highest frequency for which the model is valid.

- *The Drude model*. Further investigations can be made on choosing the DC conductivity (G_o) and the relaxation time (τ_o) to produce better agreement with the simulated model at frequencies higher than 2.5GHz.

- *The TLM solver*. The components under modelling are represented by stubs when building the network of the TLM nodes. Stubs are not always the optimum representation. Accordingly, one can set a criterion that lets the solver to choose between stub- and link-representation when modelling a component. This arrangement can have the effect of enhancing the accuracy of the numerical model.

- *Anisotropic characterisation*. The complex structure of composite materials has given it anisotropic features. This

structure can be represented as a number of layers stacked together. Using the cascade formulae, these layers can be modelled as a cascade of digital filters.

8.3 Overall Conclusion

The main objectives of this study were stated in §1.2. The discussion in §8.1 has shown how these objectives were tackled throughout this study. Better knowledge was gained on predicting electromagnetic behaviour with the developed numerical models as demonstrated in Chapter 6. Cascading can now be applied on multiple panels or multiple structures within the system under modelling. Computational effort was considerably reduced in terms of memory and time when using a coarse mesh with embedded digital filters. This is because the coarse mesh employed has led to storing less data representing the network of TLM nodes describing the system. The elapsed run time was saved because smaller number of TLM nodes has to be solved in every iteration, besides, the simulation time (NT x dt) can be covered with less iterations due to the larger time step ($dt = 2dl/u$) involved. The simulated models were validated in three ways: 1) the 1D model has shown an agreement with the analytic solution; 2) the 2D model has shown a good agreement with the corresponding fine mesh version; 3) the 3D model has shown a good agreement (over a frequency range) with the experimental results using the Drude model. Overall, this study has a number of possible practical applications. For an existing panel, this work can analyse the current distribution whether it is at the surface or inside the panel. The

pattern of this current distribution can be used to study the magnetic properties of the panel under test at a specific frequency. Moreover, the shielding effectiveness can be found for a box that is made of a given material and contains the device that is meant to be shielded. In the commercial manufacturing of CFC materials for the purpose of shielding, this study can serve in providing broad guidelines that assist in manufacturing the right CFC panel for the right shielding application. Furthermore, this work can be extended to help locating the weak points in a CFC panel when it is hit by lightning. This can be done by modelling the CFC panel in its micro-scale level. This requires information regarding the physical distribution of the carbon fibres within the polymer matrix.

The final conclusion is that the TLM method with digital filtering has been successfully applied to a number of thin panels embedded in the main system. This has made a considerable saving in computer resources and simulation time. The cascading of various materials has been modelled. An anisotropic material (the composite CFC) has been tested and has proved to validate the relevant frequency-dependent models within a certain frequency range. Eventually, these results have led to gaining a better understanding of the electromagnetic behaviour of modern shields.

Appendix A

Digital Filters' Coefficients

Throughout this study, 123 various digital filters were designed. In Chapter 5, it was shown how to derive the coefficients of the digital filter. In this appendix, the derived coefficients of the digital filters that were demonstrated in Chapter 6 and Chapter 7 will be stated. If the number of zeros (NZ) is not stated, it means it is equal to the number of poles (NP). For each set of digital filter coefficients, the following plot information will be stated: trace title (the label of the trace under which the digital filter performance is plotted), figure number, section number, and the page number.

Trace label	Figure	Section	page
All five traces	6.3	6.2.2.1.1	129
All five traces	6.5	6.2.2.1.1	130
Both two traces	6.33	6.5.1	161
20	6.41	6.5.3	169
20	6.42	6.5.3	170

	$S_{11} = S_{22}$	$S_{21} = S_{12}$
NP	6	9
b_o	-0.9119	-4.6076e-010
b_1	-2.2467e+012	136.3096
b_2	-7.7755e+023	-3.9238e+013
b_3	-7.8255e+034	6.9427e+024
b_4	-2.5933e+045	-1.0337e+036
b_5	-2.5426e+055	1.1392e+047
b_6	-4.7218e+064	-9.8152e+057
b_7		6.0597e+068
b_8		-2.4642e+079
b_9		4.9372e+089
a_1	2.3136e+012	2.1440e+011
a_2	7.8957e+023	2.5754e+022
a_3	7.8948e+034	1.7718e+033
a_4	2.6061e+045	7.6940e+043
a_5	2.5486e+055	2.0269e+054
a_6	4.7246e+064	3.1471e+064
a_7		2.5759e+074
a_8		9.2912e+083
a_9		9.3004e+092

Trace label	Figure	Section	page
Coarse mesh/digital filter	6.9	6.3	136
All three traces	6.18	6.4.4.1.1	147
All three traces	6.19	6.4.4.1.1	148
All three traces	6.20	6.4.4.1.2	149
All three traces	6.21	6.4.4.1.2	149
All three traces	6.22	6.4.4.1.3	150
All three traces	6.23	6.4.4.1.3	151
All nine traces	6.25	6.4.4.2	153
(contour lines)	6.26	6.4.4.2	154
(vector field)	6.27	6.4.4.3.1	155
(vector field)	6.28	6.4.4.3.2	156
(vector field)	6.29	6.4.4.3.3	157

	S_{11}	$S_{21} = S_{12}$	S_{22}
NP	3	5	3
b_o	-0.7689	-1.3163e-006	-0.8277
b_1	-4.1570e+011	1.4598e+005	-4.4680e+011
b_2	-2.2474e+022	-2.2604e+016	-2.4764e+022
b_3	-1.4660e+032	1.4550e+027	-1.7863e+032
b_4		-7.6497e+037	
b_5		1.6481e+048	
a_1	4.4906e+011	5.7541e+010	4.7221e+011
a_2	2.3134e+022	2.5259e+021	2.5295e+022
a_3	1.4739e+032	3.6614e+031	1.7945e+032
a_4		2.7752e+041	
a_5		4.5456e+050	

Trace label	Figure	Section	page
6500S/m	6.11	6.4.1	138
All six traces	6.15	6.4.3	143

	$S_{11} = S_{22}$	$S_{21} = S_{12}$
NP	5	6
b_o	-0.8692	3.9843e-007
b_1	-1.6448e+012	-1.5738e+005
b_2	-4.2014e+023	4.4163e+016
b_3	-2.8810e+034	-8.1800e+027
b_4	-5.5654e+044	1.0690e+039
b_5	-2.1603e+054	-8.9359e+049
b_6		3.6987e+060
a_1	1.7195e+012	2.8021e+011
a_2	4.2968e+023	3.4358e+022
a_3	2.9161e+034	2.0695e+033
a_4	5.5982e+044	6.0091e+043
a_5	2.1638e+054	7.1557e+053
a_6		2.2682e+063

Trace label	Figure	Section	page
8000S/m	6.11	6.4.1	138

	$S_{11} = S_{22}$	$S_{21} = S_{12}$
NP	6	6
b_o	-0.8611	2.4340e-007
b_1	-2.2978e+012	-7.2488e+004
b_2	-8.7072e+023	1.7799e+016
b_3	-9.9279e+034	-2.7156e+027
b_4	-3.9427e+045	3.0028e+038
b_5	-5.0858e+055	-2.0846e+049
b_6	-1.4627e+065	7.1766e+059
a_1	2.4114e+012	2.0289e+011
a_2	8.9333e+023	1.9709e+022
a_3	1.0079e+035	9.3742e+032
a_4	3.9775e+045	2.1933e+043
a_5	5.1088e+055	2.1022e+053
a_6	1.4646e+065	5.4180e+062

Trace label	Figure	Section	page
1000S/m	6.11	6.4.1	138
0.5mm	6.31	6.4.4.4	158

	$S_{11} = S_{22}$	$S_{21} = S_{12}$
NP	3	3
b_o	-0.7388	-2.6380e-004
b_1	-1.0634e+012	1.5488e+008
b_2	-1.6876e+023	-5.0350e+019
b_3	-4.3061e+033	7.8594e+030
a_1	1.1653e+012	3.4554e+011
a_2	1.7541e+023	3.4005e+022
a_3	4.3518e+033	7.4807e+032

Trace label	Figure	Section	page
2000S/m	6.11	6.4.1	138

	$S_{11} = S_{22}$	$S_{21} = S_{12}$
NP	3	3
b_o	-0.8406	-1.1585e-004
b_1	-7.5335e+011	3.0158e+007
b_2	-7.2558e+022	-5.2479e+018
b_3	-1.0312e+033	4.0219e+029
a_1	7.9292e+011	1.4516e+011
a_2	7.4073e+022	7.0430e+021
a_3	1.0367e+033	7.5976e+031

Trace label	Figure	Section	page
500S/m	6.11	6.4.1	138

	$S_{11} = S_{22}$	$S_{21} = S_{12}$
NP	2	2
b_o	-0.7253	0.0020
b_1	-5.7804e+011	-1.0283e+009
b_2	-3.5157e+022	2.4658e+020
a_1	6.3033e+011	2.5465e+011
a_2	3.5904e+022	1.1860e+022

Trace label	Figure	Section	page
5000S/m	6.11	6.4.1	138

	$S_{11} = S_{22}$	$S_{21} = S_{12}$
NP	4	5
b_o	-0.8781	-2.2578e-006
b_1	-1.0919e+012	7.3325e+005
b_2	-1.6860e+023	-1.7579e+017
b_3	-5.6954e+033	2.6052e+028
b_4	-3.3427e+043	-2.4849e+039
b_5		1.1516e+050
a_1	1.1365e+012	2.1599e+011
a_2	1.7177e+023	1.9964e+022
a_3	5.7432e+033	8.0931e+032
a_4	3.3499e+043	1.3053e+043
a_5		5.4325e+052

Trace label	Figure	Section	page
All three traces	6.13	6.4.2	140

	$S_{11} = S_{22}$	$S_{21} = S_{12}$
NP	5	6
b_o	-0.8910	1.7516e-007
b_1	-1.5683e+012	-4.3762e+004
b_2	-3.7189e+023	1.0200e+016
b_3	-2.3227e+034	-1.3842e+027
b_4	-3.9484e+044	1.4099e+038
b_5	-1.2707e+054	-8.8094e+048
b_6		2.7522e+059
a_1	1.6266e+012	1.6418e+011
a_2	3.7875e+023	1.4090e+022
a_3	2.3454e+034	5.8038e+032
a_4	3.9665e+044	1.2067e+043
a_5	1.2722e+054	1.0171e+053
a_6		2.3403e+062

Trace label		Figure	Section	page
0.05mm		6.31	6.4.4.4	158

	$S_{11} = S_{22}$	$S_{21} = S_{12}$
NP	1	1
b_o	-0.5577	-0.0351
b_1	-3.0618e+012	2.5940e+011
a_1	3.3869e+012	2.7025e+012

Trace label		Figure	Section	page
0.1 mm		6.31	6.4.4.4	158

	$S_{11} = S_{22}$	$S_{21} = S_{12}$
NP	1	1
b_o	-0.7351	-0.0176
b_1	-9.4978e+011	3.3598e+010
a_1	1.0002e+012	6.6648e+011

Trace label		Figure	Section	page
1.0 mm		6.31	6.4.4.4	158

	$S_{11} = S_{22}$	$S_{21} = S_{12}$
NP	3	3
b_o	-0.8209	-7.9892e-005
b_1	-4.8300e+011	9.3103e+006
b_2	-2.9729e+022	-9.9635e+017
b_3	-2.5350e+032	3.8676e+028
a_1	5.1186e+011	5.5702e+010
a_2	3.0415e+022	1.4678e+021
a_3	2.5490e+032	7.1526e+030

Trace label		Figure	Section	page
19		6.41	6.5.3	169
19		6.42	6.5.3	170

	$S_{11} = S_{22}$	$S_{21} = S_{12}$
NP	6	9
b_o	-0.9142	-5.6835e-010
b_1	-2.0380e+012	183.3065
b_2	-6.4476e+023	-5.3699e+013
b_3	-5.9184e+034	1.0026e+025
b_4	-1.7767e+045	-1.5395e+036
b_5	-1.5650e+055	1.7742e+047
b_6	-2.6098e+064	-1.5864e+058
b_7		1.0223e+069
b_8		-4.3304e+079
b_9		9.0628e+089
a_1	2.0975e+012	2.3754e+011

a_2	6.5452e+023	3.0309e+022
a_3	5.9695e+034	2.2291e+033
a_4	1.7852e+045	1.0238e+044
a_5	1.5685e+055	2.8592e+054
a_6	2.6113e+064	4.6826e+064
a_7		4.0486e+074
a_8		1.5374e+084
a_9		1.6223e+093

Trace label	Figure	Section	page
18	6.41	6.5.3	169
18	6.42	6.5.3	170

	$S_{11} = S_{22}$	$S_{21} = S_{12}$
NP	6	9
b_o	-0.9083	-7.0035e-010
b_1	-2.1979e+012	246.4215
b_2	-7.4946e+023	-7.3952e+013
b_3	-7.4456e+034	1.4575e+025
b_4	-2.4410e+045	-2.3191e+036
b_5	-2.3784e+055	2.7990e+047
b_6	-4.4434e+064	-2.6074e+058
b_7		1.7579e+069
b_8		-7.7833e+079
b_9		1.7062e+090
a_1	2.2664e+012	2.6289e+011
a_2	7.6159e+023	3.5814e+022
a_3	7.5146e+034	2.8194e+033
a_4	2.4537e+045	1.3748e+044
a_5	2.3843e+055	4.0788e+054
a_6	4.4462e+064	7.0696e+064
a_7		6.4711e+074
a_8		2.5954e+084
a_9		2.8938e+093

Trace label	Figure	Section	page
17	6.41	6.5.3	169
17	6.42	6.5.3	170

	$S_{11} = S_{22}$	$S_{21} = S_{12}$
NP	6	8
b_o	-0.9077	2.4889e-009
b_1	-2.1112e+012	-617.7923
b_2	-6.9609e+023	1.6493e+014
b_3	-6.6976e+034	-2.5067e+025
b_4	-2.1293e+045	3.2659e+036
b_5	-2.0181e+055	-2.9685e+047

b_6	-3.7068e+064	2.0203e+058
b_7		-8.7249e+068
b_8		1.8830e+079
a_1	2.1778e+012	1.7035e+011
a_2	7.0750e+023	1.7288e+022
a_3	6.7605e+034	9.4381e+032
a_4	2.1405e+045	3.1771e+043
a_5	2.0232e+055	5.9477e+053
a_6	3.7093e+064	5.9417e+063
a_7		2.5286e+073
a_8		3.0223e+082

Trace label	Figure	Section	page
16	6.41	6.5.3	169
16	6.42	6.5.3	170
16	7.14	7.6	191

	$S_{11} = S_{22}$	$S_{21} = S_{12}$
NP	6	8
b_o	-0.9025	3.1638e-009
b_1	-2.2169e+012	-872.4368
b_2	-7.6735e+023	2.3575e+014
b_3	-7.7610e+034	-3.8338e+025
b_4	-2.6037e+045	5.1553e+036
b_5	-2.6190e+055	-4.9522e+047
b_6	-5.1359e+064	3.5138e+058
b_7		-1.5988e+069
b_8		3.6189e+079
a_1	2.2908e+012	1.9391e+011
a_2	7.8064e+023	2.0969e+022
a_3	7.8381e+034	1.2433e+033
a_4	2.6182e+045	4.4514e+043
a_5	2.6260e+055	8.9478e+053
a_6	5.1395e+064	9.4860e+063
a_7		4.3141e+073
a_8		5.4619e+082

Trace label	Figure	Section	page
15	6.41	6.5.3	169
15	6.42	6.5.3	170
15	7.14	7.6	191
15kS/m model	7.23	7.7	200

	$S_{11} = S_{22}$	$S_{21} = S_{12}$
NP	6	8
b_o	-0.9031	4.0173e-009
b_1	-2.0619e+012	-1.2315e+003

	$S_{11} = S_{22}$	$S_{21} = S_{12}$
b_2	-6.6713e+023	3.4022e+014
b_3	-6.2922e+034	-5.9173e+025
b_4	-1.9598e+045	8.2766e+036
b_5	-1.8253e+055	-8.4142e+047
b_6	-3.3507e+064	6.2626e+058
b_7		-3.0106e+069
b_8		7.1846e+079
a_1	2.1305e+012	2.2017e+011
a_2	6.7866e+023	2.5601e+022
a_3	6.3545e+034	1.6494e+033
a_4	1.9707e+045	6.3231e+043
a_5	1.8302e+055	1.3671e+054
a_6	3.3531e+064	1.5471e+064
a_7		7.5348e+073
a_8		1.0162e+083

Trace label	Figure	Section	page
14	6.41	6.5.3	169
14	6.42	6.5.3	170
14	7.14	7.6	191

	$S_{11} = S_{22}$	$S_{21} = S_{12}$
NP	6	7
b_o	-0.8914	-1.4307e-008
b_1	-2.3993e+012	2.9827e+003
b_2	-8.9361e+023	-7.3837e+014
b_3	-9.6899e+034	9.4977e+025
b_4	-3.4909e+045	-1.0616e+037
b_5	-3.7941e+055	7.5843e+047
b_6	-8.1452e+064	-3.7053e+058
b_7		8.5648e+068
a_1	2.4881e+012	1.3372e+011
a_2	9.1075e+023	1.1499e+022
a_3	9.7966e+034	4.8131e+032
a_4	3.5125e+045	1.2091e+043
a_5	3.8055e+055	1.4599e+053
a_6	8.1518e+064	7.9257e+062
a_7		1.1242e+072

Trace label	Figure	Section	page
13	6.41	6.5.3	169
13	6.42	6.5.3	170
13	7.14	7.6	191

	$S_{11} = S_{22}$	$S_{21} = S_{12}$
NP	6	7
b_o	-0.8948	-1.8906e-008

b_1	-2.1105e+012	4.4942e+003
b_2	-7.0645e+023	-1.1183e+015
b_3	-6.9491e+034	1.5703e+026
b_4	-2.2878e+045	-1.8141e+037
b_5	-2.3007e+055	1.3918e+048
b_6	-4.7089e+064	-7.1367e+058
b_7		1.7631e+069
a_1	2.1872e+012	1.5829e+011
a_2	7.1983e+023	1.4515e+022
a_3	7.0249e+034	6.7699e+032
a_4	2.3019e+045	1.8170e+043
a_5	2.3077e+055	2.4064e+053
a_6	4.7128e+064	1.3939e+063
a_7		2.1551e+072

Trace label	Figure	Section	page
12	6.41	6.5.3	169
12	6.42	6.5.3	170
12	7.14	7.6	191

	$S_{11} = S_{22}$	$S_{21} = S_{12}$
NP	6	7
b_o	-0.8854	-2.4954e-008
b_1	-2.3070e+012	6.7699e+003
b_2	-8.4140e+023	-1.7200e+015
b_3	-9.0112e+034	2.6329e+026
b_4	-3.2400e+045	-3.1839e+037
b_5	-3.5739e+055	2.6266e+048
b_6	-8.0393e+064	-1.4282e+059
b_7		3.7849e+069
a_1	2.3983e+012	1.8638e+011
a_2	8.5872e+023	1.8538e+022
a_3	9.1181e+034	9.6136e+032
a_4	3.2618e+045	2.7928e+043
a_5	3.5857e+055	4.0566e+053
a_6	8.0466e+064	2.5363e+063
a_7		4.2768e+072

Trace label	Figure	Section	page
11	6.41	6.5.3	169
11	6.42	6.5.3	170
11	7.14	7.6	191

	$S_{11} = S_{22}$	$S_{21} = S_{12}$
NP	6	7
b_o	-0.8852	-3.2899e-008
b_1	-2.1371e+012	1.0210e+004

b_2	-7.3281e+023	-2.6910e+015
b_3	-7.4310e+034	4.4944e+026
b_4	-2.5505e+045	-5.7607e+037
b_5	-2.7260e+055	5.1297e+048
b_6	-6.1309e+064	-2.9876e+059
b_7		8.5440e+069
a_1	2.2227e+012	2.1885e+011
a_2	7.4812e+023	2.3964e+022
a_3	7.5209e+034	1.3841e+033
a_4	2.5681e+045	4.4014e+043
a_5	2.7353e+055	7.0357e+053
a_6	6.1369e+064	4.7966e+063
a_7		8.8565e+072

	$S_{11} = S_{22}$	$S_{21} = S_{12}$
NP	6	7
b_o	-0.8743	-4.3326e-008
b_1	-2.3271e+012	1.5444e+004
b_2	-8.6882e+023	-4.2928e+015
b_3	-9.5965e+034	7.8492e+026
b_4	-3.6030e+045	-1.0799e+038
b_5	-4.2371e+055	1.0447e+049
b_6	-1.0533e+065	-6.5873e+059
b_7		2.0496e+070
a_1	2.4292e+012	2.5692e+011
a_2	8.8870e+023	3.1393e+022
a_3	9.7238e+034	2.0295e+033
a_4	3.6304e+045	7.1413e+043
a_5	4.2532e+055	1.2642e+054
a_6	1.0545e+065	9.4926e+063
a_7		1.9321e+073

	$S_{11} = S_{22}$	$S_{21} = S_{12}$
NP	5	6
b_o	-0.8910	1.7516e-007
b_1	-1.5683e+012	-4.3762e+004

b_2	-3.7189e+023	1.0200e+016
b_3	-2.3227e+034	-1.3842e+027
b_4	-3.9484e+044	1.4099e+038
b_5	-1.2707e+054	-8.8094e+048
b_6		2.7522e+059
a_1	1.6266e+012	1.6418e+011
a_2	3.7875e+023	1.4090e+022
a_3	2.3454e+034	5.8038e+032
a_4	3.9665e+044	1.2067e+043
a_5	1.2722e+054	1.0171e+053
a_6		2.3403e+062

Trace label	Figure	Section	page
8	6.41	6.5.3	169
8	6.42	6.5.3	170
8	7.14	7.6	191

	$S_{11} = S_{22}$	$S_{21} = S_{12}$
NP	6	6
b_o	-0.8611	2.4340e-007
b_1	-2.2978e+012	-7.2488e+004
b_2	-8.7072e+023	1.7799e+016
b_3	-9.9279e+034	-2.7156e+027
b_4	-3.9427e+045	3.0028e+038
b_5	-5.0858e+055	-2.0846e+049
b_6	-1.4627e+065	7.1766e+059
a_1	2.4114e+012	2.0289e+011
a_2	8.9333e+023	1.9709e+022
a_3	1.0079e+035	9.3742e+032
a_4	3.9775e+045	2.1933e+043
a_5	5.1088e+055	2.1022e+053
a_6	1.4646e+065	5.4180e+062

Trace label	Figure	Section	page
7	6.41	6.5.3	169
7	6.42	6.5.3	170
7	7.14	7.6	191

	$S_{11} = S_{22}$	$S_{21} = S_{12}$
NP	5	6
b_o	-0.8747	3.3808e-007
b_1	-1.6218e+012	-1.2113e+005
b_2	-4.0564e+023	3.2255e+016
b_3	-2.7101e+034	-5.5799e+027
b_4	-5.0565e+044	6.8531e+038
b_5	-1.8696e+054	-5.3585e+049
b_6		2.0737e+060

a_1	1.6920e+012	2.5116e+011
a_2	4.1441e+023	2.8318e+022
a_3	2.7414e+034	1.5702e+033
a_4	5.0846e+044	4.2196e+043
a_5	1.8724e+054	4.6536e+053
a_6		1.3695e+063

	$S_{11} = S_{22}$	$S_{21} = S_{12}$
NP	5	6
b_o	-0.8628	4.6957e-007
b_1	-1.6750e+012	-2.0542e+005
b_2	-4.3920e+023	6.1281e+016
b_3	-3.1099e+034	-1.2217e+028
b_4	-6.2641e+044	1.7111e+039
b_5	-2.5730e+054	-1.5389e+050
b_6		6.8599e+060
a_1	1.7552e+012	3.1358e+011
a_2	4.4975e+023	4.2102e+022
a_3	3.1501e+034	2.7693e+033
a_4	6.3035e+044	8.7433e+043
a_5	2.5776e+054	1.1306e+054
a_6		3.8835e+063

	$S_{11} = S_{22}$	$S_{21} = S_{12}$
NP	4	5
b_o	-0.8781	-2.2578e-006
b_1	-1.0919e+012	7.3325e+005
b_2	-1.6860e+023	-1.7579e+017
b_3	-5.6954e+033	2.6052e+028
b_4	-3.3427e+043	-2.4849e+039
b_5		1.1516e+050
a_1	1.1365e+012	2.1599e+011
a_2	1.7177e+023	1.9964e+022
a_3	5.7432e+033	8.0931e+032
a_4	3.3499e+043	1.3053e+043
a_5		5.4325e+052

Trace label	Figure	Section	page
1D-DF CFC1	7.22	7.7	199
CFC1 Drude model	7.23	7.7	200

	$S_{11} = S_{22}$	$S_{21} = S_{12}$
NZ	2	4
b_o	-7.4551e+024	1.8571e+026
b_1	-8.8757e+034	1.2440e+037
b_2	-1.9872e+044	3.3477e+047
b_3		4.0998e+057
b_4		2.0088e+067
NP	4	6
a_1	4.0570e+012	6.3119e+013
a_2	7.5319e+024	6.8724e+028
a_3	8.9106e+034	7.6089e+040
a_4	1.9897e+044	1.5302e+051
a_5		9.3256e+060
a_6		1.6102e+070

Trace label	Figure	Section	page
1D-DF CFC2	7.22	7.7	199
CFC2 Drude model	7.23	7.7	200

	$S_{11} = S_{22}$	$S_{21} = S_{12}$
NZ	2	4
b_o	-1.0508e+025	4.4544e+026
b_1	-9.8201e+034	1.8841e+037
b_2	-1.5998e+044	4.4513e+047
b_3		4.7616e+057
b_4		2.4803e+067
NP	4	6
a_1	4.9342e+012	3.8324e+016
a_2	1.0584e+025	5.8228e+030
a_3	9.8470e+034	3.5339e+041
a_4	1.6012e+044	5.2388e+051
a_5		2.4205e+061
a_6		3.0397e+070